The Dissertation Committee for Kai Yang Certifies that this is the approved version of the following dissertation:

FFT and Multigrid Accelerated Integral Equation Solvers for Multi-Scale Electromagnetic Analysis in Complex Backgrounds

Committee:

Ali E. Yılmaz, Supervisor

Carlos Torres-Verdin

Hao Ling

Andrea Alu

Theodore Rappaport

FFT and Multigrid Accelerated Integral Equation Solvers for Multi-Scale Electromagnetic Analysis in Complex Backgrounds

by

Kai Yang, B.E.; M.E.

Dissertation

Presented to the Faculty of the Graduate School of

The University of Texas at Austin

in Partial Fulfillment

of the Requirements

for the Degree of

Doctor of Philosophy

The University of Texas at Austin

August 2014

Dedication

Dedicated to my family

Acknowledgements

I would like to express my deepest gratitude to my supervisor, Dr. Ali E. Yılmaz. His profound knowledge and enthusiasm in research have inspired my interests in Electromagnetics and enriched my vision in various areas. He provided invaluable guidance and steadfast encouragement throughout my graduate years.

I would also like to thank the members of my dissertation committee, Dr. Carlos Torres-Verdin, Dr. Hao Ling, Dr. Andrea Alu, and Dr. Theodore Rappaport for their time, excellent lectures, insightful comments and suggestions.

A special thanks to all of my colleagues in the Computational Electromagnetics Group at UT-Austin, especially Fangzhou (Max) Wei, Mingfeng Wu, Guneet Kaur, Vivek Subramanian, Jackson Massey, Chang Liu, and Tahir Malas for their support and friendship.

Finally, I would like to thank my fiancee Lei, my parents, and my brother for their encouragement, support and sacrifices.

FFT and Multigrid Accelerated Integral Equation Solvers for Multi-Scale Electromagnetic Analysis in Complex Backgrounds

Kai Yang, Ph.D.

The University of Texas at Austin, 2014

Supervisor: Ali E. Yılmaz

Novel integral-equation methods for efficiently solving electromagnetic problems that involve more than a single length scale of interest in complex backgrounds are presented. Such multi-scale electromagnetic problems arise because of the interplay of two distinct factors: the structure under study and the background medium. Both can contain material properties (wavelengths/skin depths) and geometrical features at different length scales, which gives rise to four types of multi-scale problems: (1) two-scale, (2) multi-scale structure, (3) multi-scale background, and (4) multi-scale-squared problems, where a single-scale structure resides in a different single-scale background, a multi-scale structure resides in a single-scale background, a single-scale structure resides in a multi-scale background, and a multi-scale structure resides in a multi-scale background, respectively. Electromagnetic problems can be further categorized in terms of the relative values of the length scales that characterize the structure and the background medium as (a) high-frequency, (b) low-frequency, and (c) mixed-frequency problems, where the wavelengths/skin depths in the background medium, the structure's geometrical features

or internal wavelengths/skin depths, and a combination of these three factors dictate the field variations on/in the structure, respectively.

This dissertation presents several problems arising from geophysical exploration and microwave chemistry that demonstrate the different types of multi-scale problems encountered in electromagnetic analysis and the computational challenges they pose. It also presents novel frequency-domain integral-equation methods for solving these multi-scale problems. These methods avoid meshing the background medium and finding fields in an extended computational domain outside the structure, thereby resolving important complications encountered in type 3 and 4 multi-scale problems that limit alternative methods. Nevertheless, they have been of limited practical use because of their high computational costs and because most of the existing 'fast integral-equation algorithms' are not applicable to complex Green function kernels. This dissertation introduces novel FFT, multigrid, and FFT-truncated multigrid algorithms that reduce the computational costs of frequency-domain integral-equation methods for complex backgrounds and enable the solution of unprecedented type 3 and 4 multi-scale problems. The proposed algorithms are formulated in detail, their computational costs are analyzed theoretically, and their features are demonstrated by solving benchmark and challenging multi-scale problems.

Table of Contents

List of Tables

List of Figures

Chapter I: Introduction

Efficient analysis of electromagnetic scattering, radiation, and propagation in complex backgrounds is important for many engineering applications. Consider three examples from geophysics, microwave engineering, and microwave chemistry: (i) To interpret marine controlled source electromagnetic measurements when exploring hydrocarbon reservoirs, the effects of oil/gas and various isotropic/uniaxial layered background media (sea, soil, rock, etc.) on extremely low-frequency electromagnetic waves must be evaluated [1],[2]. (ii) To design on-chip and on-package antennas, the electromagnetic interactions between integrated antennas, silicon substrate, interconnect layers, and other circuitry must be evaluated at GHz frequencies [3]. (iii) To predict the outcome of microwave-assisted chemistry experiments, the energy absorbed by various materials (solutions, thin films, containers, rotors, etc.) in a rectangular microwave reactor must be calculated [4]. As the complexity of such applications and the realism of their computer models continue to increase, conventional numerical algorithms and the simulators they drive become ineffective even though the raw computational power they can access continues to scale up. This is mainly a reflection of the "tyranny of scales" that plagues all fields of computational science and engineering [5]: Few conventional algorithms are efficient and robust enough for computations involving more than a single length scale of interest. As can be seen in the three examples above, multi-scale problems, where important field variations are observed in the domain of analysis at multiple time or length scales, are often encountered in electromagnetics. While multi-time-scale problems can often be avoided by time-harmonic/frequency-domain analysis, multi-length-scale problems remain a challenge and are the focus of this dissertation.

1.1 MULTI-LENGTH-SCALE PROBLEMS IN ELECTROMAGNETIC ANALYSIS

Multi-length-scale, henceforth referred to as multi-scale, electromagnetic problems arise because of two distinct reasons: (i) The structure under study can contain material properties (permittivity/conductivity/permeability)—equivalently, "internal" field wavelengths/skin depths—or geometrical features at different length scales, e.g., installed antennas (electrically small structures installed on electrically large platforms), electronic packaging (connecting small chips to large boards), biological systems (inhomogeneous tissues), and through-casing borehole resistivity measurements (large conductivity contrast) give rise to such structures. (ii) The background medium can consist of material properties—equivalently, "external" field wavelengths/skin depths— or geometrical features at multiple length scales; e.g., each layer of earth or a packaging substrate can be characterized by a different length scale. The interplay of these two factors can give rise to *Single-Scale Problems*, where a structure characterized by a single length scale (a single-scale structure) resides in a background characterized by a similar single length scale (a similar single-scale background), or four types of multi-scale problems: *Type 1 multi-scale problems (two-scale)*, where a single-scale structure resides in a different single-scale background; *type 2 multi-scale problems (multi-scale structure)*, where a multi-scale structure resides in a single-scale background; *type 3 multi-scale problems (multi-scale background)*, where a single-scale structure resides in a multi-scale background; and *type 4 multi-scale problems (multi-scale-squared)*, where a multi-scale structure resides in a multi-scale background. Note that only the first two types of multi-scale problems exist in single-scale backgrounds (e.g., free-space, homogeneous medium, or a rectangular cavity

filled with a homogeneous material), whereas all four types are encountered in multi-scale backgrounds (e.g., layered media).

Multi-scale electromagnetic problems can be further categorized based on the relative values of the length scales that characterize the structure and the background medium; specifically, by using the high-, low-, and mixed-frequency nomenclature. In the *high-frequency simulation regime*, the field variations on/in the structure are dictated by the wavelengths/skin depths in the background medium; typically, these lengths are much smaller than the geometrical features of the structure and comparable to the internal field wavelengths/skin depths (if the structure is penetrable). In the *low-frequency simulation regime*, the field variations on/in the structure are dictated by the geometrical features or internal wavelengths/skin depths (for penetrable structures); typically, these lengths are much smaller than the wavelengths/skin depths in the background medium. In the *mixed-frequency simulation regime*, the field variations on/in the structure are dictated by a combination of background and internal wavelengths/skin depths and geometrical features; typically, the characteristic lengths at different parts of the structure are dictated by different factors. In the high-frequency regime, generally type 1 and 3 multi-scale problems are solved because the structure does not constrain the field variation and associated discretization lengths. In the low-frequency regime, all four types of multi-scale problems are encountered; however, certain simplifications are available because all lengths are smaller than the background wavelengths/skin depths. The mixed-frequency regime necessarily gives rise to type 2 and 4 multi-scale problems; moreover, these are typically more challenging than those in the low-frequency regime because the lengths of interest are both sub- and multi-wavelength/skin depth. As a result, multi-scale electromagnetic

problems can be organized into eight categories as shown in Table 1.1. This dissertation proposes novel methods to address the challenges inherent in all eight categories of multi-scale electromagnetic analysis in complex backgrounds.

Table 1.1: Multi-scale problem categorization

Problem Type	Simulation Regime	Example	Explanation ($\lambda / \delta / h$ denotes the minimum wavelength/skin depth/layer thickness in the background medium, λ_0 is the wavelength in air)
Type 1 (Two-scale)	a. High Frequency	Scattering from a tank above ground at ~1 GHz [6].	Structure volume $\sim (10\lambda)^3$.
	b. Low Frequency	Coupling onto a partially shielded computer board at 150 MHz [7].	Structure volume $\sim 10^{-4}\lambda_0^3$.
Type 2 (Multi-scale structure)	b. Low Frequency	Scattering from a aircraft with a highly discretized fueling device at 1 MHz [8].	Structure volume $\sim (10^{-2}\lambda_0)^3$, feature around fuelling device $\sim 10^{-4}\lambda_0$.
	c. Mixed Frequency	Radiation from a monopole antenna on a high-fidelity ship model at 50 MHz [9].	Structure volume $\sim (10\lambda_0)^3$, features around antennas $\sim 10^{-2}\lambda_0$.
Type 3 (Multi-scale background)	a. High Frequency	Radiation from a microstrip patch array at 2.2 GHz [10].	Structure area $\sim (10\lambda_0)^2$, thickness of the substrate $\lambda_0 / h = 80$.
	b. Low Frequency	Scattering from a 0.1 km^3 petroleum reservoir 1 km under the sea at 1 Hz [2].	Structure volume $\sim (10^{-3}\lambda)^3$, wavelength/skin depth in soil: $\{\lambda_0 / \lambda, \lambda_0 / \delta\} = \{10^5, 10^6\}$.
Type 4 (Multi-scale squared)	b. Low Frequency	Scattering from a 45 km^3 salt dome and 2.5 km^3 petroleum reservoir under the sea at 1 mHz [11].	Structure volume $\sim (10^{-1}\lambda)^3$, thickness of the petroleum reservoir: $10^{-3}\lambda$, wavelength/skin depth in soil: $\{\lambda_0 / \lambda, \lambda_0 / \delta\} = \{10^6, 10^7\}$.
	c. Mixed Frequency	Scattering from a densely packed interconnect structure at 20 GHz [12].	Structure area $\sim (10\lambda_0)^2$, width of the strip $\sim 10^{-2}\lambda_0$, thickness of the substrate: $\lambda_0 / h = 60$.

1.2 INTEGRAL EQUATION METHODS

While a large variety of frequency- or time-domain, integral- or differential-equation based techniques can be used for electromagnetic analysis, frequency-domain surface and volume integral equation (SIE and VIE) solvers offer some of the most promising approaches for multi-scale problems, especially of types 3 and 4. This is because they only find unknown currents on/fields in the structure of interest (they never discretize the background medium), do not impose artificial/approximate mesh termination conditions (they analytically enforce the radiation condition), avoid multi-time-scale difficulties, and directly/exactly model dispersive material properties.

SIE solvers are especially useful at microwave frequencies, where most metals can be modeled as perfect electrically conducting (PEC) structures. The PEC approximation reduces computational costs significantly as integral equations can be formulated in terms of only the tangential electric current on PEC surfaces [13],[14]. When the PEC approximation is not valid, e.g., at lower frequencies or when there are dielectric materials, SIE solvers can still be used effectively for piecewise homogeneous structures by formulating integral equations in terms of tangential electric and magnetic fields on interface surfaces [15]-[18]. As the inhomogeneity of a given size structure increases, however, SIE solvers are no longer cost effective compared to VIE solvers (the area of the interface surfaces converges to the structure volume). Indeed, for continuously inhomogeneous structures, the spatial dimension of the problem can no longer be reduced by one [19] and integral equations must be formulated in terms of the electromagnetic fields inside penetrable volumes [20],[21]. SIE and VIE solvers use the well-known method-of-moments (MOM) procedure: The unknown surface currents on/volume fields

in the structure of interest are discretized by N sub-domain basis functions with unknown coefficients; to find these coefficients, the integral equations are weighted by N testing functions and converted into a linear system of equations. Although the MOM procedure is applicable to all length scales of interest in principle, it suffers from two limitations for multi-scale analysis: Low-frequency breakdown and high computational complexity.

On the one hand, the MOM basis/testing function choice depends on the frequency regime of the simulation: (i) In the high-frequency regime, divergence-conforming mixed-order functions such as the Rao-Wilton-Glisson (RWG) [22] and Schaubert-Wilton-Glisson (SWG) [23] functions can be used successfully. (ii) In the low-frequency regime, integral-equation kernels break down when RWG/SWG edge lengths are 10^{-5}-10^{-4} of the wavelength/skin depth in the background medium due to the imbalance between vector and scalar potential contributions and the limitations of finite precision arithmetic [24]. This is especially true for electric-field SIEs, for which loop-tree [25], loop-star [26], loop-charge [27], Calderon-preconditioning based Buffa-Christiansen [28],[29], hierarchical functions [8],[30],[31], and novel formulations based on the separation of current and charge unknown [32]-[34] have been proposed to combat the low-frequency breakdown; VIEs appear to be immune to it [35]. (iii) In the mixed-frequency regime, a seamless transition is required from RWG/SWG functions in some parts of the structure to those that avoid the low-frequency breakdown in other parts; various methods have been recently proposed to achieve this transition, e.g., [30],[31], and [36].

On the other hand, the classical MOM has high computational costs: It requires $O(N^2)$ operations/memory space to form/store a dense linear system of equations and $O(N^2)$ operations per iteration to solve this system using an iterative solver. Note that

even though the MOM complexity expressions are the same for structures residing in free space, layered-medium, and rectangular-cavity backgrounds, the matrix fill times are orders of magnitude higher for the latter two due to the cost of Sommerfeld integrals and slowly converging triple infinite series needed to evaluate the more complicated Green functions. The MOM computational costs can be reduced by using various classes of fast algorithms, e.g., fast multipole method [37], low-rank approximation [38], FFT [39],[40], and multigrid based algorithms [41]-[44]. For a large variety of single-scale structures residing in free space (type 1a and 1b multi-scale problems), these algorithms have been shown to reduce the MOM costs to $O(N)$ operations/memory space within logarithmic factors. In contrast, when the structures contain important features at multiple length scales or reside in layered-medium/rectangular-cavity backgrounds (type 2-4 multi-scale problems), the majority of fast algorithms break down/lose efficiency and must be modified [45]-[56] to reduce the MOM computational complexity.

1.3 ORGANIZATION OF THE DISSERTATION

Novel FFT- and multigrid-based algorithms are proposed in this dissertation to reduce the MOM computational complexity for multi-scale analysis in complex backgrounds, i.e., planar-layered medium and rectangular-cavity backgrounds. Note that, although it is an important and active area of inquiry, this dissertation is not focused on the low-frequency breakdown problem of SIEs. Instead, this problem is avoided by using SIE solvers only for PEC structures in the high-frequency regime (when edge lengths are $>10^{-3}$ of the relevant wavelength/skin depth) and VIE solvers otherwise; in other words, SIE formulations will be used only for type 1a and 3a multi-scale problems and VIE ones for

all types. The algorithms presented in this dissertation are expected to be applicable when alternative basis/testing functions are used to avoid low-frequency breakdown (as long as they are sub-domain functions).

The rest of the dissertation is organized as follows. Chapter II applies the adaptive integral method (AIM) for efficient analysis of scattering from arbitrarily meshed single-scale structures in homogeneous background (type 1a and 1b multi-scale problems). Chapter III extends the AIM scheme for fast analysis of electromagnetic scattering from single-scale structures in rectangular-cavity background (type 1a and 1b multi-scale problems). Chapter IV presents the multigrid method and combines it with the FFT-based methods to enable the fast simulation of multi-scale structures in homogeneous background (type 2a and 2b multi-scale problems). Chapter V extends the AIM for fast analysis of scattering from single-scale structures in a planar-layered medium background (type 3a and 3b multi-scale problems). Chapter VI shows the application of the developed methods to various problems in geophysics, microwave-assisted material synthesis, and microwave circuits. Chapter VII concludes this dissertation and discusses future research avenues.

Chapter II: Adaptive Integral Method for Homogeneous Background

This Chapter presents the adaptive integral method (AIM) for solving scattering from electrically large single-scale structures in homogeneous backgrounds (type 1a and 1b multi-scale problems). Section 2.1 describes the volume electric field integral equation for analyzing electromagnetic scattering from anisotropic volumes located in an unbounded homogeneous medium and its MOM solution. Section 2.2 details the AIM scheme and its computational complexity. The method is presented for the volume integral equation, but it is also applicable to surface integral equations as shown in Chapter V. The accuracy and efficiency of AIM for the volume electric field integral equation are verified numerically in Section 2.3.

2.1 VOLUME ELECTRIC FIELD INTEGRAL EQUATION AND MOM

Consider the scattering of a time-harmonic electric field $\mathbf{E}^{\text{inc}}$ from an arbitrarily shaped 3-D non-magnetic single-scale object embedded in an unbounded isotropic homogeneous background ($e^{j\omega t}$ time variation is assumed and suppressed in this dissertation). The object volume is denoted by V and the material properties in this anomalous volume are represented by the complex permittivity tensor $\tilde{\underline{\underline{\boldsymbol{\varepsilon}}}}_{\text{V}} = \underline{\underline{\boldsymbol{\varepsilon}}}_{\text{V}} + \underline{\underline{\boldsymbol{\sigma}}}_{\text{V}} / j\omega$, where $\underline{\underline{\boldsymbol{\varepsilon}}}_{\text{V}}$ denotes permittivity and $\underline{\underline{\boldsymbol{\sigma}}}_{\text{V}}$ is conductivity, i.e., the material is allowed to be anisotropic, lossy, and inhomogeneous. The complex permittivity and permeability of the homogeneous background are denoted as $\tilde{\varepsilon}_{\text{b}} = \varepsilon_{\text{b}} + \sigma_{\text{b}} / j\omega$ and μ_0 (Fig. 2.1(a)). The complex permittivity tensors are given as

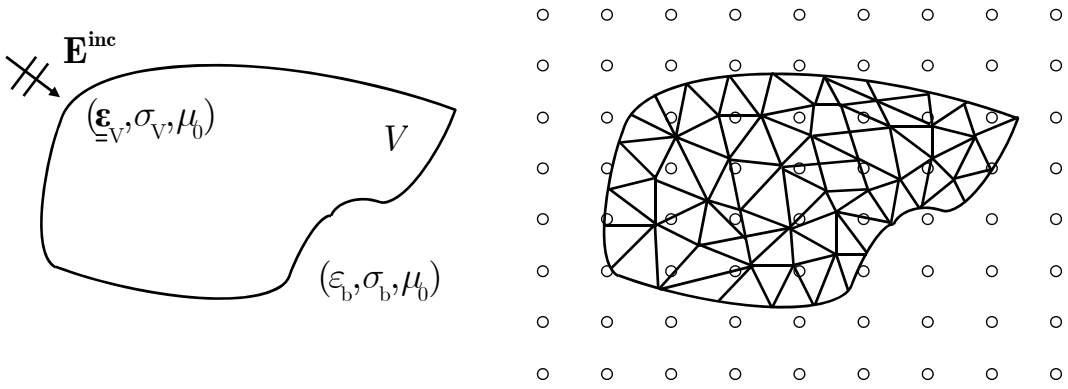

(a) (b)

Figure 2.1: (a) An aniosotropic 3-D dielectric object in a homogeneous medium. (b) The auxiliary AIM grid points and three of the basis functions defined on tetrahedral elements.

$$\tilde{\underline{\underline{\boldsymbol{\varepsilon}}}}_{\mathrm{V}}(\mathbf{r}) = \begin{bmatrix} \tilde{\varepsilon}_{\mathrm{V}}^{\mathrm{xx}}(\mathbf{r}) & \tilde{\varepsilon}_{\mathrm{V}}^{\mathrm{xy}}(\mathbf{r}) & \tilde{\varepsilon}_{\mathrm{V}}^{\mathrm{xz}}(\mathbf{r}) \\ \tilde{\varepsilon}_{\mathrm{V}}^{\mathrm{yx}}(\mathbf{r}) & \tilde{\varepsilon}_{\mathrm{V}}^{\mathrm{yy}}(\mathbf{r}) & \tilde{\varepsilon}_{\mathrm{V}}^{\mathrm{yz}}(\mathbf{r}) \\ \tilde{\varepsilon}_{\mathrm{V}}^{\mathrm{zx}}(\mathbf{r}) & \tilde{\varepsilon}_{\mathrm{V}}^{\mathrm{zy}}(\mathbf{r}) & \tilde{\varepsilon}_{\mathrm{V}}^{\mathrm{zz}}(\mathbf{r}) \end{bmatrix} \varepsilon_0 \tag{2.1.1}$$

To construct the volume electric-field integral equation (VEFIE), the total electric field in the anomalous volume is expressed in terms of the "conduction-current corrected electric flux density" [57] $\tilde{\mathbf{D}}$:

$$\tilde{\mathbf{D}}(\mathbf{r}) = \tilde{\underline{\underline{\boldsymbol{\varepsilon}}}}_{\mathrm{V}}(\mathbf{r}) \cdot [\mathbf{E}^{\mathrm{inc}}(\mathbf{r}) + \mathbf{E}^{\mathrm{sca}}(\mathbf{r})] \quad \text{for } \mathbf{r} \in V \tag{2.1.2}$$

Rearranging (2.1.2) and expressing the scattered field in mixed-potential form in terms of $\tilde{\mathbf{D}}$ yields the VEFIE:

$$\begin{aligned} \mathbf{E}^{\mathrm{inc}}(\mathbf{r}) = {} & \tilde{\underline{\underline{\boldsymbol{\varepsilon}}}}_{\mathrm{V}}^{-1}(\mathbf{r}) \cdot \tilde{\mathbf{D}}(\mathbf{r}) \\ & -\omega^2 \mu_0 \iiint_V g(\mathbf{r},\mathbf{r}')[\underline{\underline{\boldsymbol{\chi}}}(\mathbf{r}') \cdot \tilde{\mathbf{D}}(\mathbf{r}')]dv' \\ & -\frac{\nabla}{\tilde{\varepsilon}_{\mathrm{b}}} \iiint_V g(\mathbf{r},\mathbf{r}')\nabla' \cdot [\underline{\underline{\boldsymbol{\chi}}}(\mathbf{r}') \cdot \tilde{\mathbf{D}}(\mathbf{r}')]dv' \end{aligned} \tag{2.1.3}$$

where $\mathbf{r}'$ and $\mathbf{r}$ are the source and observer position vectors, $g(\mathbf{r},\mathbf{r}') = e^{-\gamma_b|\mathbf{r}-\mathbf{r}'|} / 4\pi\,|\,\mathbf{r}-\mathbf{r}'\,|$ is the homogeneous Green function, $\gamma_b = j\omega\sqrt{\mu_0\tilde{\varepsilon}_b}$ is the complex propagation constant in the background, and $\underline{\underline{\boldsymbol{\chi}}}$ denotes the generalized "contrast ratio" tensor [23]:

$$\underline{\underline{\boldsymbol{\chi}}}(\mathbf{r}) = \begin{bmatrix} \chi^{xx}(\mathbf{r}) & \chi^{xy}(\mathbf{r}) & \chi^{xz}(\mathbf{r}) \\ \chi^{yx}(\mathbf{r}) & \chi^{yy}(\mathbf{r}) & \chi^{yz}(\mathbf{r}) \\ \chi^{zx}(\mathbf{r}) & \chi^{zy}(\mathbf{r}) & \chi^{zz}(\mathbf{r}) \end{bmatrix} = \underline{\underline{\mathbf{I}}} - \tilde{\varepsilon}_b \underline{\underline{\mathbf{I}}} \cdot \underline{\underline{\tilde{\boldsymbol{\varepsilon}}}}_V^{-1}(\mathbf{r}) \tag{2.1.4}$$

where $\underline{\underline{\mathbf{I}}}$ is an identity tensor.

The VEFIE is converted to a system of linear equations using the standard MOM procedure: First, V is meshed with tetrahedral elements that have a total of N triangular faces; and $\tilde{\mathbf{D}}$ is expanded using N sub-domain basis functions $\mathbf{b}_1^V, \ldots, \mathbf{b}_N^V$

$$\tilde{\mathbf{D}}(\mathbf{r}) \cong \sum_{n=1}^{N} \mathbf{I}[n]\mathbf{b}_n^V(\mathbf{r}) \tag{2.1.5}$$

Here, $\mathbf{I}$ is the vector of unknown coefficients and the basis functions are chosen to be SWG functions [23], which are of three types: Each SWG function $\mathbf{b}_n^V$ is associated with the n^{th} triangular face and is non-zero over either (i) one tetrahedron facing the boundary of V, or (ii) two tetrahedra with different contrast ratios, or (iii) two tetrahedra with the same contrast ratio. The (piecewise constant) permittivity and contrast ratio tensor throughout the support of $\mathbf{b}_n^V$ is denoted as $\underline{\underline{\tilde{\boldsymbol{\varepsilon}}}}_{V,n}$ and $\underline{\underline{\boldsymbol{\chi}}}_n$, respectively. When (2.1.5) is substituted in (2.1.3), the divergence operation in the last term must be evaluated carefully because the contrast ratio is a tensor. Using dyadic notation, the result is expressed as

$$\nabla' \cdot [\underline{\underline{\boldsymbol{\chi}}}_n \cdot \mathbf{b}_n^V] = \frac{\chi_n^{xx} + \chi_n^{yy} + \chi_n^{zz}}{3} \nabla' \cdot \mathbf{b}_n^V + [\nabla' \cdot \underline{\underline{\boldsymbol{\chi}}}_n] \cdot \mathbf{b}_n^V \tag{2.1.6}$$

where the first term represents a piecewise-constant volume charge density and the second term denotes a surface charge density at the triangular faces caused by the discontinuity of $\underline{\underline{\chi}}_n$. Because $\nabla' \cdot \underline{\underline{\chi}}_n$ is a vector that can point in arbitrary directions, surface charges can exist on *all faces* in the support of $\mathbf{b}_n^{\mathrm{V}}$ for all three types of SWG functions. In contrast, surface charges exist only on one face in the isotropic case. Next, (2.1.3) is tested by the symmetric testing scheme [58] to decrease the AIM anter/interpolation costs, i.e., $\mathbf{t}_m^{\mathrm{V}} = \underline{\underline{\chi}}_m \cdot \mathbf{b}_m^{\mathrm{V}}$ for $m = 1,\ldots,N$. This MOM procedure yields the matrix equation

$$(\mathbf{Z} + \mathbf{D})\mathbf{I} = \mathbf{V}^{\mathrm{inc}} \tag{2.1.7}$$

The entries of the $N \times N$ impedance matrix $\mathbf{Z}$, the Gram matrix $\mathbf{D}$, and the tested incident field vector $\mathbf{V}^{\mathrm{inc}}$ are given as

$$\begin{aligned}
\mathbf{Z}[m,n] &= -\omega^2\mu_0 \iiint_V \mathbf{t}_m^{\mathrm{V}} \cdot \iiint_V g(\underline{\underline{\chi}}_n \cdot \mathbf{b}_n^{\mathrm{V}}) dv' dv \\
&\quad + \iiint_V [\nabla \cdot \mathbf{t}_m^{\mathrm{V}}] \iiint_V g \nabla' \cdot (\underline{\underline{\chi}}_n \cdot \mathbf{b}_n^{\mathrm{V}}) dv' dv \,/\, \tilde{\varepsilon}_{\mathrm{b}} \\
&\quad - \iint_{S_m} \mathbf{t}_m^{\mathrm{V}} \cdot \hat{\mathbf{n}}_m \iiint_V g \nabla' \cdot (\underline{\underline{\chi}}_n \cdot \mathbf{b}_n^{\mathrm{V}}) dv' ds \,/\, \tilde{\varepsilon}_{\mathrm{b}} \\
\mathbf{D}[m,n] &= \iiint_V \mathbf{t}_m^{\mathrm{V}} \cdot [\underline{\underline{\varepsilon}}_{\mathrm{V},n}^{-1} \cdot \mathbf{b}_n^{\mathrm{V}}] dv \\
\mathbf{V}^{\mathrm{inc}}[m] &= \iiint_V \mathbf{t}_m^{\mathrm{V}} \cdot \mathbf{E}^{\mathrm{inc}} dv
\end{aligned} \tag{2.1.8}$$

for $1 \le m,n \le N$. The calculation of the impedance matrix (matrix fill time), the memory required for storing it (memory cost), and the solution of (2.1.7) (matrix solve time) are the main computational costs of the above MOM procedure. The matrix fill time and memory cost scale as $O(N^2)$ and the matrix solve time scales as $O(N^{\mathrm{it}}N^2)$ if an iterative solver that converges in N^{it} iterations is used. The computational costs of MOM

can be reduced by exploiting the convolution form of homogeneous Green functions as detailed next for AIM.

2.2 AIM

The proposed AIM scheme is formulated by enclosing V with an auxiliary 3-D regular grid with $N^{\mathrm{3D}} = N^{\mathrm{3D,x}} N^{\mathrm{3D,y}} N^{\mathrm{3D,z}}$ nodes, where $N^{\mathrm{3D},\{\mathrm{x,y,z}\}}$ denote the number of points in the three Cartesian directions (Fig. 2.1(b)). The MOM matrix is then approximated as $\mathbf{Z} \approx \mathbf{Z}^{\mathrm{corr}} + \mathbf{Z}^{\mathrm{FFT}}$, where $\mathbf{Z}^{\mathrm{corr}}$ is a "pre-corrected" matrix [40] and $\mathbf{Z}^{\mathrm{FFT}}$ is given as

$$\mathbf{Z}^{\mathrm{FFT}} = -\omega^2 \mu_0 \begin{bmatrix} \boldsymbol{\Lambda}^{\mathrm{x,V}} \\ \boldsymbol{\Lambda}^{\mathrm{y,V}} \\ \boldsymbol{\Lambda}^{\mathrm{z,V}} \end{bmatrix}^{\dagger} \begin{bmatrix} \mathbf{G} & \mathbf{0} & \mathbf{0} \\ \mathbf{0} & \mathbf{G} & \mathbf{0} \\ \mathbf{0} & \mathbf{0} & \mathbf{G} \end{bmatrix} \begin{bmatrix} \boldsymbol{\Lambda}^{\mathrm{x,V}} \\ \boldsymbol{\Lambda}^{\mathrm{y,V}} \\ \boldsymbol{\Lambda}^{\mathrm{z,V}} \end{bmatrix} + \frac{\boldsymbol{\Lambda}^{\nabla,\mathrm{V}\dagger} \mathbf{G} \boldsymbol{\Lambda}^{\nabla,\mathrm{V}}}{\tilde{\varepsilon}_{\mathrm{b}}} \tag{2.2.1}$$

Here, the matrices $\boldsymbol{\Lambda}^{\{\mathrm{x,y,z},\nabla\},\mathrm{V}}$ represent anterpolation [41] from the primary mesh to the auxiliary grid. The anterpolation coefficients are also found by matching the multipole moments of M_n^{V} points on the auxiliary grid to those of the functions, $\hat{\mathbf{x}} \cdot (\underline{\underline{\boldsymbol{\chi}}}_n \cdot \mathbf{b}_n^{\mathrm{V}})$, $\hat{\mathbf{y}} \cdot (\underline{\underline{\boldsymbol{\chi}}}_n \cdot \mathbf{b}_n^{\mathrm{V}})$, $\hat{\mathbf{z}} \cdot (\underline{\underline{\boldsymbol{\chi}}}_n \cdot \mathbf{b}_n^{\mathrm{V}})$, and $\nabla \cdot (\underline{\underline{\boldsymbol{\chi}}}_n \cdot \mathbf{b}_n^{\mathrm{V}})$ and stored in $\boldsymbol{\Lambda}^{\{\mathrm{x,y,z},\nabla\},\mathrm{V}}$, respectively. These are $N^{\mathrm{3D}} \times N$ sparse *complex* matrices. The transpose matrices $\boldsymbol{\Lambda}^{\{\mathrm{x,y,z},\nabla\},\mathrm{V}\dagger}$ represent interpolation from the auxiliary grid to the primary mesh. The matrix $\mathbf{G}$ represents propagation from sources to observers on the auxiliary grid; it is a dense $N^{\mathrm{3D}} \times N^{\mathrm{3D}}$ 3-level block-Toeplitz matrix whose entries are

$$\mathbf{G}[u, v] = g(\mathbf{r}_u, \mathbf{r}_v) \tag{2.2.2}$$

for nodes $u \neq v$ on the auxiliary grid; $\mathbf{G}[u, u]$ is set to 0 since it is singular when $\mathbf{r}_u = \mathbf{r}_v$.

The pre-corrected matrix $\mathbf{Z}^{\text{corr}}$ ensures the accuracy of the proposed method by using the original impedance matrix entries to replace the most inaccurate entries in the approximation. Let N^{corr} denotes the number of non-zero entries in $\mathbf{Z}^{\text{corr}}$. The value of N^{corr} depends on the size of the correction region, which is controlled by the integer γ and the minimum "grid distance" [39] between the functions $\mathbf{t}_m^{\text{V}}$ and $\mathbf{f}_n^{\text{V}}$ defined as

$$\text{dist}^{\text{VV}'}[m,n] = \min_{u\in M_m, v\in M_n} \max\left(\left\lfloor\frac{\hat{\mathbf{x}}\cdot\mathbf{R}(\mathbf{r}_u,\mathbf{r}_v)}{\Delta_{\text{x}}}\right\rfloor, \left\lfloor\frac{\hat{\mathbf{y}}\cdot\mathbf{R}(\mathbf{r}_u,\mathbf{r}_v)}{\Delta_{\text{y}}}\right\rfloor, \left\lfloor\frac{\hat{\mathbf{z}}\cdot\mathbf{R}(\mathbf{r}_u,\mathbf{r}_v)}{\Delta_{\text{z}}}\right\rfloor\right) \tag{2.2.3}$$

where $\Delta_{\text{x,y,z}}$ denote the auxiliary grid spacing in the three Cartesian directions, $\lfloor\cdot\rfloor$ denotes the greatest integer less than or equal to its argument, and $\mathbf{R}$ is the vector pointing to $\mathbf{r}_u$ from $\mathbf{r}_v$. The entries of the pre-corrected matrix, which is a sparse $N\times N$ matrix, are

$$\mathbf{Z}^{\text{corr}}[m,n] = \begin{cases} \mathbf{Z}[m,n] - \mathbf{Z}^{\text{FFT}}[m,n], & \text{if } \text{dist}^{\text{VV}'}[m,n] < \gamma \\ 0, & \text{else} \end{cases} \tag{2.2.4}$$

for $1 \le m,n \le N$. $\text{dist}^{\text{VV}'}[m,n] < \gamma$ also indicates that two SWG functions $\mathbf{t}_m^{\text{V}}$ and $\mathbf{b}_n^{\text{V}}$ are considered to be near each other. $N^{\text{corr}} \sim N$ for single-scale structures [39],[48],[59] in type 1a and 1b multi-scale problems.

Because the propagation matrix in (2.2.1) has a 3-level block-Toeplitz structure, it can be efficiently multiplied with vectors using 3-D FFTs [52],[53],[59]-[62]. For example, consider the calculation of $\mathbf{G}\boldsymbol{\Lambda}^{\text{x,V}}\mathbf{I}$: first, a 3-D array of size $(2N^{\text{3D,x}}-1)\times(2N^{\text{3D,y}}-1)\times(2N^{\text{3D,z}}-1) \sim 8N^{\text{3D}}$ is constructed by re-organizing and zero-padding the $\boldsymbol{\Lambda}^{\text{x,V}}\mathbf{I}$ vector; the 3-D FFT of this array is computed; and the result is stored in ${}^{\text{FFT}}\mathbf{I}^{\text{x}}$. Second, ${}^{\text{FFT}}\mathbf{I}^{\text{x}}$ is multiplied element-by-element with ${}^{\text{FFT}}\mathbf{G}$, which is the 3-D FFT of an identical-sized array constructed from the unique entries of $\mathbf{G}$. Third,

the inverse 3-D FFT of the array resulting from this multiplication is found; and last, N^{3D} entries are extracted and re-organized to yield the desired vector $\mathbf{G}\mathbf{\Lambda}^{x,V}\mathbf{I}$. At each iteration, 4 FFTs (for the different current components), 4 element-by-element multiplications, and 4 inverse FFTs must be computed. These operations can be executed one current/field component at a time; thus, only 2 arrays of size $\sim 8N^{3D}$ are needed (one for the pre-computed FFT for $\mathbf{G}$ and one for ${}^{FFT}\mathbf{I}^{\{x,y,z,\nabla\},V}$ or the result of the element-by-element multiplication).

The above AIM algorithm requires $O(N + N^{3D})$ operations and bytes to compute and store the unique entries of anter/interpolation matrices, the pre-corrected matrix, and the propagation matrices; it also requires $O(N + N^{3D} \log N^{3D})$ operations to multiply them at each iteration.

2.3 NUMERICAL RESULTS

In this section, the accuracy and efficiency of the AIM is demonstrated. First, the computational complexity of AIM is validated by analyzing the power absorbed by a steak model in free space. Then, the AIM scheme is validated by modeling resistivity measurements in a deviated borehole and comparing results to the MOM solution and an independent reference [63]. In all the simulations in this dissertation, a diagonal preconditioner is used and the iterative solver is terminated when the relative residual error is less than 10^{-4}. Unless specified, third-order moment matching $(M_n^V = 4 \times 4 \times 4)$ is used for all basis and $\gamma = 2$. All the results in this section are obtained on the cluster using an MPI-based parallel implementation of the method [64],[65]. The observed timing and memory requirements of the implementation are 'serialized,' i.e., the parallelization effects

are minimized by using the minimum number of processes dictated by memory requirements and by reporting only the total computation times (number of processes times the wall-clock time) and total memory requirements [18].

2.3.1 Computational Complexity

The computational complexity of the AIM scheme is verified by analyzing scattering from a homogeneous steak model of size $0.1 \times 0.1 \times 0.01 \text{ m}^3$ with properties of muscle $(\varepsilon_{\text{V}} = 52.729\varepsilon_0, \sigma_{\text{V}} = 1.7388 \text{ S/m})$ [66],[67] in free space. Increasingly larger simulations are performed at 2.45 GHz by repeatedly doubling the volume mesh density: the average tetrahedron edge length is varied approximately from $\delta_{\text{V}} / 1.7$ to $\delta_{\text{V}} / 14.7$, where δ_{V} is the skin depth in the steak model. This procedure is similar to the one in [64],[65] except the sphere is replaced by a parallelepiped. The steak model is centered at $(0.225 \text{ m}, 0.21 \text{ m}, 0.175 \text{ m})$ and is excited by an impressed unit electric Hertzian dipole that is located at $(0.1 \text{ m}, 0.21 \text{ m}, 0.175 \text{ m})$ and points in the $(\hat{\mathbf{x}} + \hat{\mathbf{y}} + \hat{\mathbf{z}}) / \sqrt{3}$ direction. The accuracy of the simulations are quantified by computing the time-average absorbed power density and finding the L1 relative error norm [68]

$$err_{\text{L1}}^{P} = \frac{\iiint_V 0.5\sigma_{\text{V}} \mid \mathbf{E}(\mathbf{r}) \cdot \mathbf{E}^{*}(\mathbf{r}) - \mathbf{E}^{\text{ref}}(\mathbf{r}) \cdot \mathbf{E}^{\text{ref}*}(\mathbf{r}) \mid dv}{\iiint_V 0.5\sigma_{\text{V}} \mathbf{E}^{\text{ref}}(\mathbf{r}) \cdot \mathbf{E}^{\text{ref}*}(\mathbf{r}) dv} \tag{2.3.1}$$

The MOM solution of the same problem is used as reference when feasible; otherwise, a more accurate AIM solution is used (fifth order moments are matched and $\gamma = 3$). The AIM parameters are chosen to minimize the computational costs subject to the constraint that $err_{\text{L1}}^{P} > 1\%$; these parameters are detailed in Table 2.1. The total time-average power

absorbed by the steak model—the denominator in (2.3.1)—that is calculated using the finest mesh are about 8.3×10^2 W in the free space.

The observed computational costs of AIM simulations are shown in Figs. 2.2(a)-(c). The curves that are fitted to the observed data in Fig. 2.2 are in line with the complexity expressions in Section 2.2, where the matrix fill time, memory cost, and matrix solve time per iteration of the AIM scale as $O(N)$, $O(N)$, and $O(N \log N)$ for single-scale 3-D dielectric structures ($N^{3D} \sim N$), respectively. AIM outperforms MOM in all the performance metrics for N greater than ~3500. The number of iterations N^{it} varied from 241 to 439.

Table 2.1: Parameters for analyzing scattering from a steak model in free space

Average edge length	N	N^{3D}	Reference	err_{L1}^{P} (%)
$\delta_V / 1.7$	1168	$30 \times 30 \times 7$	MOM/AIM	0.15/0.15
$\delta_V / 3.7$	10 048	$54 \times 54 \times 9$	MOM/AIM	0.35/0.35
$\delta_V / 7.3$	77 002	$105 \times 105 \times 14$	MOM/AIM	0.57/0.57
$\delta_V / 14.7$	585 236	$224 \times 224 \times 25$	AIM	0.32

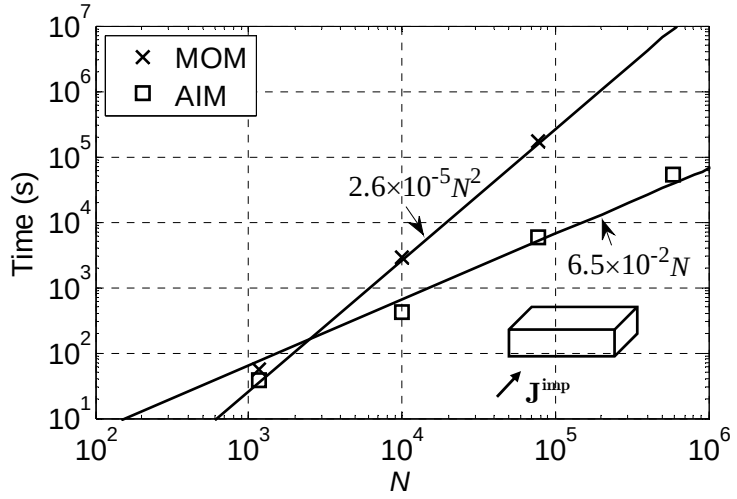

(a)

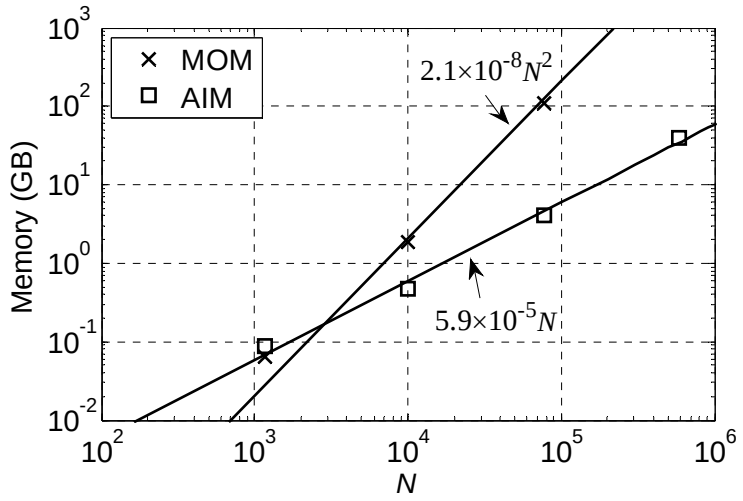

(b)

Figure 2.2: AIM for a steak model in free space as the mesh density of the steak is increased. (a) Matrix fill time. (b) Memory requirement. (c) Average solution time per iteration.

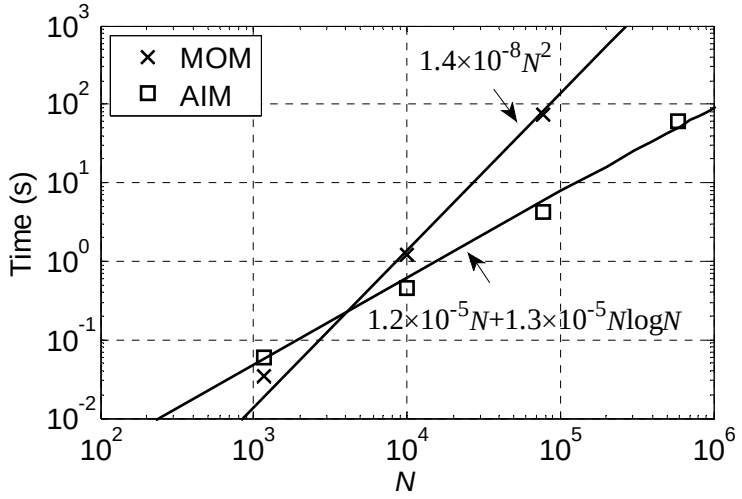

(c)

Figure 2.2: Continued.

2.3.2 Borehole Resistivity Measurements

Here, all permittivity values are set to the free-space permittivity ε_0, and the AIM grid spacing is given below.

The borehole is modeled as a 45° tilted circular cylinder of $2\ \mathrm{m}$ length and $0.01\pi\ \mathrm{m}^2$ cross-sectional area. The formation conductivity is set to $\sigma_\mathrm{b} = 0.01\ \mathrm{S/m}$ and two values of borehole conductivity are considered: $\sigma_\mathrm{v} = 0.1\ \mathrm{S/m}$ (case b1) and $\sigma_\mathrm{v} = 1.25\ \mathrm{S/m}$ (case b2). The transmitter is modeled as a 10 kHz unit magnetic Hertzian dipole oriented along the axis and located 0.3 m away from the end. The receiver is modeled as a small circular loop on the cylinder whose center is $5\ \mathrm{cm} \le d \le 1.4\ \mathrm{m}$ away from the transmitter.

The voltage detected with this measurement away from the one detected in free space is $\Delta U = -j\omega\mu_0 \hat{\mathbf{d}} \cdot [\mathbf{H}(\mathbf{r}_{\mathrm{RX}}) - \mathbf{H}^{\mathrm{fs}}(\mathbf{r}_{\mathrm{RX}})] \times 0.01\pi$ [63], where $\hat{\mathbf{d}}$ is the unit vector along the cylinder axis, $\mathbf{H} = \mathbf{H}^{\mathrm{inc}} + \mathbf{H}^{\mathrm{sca}}$ is the total magnetic field, $\mathbf{r}_{\mathrm{RX}}$ denotes the center of the receiver loop, $\hat{\mathbf{d}} \cdot \mathbf{H}^{\mathrm{fs}} = (1 + d\gamma_0) d^{-d\gamma_0} / (2\pi j\omega\mu_0 d^3)$, and γ_0 is the propagation constant in free space.

To solve the VEFIE, the borehole volume is discretized using tetrahedra with approximately 3.96 cm average edge length and the auxiliary grid spacing is approximately 3 cm in all three Cartesian directions in both cases (b1) and (b2). The length and radius of borehole are much smaller compare to the skin depth δ_{b} in the background medium (about $\delta_{\mathrm{b}} / 25$ and $\delta_{\mathrm{b}} / 500$). Therefore, this example is a type 1b multi-scale problem. The {average edge length, grid spacing} are approximately $\{\delta_{\min} / 402, \delta_{\min} / 531\}$ for case (b1) and $\{\delta_{\min} / 114, \delta_{\min} / 150\}$ for case (b2), where $\delta_{\min}$ is the minimum skin depth in the anomalous volume and the background medium; hence, $N = 20\ 729$ and $N^{3\mathrm{D}} = 72 \times 12 \times 12$. These unusually small mesh lengths are caused by the small cross-section of the borehole geometry.

Normalized voltages calculated with AIM are compared to MOM results, and those calculated and in [63] in Fig. 2.3. Good agreement is observed in both case (b1) and (b2), validating the method. For MOM, both cases required approximately 2.9×10^4 seconds for filling the matrices, 8.0 GB memory, and 4.7 seconds per iteration. For AIM, both cases required approximately 8.9×10^3 seconds for filling the matrices, 1.6 GB memory, and 1 second per iteration as the same mesh using AIM parameters. The iterative

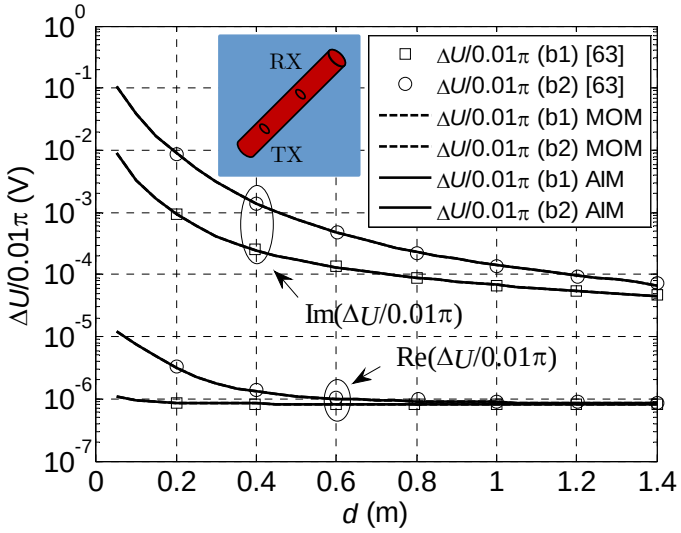

Figure 2.3: Normalized voltage detected relative to that detected in free space. The receiver is moved to different distances *d* from the transmitter.

solver converged in $N^{\text{it}} = 42$ iterations in case (b1) and $N^{\text{it}} = 18$ iterations in case (b2) for both AIM and MOM.

2.4 SUMMARY

This Chapter presented the AIM; the scheme was shown to be effective for solving scattering from large single-scale structures in a homogeneous background both in the high- and low-frequency regime of analysis (type 1a and 1b multi-scale problems). Numerical results validated the computational complexity of the method and demonstrated remarkable speedup and memory reduction compared to the MOM solution.

Chapter III: Adaptive Integral Method for Rectangular Cavities

Rectangular cavities are widely employed in microwave power and electromagnetic compatibility/interference applications. These applications require the analysis of scattering and radiation from arbitrarily shaped 3-D structures composed of perfect electrically conducting (PEC) surfaces and penetrable volumes located in such cavities. These problems are also categorized as type 1 multiscale problems; nonetheless, the more complex background medium (the rectangular cavity) necessitates modifications to algorithms that are efficient for type 1 multiscale problems when the background is a homogeneous medium. This Chapter extends the AIM presented in Chapter II for rectangular cavities. Section 3.1 describes the surface-volume electric field integral equation for analyzing electromagnetic scattering from structures located in a rectangular-cavity background. Section 3.2 details the corresponding rectangular-cavity Green functions. Sections 3.3-3.5 detail its MOM solution, the AIM extension and its computational complexity. The accuracy and efficiency of the extended AIM are verified by the numerical results in Section 3.6.

3.1 Surface-Volume Electric Field Integral Equation

Consider the scattering of a time-harmonic incident electric field $\mathbf{E}^{\text{inc}}$ by an arbitrarily shaped 3-D structure in a rectangular cavity of size $d_{\text{x}} \times d_{\text{y}} \times d_{\text{z}}$ (Fig. 3.1(a)). The structure is assumed to be composed of a perfect electrically conducting (PEC) surface S and a non-magnetic volume V with permittivity ε_{V} and conductivity σ_{V}. The cavity is assumed to reside in the first octant, have a corner at the origin, have PEC walls, and be filled by an equivalent homogeneous non-magnetic material with permeability

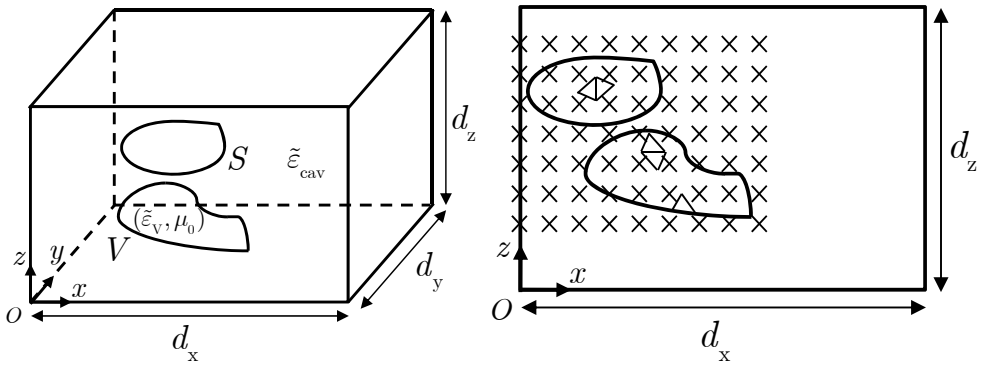

(a) (b)

Figure 3.1: Scattering from an arbitrarily shaped 3-D structure in a rectangular cavity. (a) Geometry. (b) Side view showing the auxiliary grid points and some triangular surface and tetrahedral volume elements.

μ_0, permittivity ε_{cav}, and conductivity σ_{cav}; this background material can be used to generalize the model, e.g., to approximate losses on finite conductivity walls or leakage from apertures [69]. The scattered field is expressed in mixed potential form as

$$\begin{aligned}
\mathbf{E}^{sca}(\mathbf{r}) &= \sum_{v' \in \{S,V\}} -j\omega \mathbf{A}^{v'}(\mathbf{r}) - \nabla \phi^{v'}(\mathbf{r}) \\
\mathbf{A}^{v'}(\mathbf{r}) &= \mu_0 \int \underline{\underline{\mathbf{g}}}_{cav}(\mathbf{r}, \mathbf{r}') \cdot \mathbf{J}^{v'}(\mathbf{r}') dr' \\
\phi^{v'}(\mathbf{r}) &= -\frac{1}{j\omega \tilde{\varepsilon}_{cav}} \int g^{\phi}_{cav}(\mathbf{r}, \mathbf{r}') \nabla' \cdot \mathbf{J}^{v'}(\mathbf{r}') dr'
\end{aligned} \tag{3.1.1}$$

where $\{\mathbf{r}, \mathbf{r}'\}$ denotes the {observer, source} position, $\{\underline{\underline{\mathbf{g}}}_{cav} = \hat{\mathbf{x}}\hat{\mathbf{x}} g^{xx}_{cav} + \hat{\mathbf{y}}\hat{\mathbf{y}} g^{yy}_{cav} + \hat{\mathbf{z}}\hat{\mathbf{z}} g^{zz}_{cav}, g^{\phi}\}$ denotes the {tensor, scalar} rectangular-cavity Green function, $\{\mathbf{J}^S, \mathbf{J}^V\}$ denotes the induced {surface, volume} current density, and $\{\mathbf{A}^{v'}, \phi^{v'}\}$ denotes the contribution of $\mathbf{J}^{v'}$ to the {magnetic vector, electric scalar} potential. The integrals in (3.1.1) and throughout this Chapter represent either surface or volume integration

depending on whether the source is a surface or a volume current density. The surface-volume electric-field integral equation (SV-EFIE) is formulated by enforcing the tangential boundary condition on S and relating the total electric field to the volume current density in V as

$$\begin{cases} \hat{\mathbf{n}}(\mathbf{r}) \times \hat{\mathbf{n}}(\mathbf{r}) \times [\mathbf{E}^{\text{inc}}(\mathbf{r}) + \mathbf{E}^{\text{sca}}(\mathbf{r})] = 0 & \text{for } \mathbf{r} \in S \\ j\omega(\tilde{\varepsilon}_{\text{V}} - \tilde{\varepsilon}_{\text{cav}})\left[\mathbf{E}^{\text{inc}}(\mathbf{r}) + \mathbf{E}^{\text{sca}}(\mathbf{r})\right] = \mathbf{J}^{\text{V}}(\mathbf{r}) & \text{for } \mathbf{r} \in V \end{cases} \tag{3.1.2}$$

where $\hat{\mathbf{n}}$ is the unit vector normal to the PEC surface, $\tilde{\varepsilon}_{\text{V}} = \varepsilon_{\text{V}} + \sigma_{\text{V}} / j\omega$, and $\tilde{\varepsilon}_{\text{cav}} = \varepsilon_{\text{cav}} + \sigma_{\text{cav}} / j\omega$.

3.2 RECTANGULAR-CAVITY GREEN FUNCTIONS

By applying the method of images, each of the four scalar rectangular-cavity Green functions $g_{\text{cav}}^{\text{xx,yy,zz,}\phi}$ can be expressed as a triple infinite series of homogeneous (free space) Green functions; each term in these series represent the interaction between the observer and either the source or one of the images of the source. To enable the FFT operations described in Section 3.4, each of these series is organized into eight sub-series of homogeneous Green functions as [70]

$$g_{\text{cav}}^{\{\text{xx,yy,zz,}\phi\}}(\mathbf{r}, \mathbf{r}') = \sum_{i_{\text{x}} \in \{\text{T,H}\}} \sum_{i_{\text{y}} \in \{\text{T,H}\}} \sum_{i_{\text{z}} \in \{\text{T,H}\}} B_{i_{\text{x}} i_{\text{y}} i_{\text{z}}}^{\{\text{x,y,z,}\phi\}} g_{i_{\text{x}} i_{\text{y}} i_{\text{z}}}(\mathbf{r}, \mathbf{r}') \tag{3.2.1}$$

Here, the coefficients $B_{i_{\text{x}} i_{\text{y}} i_{\text{z}}}^{\{\text{x,y,z,}\phi\}}$ are either 1 or -1. The signs follow from image theory and ensure that zero electric fields are produced tangential to the cavity walls; they are given as

$$B_{i_{\text{x}} i_{\text{y}} i_{\text{z}}}^{\{\text{x,y,z,}\phi\}} = -1^{\{2q_{i_{\text{x}}} + q_{i_{\text{y}}} + q_{i_{\text{z}}}, q_{i_{\text{x}}} + 2q_{i_{\text{y}}} + q_{i_{\text{z}}}, q_{i_{\text{x}}} + q_{i_{\text{y}}} + 2q_{i_{\text{z}}}, q_{i_{\text{x}}} + q_{i_{\text{y}}} + q_{i_{\text{z}}}\}} \tag{3.2.2}$$

where the constants $q_{\mathrm{T}} = 0$ and $q_{\mathrm{H}} = 0$. In (3.2.1), the functions $g_{i_{\mathrm{x}} i_{\mathrm{y}} i_{\mathrm{z}}}$ depend on either $x - x'$ or $x + x'$, either $y - y'$ or $y + y'$, and either $z - z'$ or $z + z'$. These dependences are indicated by using the subscript T or H: Throughout this Chapter and the dissertation, the first, second, and third subscript T (H) used with a function/matrix indicates that the function/matrix is in convolution/Toeplitz (correlation/Hankel) form in the x, y, and z direction, respectively. For example, $g_{\mathrm{THT}}(\mathbf{r}, \mathbf{r}') = g_{\mathrm{THT}}(x - x', y + y', z - z')$ is in convolution, correlation, and convolution form in the x, y, and z direction, respectively.

Each of the eight sub-series in (3.2.1), denoted by $g_{i_{\mathrm{x}} i_{\mathrm{y}} i_{\mathrm{z}}}$, represents the sum of the homogeneous Green functions due to one of the eight sources in a "basic cell" and its translations [70]. Specifically, the basic cell is formed by the source at $\mathbf{r}'$ and its seven images that are closest to the origin; these sources are translated by even multiples of the cavity size in each direction. Thus, the sub-series corresponding to the source located at $\hat{\mathbf{x}}(-1)^{q_{i_{\mathrm{x}}}} x' + \hat{\mathbf{y}}(-1)^{q_{i_{\mathrm{y}}}} y' + \hat{\mathbf{x}}(-1)^{q_{i_{\mathrm{z}}}} z'$ in the basic cell and its translations can be expressed as (for $i_{\mathrm{x,y,z}} \in \{\mathrm{T}, \mathrm{H}\}$)

$$g_{i_{\mathrm{x}} i_{\mathrm{y}} i_{\mathrm{z}}}(\mathbf{r}, \mathbf{r}') = \sum_{p_{\mathrm{x}}=-\infty}^{\infty} \sum_{p_{\mathrm{y}}=-\infty}^{\infty} \sum_{p_{\mathrm{z}}=-\infty}^{\infty} \frac{e^{-\gamma_{\mathrm{cav}} R_{i_{\mathrm{x}} i_{\mathrm{y}} i_{\mathrm{z}}}^{p_{\mathrm{x}} p_{\mathrm{y}} p_{\mathrm{z}}}}}{4\pi R_{i_{\mathrm{x}} i_{\mathrm{y}} i_{\mathrm{z}}}^{p_{\mathrm{x}} p_{\mathrm{y}} p_{\mathrm{z}}}}} \tag{3.2.3}$$

where $\gamma_{\mathrm{cav}} = j\omega\sqrt{\mu_0 \tilde{\varepsilon}_{\mathrm{cav}}}$ is the complex propagation constant in the cavity, the wavelength in the cavity is defined as $\lambda_{\mathrm{cav}} = 2\pi / \mathrm{Im}(\gamma_{\mathrm{cav}})$, $R_{i_{\mathrm{x}} i_{\mathrm{y}} i_{\mathrm{z}}}^{p_{\mathrm{x}} p_{\mathrm{y}} p_{\mathrm{z}}} = \left| \mathbf{R}_{i_{\mathrm{x}} i_{\mathrm{y}} i_{\mathrm{z}}}^{p_{\mathrm{x}} p_{\mathrm{y}} p_{\mathrm{z}}} \right|$ is the distance from the observer to one of the translations of the source, and

$$\begin{aligned}\mathbf{R}_{i_{\mathrm{x}}i_{\mathrm{y}}i_{\mathrm{z}}}^{p_{\mathrm{x}}p_{\mathrm{y}}p_{\mathrm{z}}}(\mathbf{r},\mathbf{r}') &= (x-(-1)^{q_{i_{\mathrm{x}}}}x'-2p_{\mathrm{x}}d_{\mathrm{x}})\hat{\mathbf{x}} \\ &+(y-(-1)^{q_{i_{\mathrm{y}}}}y'-2p_{\mathrm{y}}d_{\mathrm{y}})\hat{\mathbf{y}} \\ &+(z-(-1)^{q_{i_{\mathrm{y}}}}z'-2p_{\mathrm{z}}d_{\mathrm{z}})\hat{\mathbf{z}}\end{aligned} \tag{3.2.4}$$

is the vector pointing from one of the translations of the source to the observer. Notice that R_{TTT}^{000} is 0 and g_{TTT} is singular if $\mathbf{r}=\mathbf{r}'$; in contrast, the other seven sub-series become singular only if $\mathbf{r}=\mathbf{r}'$ *and* $\mathbf{r}$ is on the boundary of the cavity. When $\mathbf{r}=\mathbf{r}'$, there is at most one singular term in each of the eight sub-series; indeed, there are a total of one, two, four, or eight singular terms in the series (3.2.3) when $\mathbf{r}=\mathbf{r}'$ and $\mathbf{r}$ is inside the cavity, on a wall, on an edge, or at a corner, respectively. It should be noted that $p_{\mathrm{x}},p_{\mathrm{y}},p_{\mathrm{z}}\in\{0,1\}$ if $R_{i_{\mathrm{x}}i_{\mathrm{y}}i_{\mathrm{z}}}^{p_{\mathrm{x}}p_{\mathrm{y}}p_{\mathrm{z}}}=0$, i.e., the sources closest to the observer are in the basic cell or its first translations. More generally, $p_{\mathrm{x}},p_{\mathrm{y}},p_{\mathrm{z}}\in\{0,1\}$ whenever the smallest $R_{i_{\mathrm{x}}i_{\mathrm{y}}i_{\mathrm{z}}}^{p_{\mathrm{x}}p_{\mathrm{y}}p_{\mathrm{z}}}$ is obtained in (3.2.3). Thus, each sub-series can be divided into nonsingular and potentially singular terms as

$$\begin{aligned}g_{i_{\mathrm{x}}i_{\mathrm{y}}i_{\mathrm{z}}} &= \underbrace{g_{i_{\mathrm{x}}i_{\mathrm{y}}i_{\mathrm{z}}}-g_{i_{\mathrm{x}}i_{\mathrm{y}}i_{\mathrm{z}}}^{\mathrm{ps}}}_{\text{nonsingular}}+\underbrace{g_{i_{\mathrm{x}}i_{\mathrm{y}}i_{\mathrm{z}}}^{\mathrm{ps}}}_{\text{potentially singular}} \\ g_{i_{\mathrm{x}}i_{\mathrm{y}}i_{\mathrm{z}}}^{\mathrm{ps}} &= \sum_{p_{\mathrm{x}}\in s^{i_{\mathrm{x}}}}\sum_{p_{\mathrm{y}}\in s^{i_{\mathrm{y}}}}\sum_{p_{\mathrm{z}}\in s^{i_{\mathrm{z}}}}\frac{e^{-\gamma_{\mathrm{cav}}R_{i_{\mathrm{x}}i_{\mathrm{y}}i_{\mathrm{z}}}^{p_{\mathrm{x}}p_{\mathrm{y}}p_{\mathrm{z}}}}}{4\pi R_{i_{\mathrm{x}}i_{\mathrm{y}}i_{\mathrm{z}}}^{p_{\mathrm{x}}p_{\mathrm{y}}p_{\mathrm{z}}}}\end{aligned} \tag{3.2.5}$$

where

$$s^{i_{\mathrm{x,y,z}}}=\begin{cases}\{0\} & \text{if } i_{\mathrm{x,y,z}}=\mathrm{T}\\ \{0,1\} & \text{if } i_{\mathrm{x,y,z}}=\mathrm{H}\end{cases} \tag{3.2.6}$$

The triple infinite sub-series in (3.2.3) converges slowly, especially when the operating frequency is close to a cavity resonance [71]. To reduce the cost of computing the Green functions, two methods are adopted here: (i) *Ewald acceleration* [72]-[77]. First,

each of the eight Green function components $g_{i_x i_y i_z}$ is expressed as a sum of two fast converging triple-infinite series by applying the Ewald identity [75] to each term in the summation in (3.2.3), dividing the resulting integral into two sub-integrals using a splitting parameter E, and using Jacobi's imaginary transformation [70]. Truncating these two series to $(2P+1)^3$ terms, each Green function component is approximated as $g_{i_x i_y i_z} \approx g^E_{i_x i_y i_z}$, where

$$g^E_{i_x i_y i_z} = \sum_{p_x=-P}^{P}\sum_{p_y=-P}^{P}\sum_{p_z=-P}^{P} \mathrm{Re}\{\frac{e^{-\gamma_{\mathrm{cav}} R^{p_x p_y p_z}_{i_x i_y i_z}}}{4\pi R^{p_x p_y p_z}_{i_x i_y i_z}} \mathrm{erfc}(R^{p_x p_y p_z}_{i_x i_y i_z} E - \frac{\gamma_{\mathrm{cav}}}{2E})\} + \sum_{p_x=-P}^{P}\sum_{p_y=-P}^{P}\sum_{p_z=-P}^{P} \frac{e^{j\Omega^{p_x p_y p_z}_{i_x i_y i_z}}}{8 d_x d_y d_z} \frac{e^{\frac{-\Delta^{p_x p_y p_z}}{4E^2}}}{\Delta^{p_x p_y p_z}} \tag{3.2.7}$$

Here, $\Omega^{p_x p_y p_z}_{i_x i_y i_z} = [x - x'(-1)^{q_{i_x}}]p_x\pi / d_x + [y - y'(-1)^{q_{i_y}}]p_y\pi / d_y + [z - z'(-1)^{q_{i_z}}]p_z\pi / d_z$; thus, the two series can be interpreted as a weighted combination of truncated image and modal series. In (3.2.7), erfc denotes the complementary error function that decays as $\mathrm{erfc}(x) \sim \exp(-x^2)/x$ for large arguments and $\Delta^{p_x p_y p_z} = (p_x\pi / d_x)^2 + (p_y\pi / d_y)^2 + (p_z\pi / d_z)^2 + \gamma^2_{\mathrm{cav}}$; i.e., both series exhibit faster than Gaussian decay with respect to p_x, p_y, and p_z. The different convergence ratios of the two series can be balanced by choosing

$$E = \sqrt{\pi}[\frac{d_x^{-2} + d_y^{-2} + d_z^{-2}}{d_x^2 + d_y^2 + d_z^2}]^{1/4} \tag{3.2.8}$$

This choice minimizes the truncation error in (3.2.7) for any given P [78],[79] when the electrical size of the cavity is moderate. It causes cancellation between the image and modal series in (3.2.7), however, when implemented in finite precision arithmetic; the

cancellation becomes catastrophic when the cavity is electrically large. To reduce these cancellation errors, E must be chosen differently than the value in (3.2.8) but (in infinite precision arithmetic) this results in either a less accurate Green function value for a given P or a more expensive Green function computation (larger value of P) for a given error level. In other words, when the cavity is electrically large, E and P are dictated not just by the truncation errors in the series in (3.2.7) but also the cancellation of significant digits. In Section 3.6, E is set to (3.2.8) for small cavities but is set to larger values when the minimum cavity side length is more than about $2\lambda_{\text{cav}}$; optimal values of E and P for a prescribed error level can be found as in [78]-[80]. It is important to observe that, just like in (3.2.3), there are potentially singular terms in (3.2.7):

$$g^{E,\text{ps}}_{i_{\text{x}}i_{\text{y}}i_{\text{z}}} = \sum_{p_{\text{x}}\in s^{i_{\text{x}}}} \sum_{p_{\text{y}}\in s^{i_{\text{y}}}} \sum_{p_{\text{z}}\in s^{i_{\text{z}}}} \text{Re}\{\frac{e^{-\gamma_{\text{cav}}R^{p_{\text{x}}p_{\text{y}}p_{\text{z}}}_{i_{\text{x}}i_{\text{y}}i_{\text{z}}}}}{4\pi R^{p_{\text{x}}p_{\text{y}}p_{\text{z}}}_{i_{\text{x}}i_{\text{y}}i_{\text{z}}}} \text{erfc}(R^{p_{\text{x}}p_{\text{y}}p_{\text{z}}}_{i_{\text{x}}i_{\text{y}}i_{\text{z}}}E - \frac{\gamma_{\text{cav}}}{2E})\} \tag{3.2.9}$$

(ii) *Spatial interpolation* [54],[55]. Eight different 3-D tables are constructed to interpolate the Green functions; one for each sub-series $g^{E}_{i_{\text{x}}i_{\text{y}}i_{\text{z}}}$ in (3.2.7). As mentioned above, each sub-series may contain a singular term depending on source and observer location; thus, interpolating the functions $g^{E}_{i_{\text{x}}i_{\text{y}}i_{\text{z}}}$ directly from their samples would not be accurate and only the nonsingular portions $g^{E}_{i_{\text{x}}i_{\text{y}}i_{\text{z}}} - g^{E,\text{ps}}_{i_{\text{x}}i_{\text{y}}i_{\text{z}}}$ are interpolated instead; i.e., each table is filled by sampling the nonsingular portion of one sub-series in the interval of either $x_{\min} - x_{\max} \le x - x' \le x_{\max} - x_{\min}$ or $2x_{\min} \le x + x' \le 2x_{\max}$, either $y_{\min} - y_{\max} \le y - y' \le y_{\max} - y_{\min}$ or $2y_{\min} \le y + y' \le 2y_{\max}$, and either $z_{\min} - z_{\max} \le z - z' \le z_{\max} - z_{\min}$ or $2z_{\min} \le z + z' \le 2z_{\max}$. Here, $x_{\max}$, $y_{\max}$, and $z_{\max}$ ($x_{\min}$, $y_{\min}$, and $z_{\min}$) denote the maximum (minimum) coordinate of the structure of interest in the x, y, and z direction, respectively. In this Chapter, these intervals are

uniformly sampled and 3-D Lagrange interpolation is used. Central interpolation is employed whenever possible but when both the source and observer are close to the cavity walls, backward or forward interpolation has to be utilized; this is similar to the interpolation of layered-medium Green functions when the source and observer are close to layer interfaces [54],[55]. Once the nonsingular portions are interpolated, the results are combined with the potentially singular terms to obtain the desired function values. In short, Ewald acceleration speeds up the evaluation of each series, while interpolation reduces the number of series to be evaluated. The accuracy and efficiency of this approach is investigated numerically in Section 3.6.1.

3.3 MOM

The SV-EFIE is solved using the standard MOM procedure: First, S and V are meshed with triangles that have N^{S} inner edges and tetrahedra that have N^{V} triangular faces, $\tilde{\varepsilon}_{\mathrm{V}}$ in each tetrahedron is assumed constant, N^{S} RWG [22] functions $\mathbf{f}_1^{\mathrm{S}},\ldots,\mathbf{f}_{N^{\mathrm{S}}}^{\mathrm{S}}$ and N^{V} SWG [23] functions $\mathbf{f}_1^{\mathrm{V}},\ldots,\mathbf{f}_{N^{\mathrm{V}}}^{\mathrm{V}}$ are defined, and the unknown current densities are expanded as

$$\{\mathbf{J}^{\mathrm{S}}(\mathbf{r}'),\mathbf{J}^{\mathrm{V}}(\mathbf{r}')\} \cong \{\sum_{n=1}^{N^{\mathrm{S}}}\mathbf{I}^{\mathrm{S}}[n]\mathbf{b}_n^{\mathrm{S}}(\mathbf{r}'),\sum_{n=1}^{N^{\mathrm{V}}}\mathbf{I}^{\mathrm{V}}[n]\mathbf{b}_n^{\mathrm{V}}(\mathbf{r}')\} \tag{3.3.1}$$

where the basis functions are

$$\mathbf{b}_n^{v'}(\mathbf{r}') = \begin{cases} \mathbf{f}_n^{\mathrm{S}}(\mathbf{r}') & \text{if } v' = \mathrm{S} \\ j\omega\chi_n(\mathbf{r}')\mathbf{f}_n^{\mathrm{V}}(\mathbf{r}') & \text{if } v' = \mathrm{V} \end{cases} \tag{3.3.2}$$

In (3.3.2), $\chi_n = 1 - \tilde{\varepsilon}_{\mathrm{cav}} \,/\, \tilde{\varepsilon}_n$ is the complex contrast ratio [23] and $\tilde{\varepsilon}_n$ denotes the (piecewise constant) permittivity in the support of $\mathbf{f}_n^{\mathrm{V}}$. Next, (3.3.1) is substituted in

(3.1.2), the S-EFIE is tested with the functions $\mathbf{t}_1^{\mathrm{S}},\ldots,\mathbf{t}_{N^{\mathrm{S}}}^{\mathrm{S}}$, and the V-EFIE is tested with the functions $\mathbf{t}_1^{\mathrm{V}},\ldots,\mathbf{t}_{N^{\mathrm{V}}}^{\mathrm{V}}$, where

$$\mathbf{t}_k^v(\mathbf{r}) = \begin{cases} \mathbf{f}_k^{\mathrm{S}}(\mathbf{r}) & \text{if } v = \mathrm{S} \\ \chi_k(\mathbf{r})\mathbf{f}_k^{\mathrm{V}}(\mathbf{r}) & \text{if } v = \mathrm{V} \end{cases} \tag{3.3.3}$$

This yields the linear system of equations

$$\begin{bmatrix} \mathbf{Z}^{\mathrm{SS}} & \mathbf{Z}^{\mathrm{SV}} \\ \mathbf{Z}^{\mathrm{VS}} & \mathbf{Z}^{\mathrm{VV}} + \mathbf{D}^{\mathrm{VV}} \end{bmatrix} \begin{bmatrix} \mathbf{I}^{\mathrm{S}} \\ \mathbf{I}^{\mathrm{V}} \end{bmatrix} = \begin{bmatrix} \mathbf{V}^{\mathrm{inc,S}} \\ \mathbf{V}^{\mathrm{inc,V}} \end{bmatrix} \tag{3.3.4}$$

$\mathbf{I}^{v'}$ is the unknown coefficient sub-vector. The entries of the tested incident field sub-vector $\mathbf{V}^{\mathrm{inc},v}$, and the impedance sub-matrix $\mathbf{Z}^{vv'}$ are

$$\begin{aligned} \mathbf{V}^{\mathrm{inc},v}[m] &= \int \mathbf{t}_m^v(\mathbf{r}) \cdot \mathbf{E}^{\mathrm{inc}}(\mathbf{r}) dr \\ \mathbf{Z}^{vv'}[m,n] &= \sum_{i_{\mathrm{x}}\in\{\mathrm{T,H}\}} \sum_{i_{\mathrm{y}}\in\{\mathrm{T,H}\}} \sum_{i_{\mathrm{z}}\in\{\mathrm{T,H}\}} \mathbf{Z}_{i_{\mathrm{x}}i_{\mathrm{y}}i_{\mathrm{z}}}^{vv'}[m,n] \\ \mathbf{Z}_{i_{\mathrm{x}}i_{\mathrm{y}}i_{\mathrm{z}}}^{vv'}[m,n] &= \int \mathbf{t}_m^v(\mathbf{r}) \cdot j\omega \mathbf{A}_{i_{\mathrm{x}}i_{\mathrm{y}}i_{\mathrm{z}},n}^{v'}(\mathbf{r}) + \nabla \cdot \mathbf{t}_m^v(\mathbf{r}) \phi_{i_{\mathrm{x}}i_{\mathrm{y}}i_{\mathrm{z}},n}^{v'}(\mathbf{r}) dr \end{aligned} \tag{3.3.5}$$

for $v, v' \in \{\mathrm{S},\mathrm{V}\}$, $n \in \{1,\ldots,N^{v'}\}$, and $m \in \{1,\ldots,N^{v}\}$. The entries of the Gram matrix are

$$\mathbf{D}^{\mathrm{VV}}[m,n] = \int \chi_m(\mathbf{r}) \mathbf{f}_m^{\mathrm{V}}(\mathbf{r}) \cdot \mathbf{f}_n^{\mathrm{V}}(\mathbf{r}) \,/\, \tilde{\varepsilon}_n(\mathbf{r}) dr \tag{3.3.6}$$

for $m,n \in \{1,\ldots,N^{\mathrm{V}}\}$. In (3.3.5), the contribution of each basis function $\mathbf{b}_n^{v'}$ to the potentials are

$$\begin{aligned} \mathbf{A}_{i_{\mathrm{x}}i_{\mathrm{y}}i_{\mathrm{z}},n}^{v'}(\mathbf{r}) &= \int (\hat{\mathbf{x}}\hat{\mathbf{x}} B_{i_{\mathrm{x}}i_{\mathrm{y}}i_{\mathrm{z}}}^{\mathrm{x}} + \hat{\mathbf{y}}\hat{\mathbf{y}} B_{i_{\mathrm{x}}i_{\mathrm{y}}i_{\mathrm{z}}}^{\mathrm{y}} + \hat{\mathbf{z}}\hat{\mathbf{z}} B_{i_{\mathrm{x}}i_{\mathrm{y}}i_{\mathrm{z}}}^{\mathrm{z}}) g_{i_{\mathrm{x}}i_{\mathrm{y}}i_{\mathrm{z}}}(\mathbf{r},\mathbf{r}') \\ &\qquad \cdot \mathbf{b}_n^{v'}(\mathbf{r}') \mu_0 dr' \\ \phi_{i_{\mathrm{x}}i_{\mathrm{y}}i_{\mathrm{z}},n}^{v'}(\mathbf{r}) &= \int B_{i_{\mathrm{x}}i_{\mathrm{y}}i_{\mathrm{z}}}^{\phi} g_{i_{\mathrm{x}}i_{\mathrm{y}}i_{\mathrm{z}}}(\mathbf{r},\mathbf{r}') \nabla' \cdot \mathbf{b}_n^{v'}(\mathbf{r}') \,/\, (j\omega\tilde{\varepsilon}_{\mathrm{cav}}) dr' \end{aligned} \tag{3.3.7}$$

By employing the methods described in Section 3.2 to approximate the Green functions and by evaluating the integrals of potentially singular terms in (3.2.7) just as in

free space, e.g., by singularity extraction [24], the matrix fill times for structures in rectangular cavities can be reduced to values that are comparable to those for the same structures in free space as shown in Section 2.1. Despite this reduction, the MOM procedure is limited to relatively simple structures and small-scale problems due to its high memory and time requirements. In order to solve more complicated rectangular cavity problems given a fixed computational budget, a fast algorithm that exploits the convolution/correlation form of rectangular-cavity Green functions is presented next.

3.4 AIM

The proposed algorithm is an extension of AIM in Chapter II. Similar to implementations for homogeneous background, the proposed algorithm is also formulated by enclosing the structure of interest with an auxiliary 3-D regular grid composed of N^{3D} nodes. All grid nodes are constrained to be inside or on the cavity walls (Fig. 3.1(b)), i.e., when the structure is touching one or more cavity walls, the auxiliary grid points cannot be placed outside the cavity but can coincide with the walls. The MOM sub-matrices are then approximated as (for $v, v' \in \{\mathrm{S}, \mathrm{V}\}$)

$$\mathbf{Z}^{vv'} \approx \mathbf{Z}^{\mathrm{corr},vv'} + \sum_{i_{\mathrm{x}}\in\{\mathrm{T},\mathrm{H}\}} \sum_{i_{\mathrm{y}}\in\{\mathrm{T},\mathrm{H}\}} \sum_{i_{\mathrm{z}}\in\{\mathrm{T},\mathrm{H}\}} \mathbf{Z}^{\mathrm{FFT},vv'}_{i_{\mathrm{x}}i_{\mathrm{y}}i_{\mathrm{z}}} \tag{3.4.1}$$

where $\mathbf{Z}^{\mathrm{corr},vv'}$ is a pre-corrected sub-matrix and $\mathbf{Z}^{\mathrm{FFT},vv'}_{i_{\mathrm{x}}i_{\mathrm{y}}i_{\mathrm{z}}}$ can be expressed as

$$\begin{bmatrix} \mathbf{Z}^{\mathrm{FFT,SS}}_{i_{\mathrm{x}}i_{\mathrm{y}}i_{\mathrm{z}}} & \mathbf{Z}^{\mathrm{FFT,SV}}_{i_{\mathrm{x}}i_{\mathrm{y}}i_{\mathrm{z}}} \\ \mathbf{Z}^{\mathrm{FFT,VS}}_{i_{\mathrm{x}}i_{\mathrm{y}}i_{\mathrm{z}}} & \mathbf{Z}^{\mathrm{FFT,VV}}_{i_{\mathrm{x}}i_{\mathrm{y}}i_{\mathrm{z}}} \end{bmatrix} = \sum_{l\in\{\mathrm{x,y,z},\phi\}} B^{l}_{i_{\mathrm{x}}i_{\mathrm{y}}i_{\mathrm{z}}} \begin{bmatrix} \mathbf{\Lambda}^{l,\mathrm{S}} & \mathbf{0} \\ \mathbf{0} & \mathbf{\Lambda}^{l,\mathrm{V}} \end{bmatrix}^{\dagger} \mathbf{G}_{i_{\mathrm{x}}i_{\mathrm{y}}i_{\mathrm{z}}} \begin{bmatrix} \tau^{l}\mathbf{\Lambda}^{l,\mathrm{S}} & \mathbf{0} \\ \mathbf{0} & j\omega\tau^{l}\mathbf{\Lambda}^{l,\mathrm{V}} \end{bmatrix}, \quad \text{for } i_{\mathrm{x,y,z}}\{\mathrm{T},\mathrm{H}\} \tag{3.4.2}$$

In (3.4.2), the sub-matrices $\mathbf{\Lambda}^{l,v}$ represent "anterpolation" of currents from basis functions to point sources on the auxiliary grid and the transpose matrices $(\mathbf{\Lambda}^{l,v})^{\dagger}$ represent interpolation of fields from point observers on the auxiliary grid to the testing functions. Each column n of the $\mathbf{\Lambda}^{\mathrm{x},v}$, $\mathbf{\Lambda}^{\mathrm{y},v}$, $\mathbf{\Lambda}^{\mathrm{z},v}$ and $\mathbf{\Lambda}^{\phi,v}$ sub-matrix is filled by matching the multipole moments of M_n^v points to those of the functions $\hat{\mathbf{x}}\cdot\mathbf{t}_n^v$, $\hat{\mathbf{y}}\cdot\mathbf{t}_n^v$, $\hat{\mathbf{z}}\cdot\mathbf{t}_n^v$ and $\nabla\cdot\mathbf{t}_n^v$, respectively. As a result, the $\mathbf{\Lambda}^{l,\mathrm{S}}$ matrices are real sparse matrices of size $N^{3\mathrm{D}}\times N^{\mathrm{S}}$ and $\mathbf{\Lambda}^{l,\mathrm{V}}$ matrices are complex sparse matrices of size $N^{3\mathrm{D}}\times N^{\mathrm{V}}$. The coefficients $\tau^{\mathrm{x,y,z},\phi}$ are $j\omega\mu_0$, $j\omega\mu_0$, $j\omega\mu_0$ and $1/j\omega\tilde{\varepsilon}_{\mathrm{cav}}$ respectively. The propagation matrices $\mathbf{G}_{i_{\mathrm{x}}i_{\mathrm{y}}i_{\mathrm{z}}}$ are dense $N^{3\mathrm{D}}\times N^{3\mathrm{D}}$ matrices that store Green function values from one of the eight sub-series, i.e., $1\le u,u'\le N^{3\mathrm{D}}$

$$\mathbf{G}_{i_{\mathrm{x}}i_{\mathrm{y}}i_{\mathrm{z}}}[u,u'] = \begin{cases} 0 & \text{if } R^{\min}_{i_{\mathrm{x}}i_{\mathrm{y}}i_{\mathrm{z}}}(\mathbf{r}_u,\mathbf{r}_{u'})=0 \\ g_{i_{\mathrm{x}}i_{\mathrm{y}}i_{\mathrm{z}}}(\mathbf{r}_u,\mathbf{r}_{u'}) & \text{else} \end{cases} \tag{3.4.3}$$

where $\{\mathbf{r}_u,\mathbf{r}_v\}$ denotes the position of the {observer, source} point on the auxiliary grid and $R^{\min}_{i_{\mathrm{x}}i_{\mathrm{y}}i_{\mathrm{z}}}(\mathbf{r}_u,\mathbf{r}_{u'}) = \min\left|\mathbf{R}^{p_{\mathrm{x}}p_{\mathrm{y}}p_{\mathrm{z}}}_{i_{\mathrm{x}}i_{\mathrm{y}}i_{\mathrm{z}}}(\mathbf{r}_u,\mathbf{r}_{u'})\right|$. In (3.4.3), the singular terms in the sub-series are replaced with zeros; in other words, the Green functions are "softened" [41]. As a result, the diagonal of $\mathbf{G}_{\mathrm{TTT}}$ is zero; in contrast, only some diagonal entries of the other seven propagation matrices are zero; these correspond to grid points that reside on the cavity walls, edges, or corners.

The pre-corrected sub-matrices are sparse matrices whose entries are given in (3.4.5). N^{corr} also denotes the total number of non-zero entries in the four $\mathbf{Z}^{\mathrm{corr},vv'}$ sub-matrices. The value of N^{corr} is also controlled by the integer γ and the minimum "grid distance" [39] between the functions $\mathbf{t}_m^v$ and $\mathbf{b}_n^{v'}$ as defined in Section 2.2:

$$\mathrm{dist}^{vv'}_{i_{\mathrm{x}}i_{\mathrm{y}}i_{\mathrm{z}}}[m,n]=\min_{u\in M_m^v,u'\in M_n^{v'},p_{\mathrm{x}},p_{\mathrm{y}},p_{\mathrm{z}}}\max\Bigg(\left\lfloor\frac{|\,\hat{\mathbf{x}}\cdot\mathbf{R}^{p_{\mathrm{x}}p_{\mathrm{y}}p_{\mathrm{z}}}_{i_{\mathrm{x}}i_{\mathrm{y}}i_{\mathrm{z}}}(\mathbf{r}_u,\mathbf{r}_{u'})\,|}{\Delta_{\mathrm{x}}}\right\rfloor,\left\lfloor\frac{|\,\hat{\mathbf{y}}\cdot\mathbf{R}^{p_{\mathrm{x}}p_{\mathrm{y}}p_{\mathrm{z}}}_{i_{\mathrm{x}}i_{\mathrm{y}}i_{\mathrm{z}}}(\mathbf{r}_u,\mathbf{r}_{u'})\,|}{\Delta_{\mathrm{y}}}\right\rfloor,\left\lfloor\frac{|\,\hat{\mathbf{z}}\cdot\mathbf{R}^{p_{\mathrm{x}}p_{\mathrm{y}}p_{\mathrm{z}}}_{i_{\mathrm{x}}i_{\mathrm{y}}i_{\mathrm{z}}}(\mathbf{r}_u,\mathbf{r}_{u'})\,|}{\Delta_{\mathrm{z}}}\right\rfloor,\Bigg) \tag{3.4.4}$$

where $\Delta_{\mathrm{x,y,z}}$ denote the auxiliary grid spacing in the three Cartesian directions and $\lfloor\cdot\rfloor$ denotes the greatest integer less than or equal to its argument. Each of the eight sub-series in the $\mathbf{Z}^{\mathrm{corr},vv'}$ expression in (3.4.5) can have a different number of non-zero entries, i.e., each non-zero entry in $\mathbf{Z}^{\mathrm{corr},vv'}$ can be a combination of one, two, four, or eight terms: If $\mathbf{Z}^{\mathrm{corr},vv'}[m,n]$ is not zero then $\mathrm{dist}^{vv'}_{\mathrm{TTT}}[m,n]$ and one, three, or seven other distances are less than γ depending on whether the corresponding testing and basis functions are near a wall, edge, or corner of the cavity. Therefore, different from the algorithms in Chapters II and V, where the pre-corrected matrix replaces the interaction between basis-testing functions computed from auxiliary grid with the original impedance matrix entry, the $\mathbf{Z}^{\mathrm{corr},vv'}$ matrix in (3.4.1) replaces only part of the contribution from the auxiliary grid with part of original impedance matrix entry. For example, when the structure of interest is away from the cavity walls, only one term is used, i.e., only $\mathbf{Z}^{\mathrm{FFT},vv'}_{\mathrm{TTT}}$ term is corrected, because the contributions from the other seven terms are accurately approximated by the seven $\mathbf{Z}^{\mathrm{FFT},vv'}_{i_{\mathrm{x}}i_{\mathrm{y}}i_{\mathrm{z}}}$ matrices.

$$\mathbf{Z}^{\mathrm{corr},vv'}[m,n]=\begin{cases}\displaystyle\sum_{i_{\mathrm{x}}\in\{\mathrm{T,H}\}}\sum_{i_{\mathrm{y}}\in\{\mathrm{T,H}\}}\sum_{i_{\mathrm{z}}\in\{\mathrm{T,H}\}}\mathbf{Z}^{vv'}_{i_{\mathrm{x}}i_{\mathrm{y}}i_{\mathrm{z}}}[m,n]-\mathbf{Z}^{\mathrm{FFT},vv'}_{i_{\mathrm{x}}i_{\mathrm{y}}i_{\mathrm{z}}}[m,n], & \text{if } \mathrm{dist}^{vv'}_{i_{\mathrm{x}}i_{\mathrm{y}}i_{\mathrm{z}}}[m,n]<\gamma\\ 0, & \text{else}\end{cases} \tag{3.4.5}$$

Unlike for structures in homogeneous background in Chapter II, where the AIM propagation matrices have a 3-level block-Toeplitz structure, the AIM propagation

matrices in (3.4.3) have a TTT, TTH, THT, THH, HTT, HTH, HHT, or HHH structure. It was shown in the previous Chapter that $\mathbf{G}_{\mathrm{TTT}}$ matrix can be efficiently multiplied with vectors using 3-D FFTs. Here, a similar approach is used to multiply the other seven types of propagation matrices with vectors. That is, block-anti-diagonal permutation matrices $\mathbf{Q}_{i_x i_y i_z}$ are used to convert the Hankel blocks to Toeplitz ones; specifically, a total of seven different $\mathbf{Q}_{i_x i_y i_z}$ matrices are used, e.g., $\mathbf{Q}_{\mathrm{HHH}}$ is a (3-level) block-anti-diagonal permutation matrix and $\mathbf{Q}_{\mathrm{HTH}}$ is an block-anti-diagonal-block-diagonal-block-anti-diagonal permutation matrix. These permutation matrices reduce the multiplications between the propagation matrices and vectors to multiplying TTT matrices with reordered vectors. For example, consider the multiplication of $\mathbf{G}_{\mathrm{HHH}}$ with the (anterpolated) vector $\mathbf{I}$: $\mathbf{G}_{\mathrm{HHH}}\mathbf{I} = (\mathbf{G}_{\mathrm{HHH}}\mathbf{Q}_{\mathrm{HHH}})(\mathbf{Q}_{\mathrm{HHH}}^{-1}\mathbf{I})$. Here, $\mathbf{Q}_{\mathrm{HHH}}^{-1}\mathbf{I}$ reorders the vector $\mathbf{I}$ and $\mathbf{G}_{\mathrm{HHH}}\mathbf{Q}_{\mathrm{HHH}}$ is a TTT matrix; thus, the matrix $\mathbf{G}_{\mathrm{HHH}}\mathbf{Q}_{\mathrm{HHH}}$ and the vector $\mathbf{Q}_{\mathrm{HHH}}^{-1}\mathbf{I}$ can be multiplied in three stages by (i) forming two 3-D arrays, which contain the unique entries of the matrix and zero-padded version of the vector, and computing their 3-D FFTs, (ii) multiplying the resulting arrays element by element, and (iii) computing the inverse 3-D FFT of the resulting array. This is just like the procedure for computing $\mathbf{G}_{\mathrm{TTT}}\mathbf{I}$; indeed, the 3-D FFTs needed while computing $\mathbf{G}_{\mathrm{TTT}}\mathbf{I}$ can be recycled because the 3-D FFT of the array formed from $\mathbf{Q}_{\mathrm{HHH}}^{-1}\mathbf{I}$ is simply a reordered version of the 3-D FFT of the array formed from $\mathbf{I}$ multiplied element-by-element with a phase shift [54],[55]. In short, if the 3-D FFT of the eight propagation matrices $\mathbf{G}_{i_x i_y i_z}$ are pre-computed and stored before the iterative solution, then at each iteration the $\mathbf{G}_{i_x i_y i_z}\mathbf{I}$ multiplication can be computed with no additional FFTs after computing $\mathbf{G}_{\mathrm{TTT}}\mathbf{I}$.

If the above correction and propagation procedures are used, the matrix fill time, memory cost, and matrix solve time of the proposed AIM scale as $O(N^{\mathrm{corr}} + N^{\mathrm{3D}})$, $O(N^{\mathrm{corr}} + N^{\mathrm{3D}})$, and $O(N^{\mathrm{corr}} + N^{\mathrm{3D}} \log N^{\mathrm{3D}})$ per iteration, respectively. If the structure of interest consists of (i) only a PEC surface, N^{3D} is $\sim N$ if the surface is quasi-planar and $N^{\mathrm{3D}} \sim N^{1.5}$ if it is a 3-D surface because N^{3D} is proportional to the volume enclosing the structure and $N = N^{\mathrm{S}}$ is proportional to the area of the structure; (ii) only a dielectric volume, N^{3D} is $\sim N$ because both N^{3D} and $N = N^{\mathrm{V}}$ are proportional to the volume of the structure [39],[40][54],[55]; and (iii) both a PEC surface and a dielectric volume, $N^{\mathrm{3D}} \sim N - N^{1.5}$ depending on the number of surface and volume unknowns. For single-scale problems, where the mesh lengths do not vary significantly over the structure, $N^{\mathrm{corr}} \sim N$ [59]. Note that for structures away from the cavity walls, AIM reduces the MOM matrix fill time more significantly than other cases because only one of the eight Green function sub-series is evaluated when computing the impedance matrix contribution to the $\mathbf{Z}^{\mathrm{corr},vv'}$ matrices in (3.4.1); in contrast, all eight sub-series must be computed when filling the impedance sub-matrices $\mathbf{Z}^{vv'}$ in MOM.

3.5 COMPARISON TO FREE SPACE

Next, the proposed method is contrasted to the classical AIM for analyzing scattering from 3-D structures in homogeneous background. In the following it is assumed that all AIM parameters are the same whether the structure resides in free space or a rectangular cavity; this assumption is supported by the results in Section 3.6.2. In this case, the matrix fill time of the proposed method would be comparable to that in the free-space case if the Ewald acceleration and interpolation can successfully reduce the Green function

computation costs; the memory requirement and matrix solution costs are contrasted to the free-space case next.

In free space, the AIM procedure can be expressed as $\mathbf{Z}_{\text{free}}^{vv'} = \mathbf{Z}^{\text{corr},vv'} + \mathbf{Z}^{\text{FFT},vv'}$ (for $v, v' \in \{\text{S}, \text{V}\}$), where both matrices are formed by using the free-space Green function, e.g.,

$$\begin{bmatrix} \mathbf{Z}_{\text{FFT}}^{\text{SS}} & \mathbf{Z}_{\text{FFT}}^{\text{SV}} \\ \mathbf{Z}_{\text{FFT}}^{\text{VS}} & \mathbf{Z}_{\text{FFT}}^{\text{VV}} \end{bmatrix} = \sum_{l \in \{\text{x},\text{y},\text{z},\phi\}} \begin{bmatrix} \mathbf{\Lambda}^{l,\text{S}} & \mathbf{0} \\ \mathbf{0} & \mathbf{\Lambda}^{l,\text{V}} \end{bmatrix}^{\dagger} \mathbf{G}_{\text{TTT}}^{000} \begin{bmatrix} \tau^{l} \mathbf{\Lambda}^{l,\text{S}} & \mathbf{0} \\ \mathbf{0} & j\omega\tau^{l} \mathbf{\Lambda}^{l,\text{V}} \end{bmatrix} \tag{3.5.1}$$

Unlike in (3.4.2), there are not eight but only one propagation matrix $\mathbf{G}_{\text{TTT}}^{000}$, whose entries are the $p_{\text{x}} = p_{\text{y}} = p_{\text{z}} = 0$ term in the g_{TTT} sub-series, i.e., the free-space Green function. To multiply the $\mathbf{Z}^{\text{FFT}}$ matrix, four FFTs, four element-by-element multiplications, and four inverse FFTs (one for each $l \in \{\text{x}, \text{y}, \text{z}, \nabla\}$) are computed at each iteration as in Section 2.2. These four computations can be performed one at a time by using only two arrays of size $\sim 8N^{\text{3D}}$: One for storing the pre-computed FFT of the array formed from $\mathbf{G}_{\text{TTT}}^{000}$ and one for storing the result of the FFT of the zero-padded arrays, the element-by-element multiplication, and the inverse FFTs.

In a rectangular cavity, a straightforward implementation of the AIM procedure would be to compute the stages for each of the eight sub-series and for each $l \in \{\text{x}, \text{y}, \text{z}, \nabla\}$ one at a time. In this case, multiplying the $\mathbf{Z}_{i_{\text{x}} i_{\text{y}} i_{\text{z}}}^{\text{FFT},vv'}$ matrices in (3.4.1) would require thirty-two FFTs, element-by-element multiplications, and inverse FFTs to be computed at each iteration, which can be performed by storing nine arrays of size $\sim 8N^{\text{3D}}$ (eight for pre-computed and one for on-the-fly FFTs). A better approach is to minimize the FFTs and inverse FFTs by recycling the FFTs of the zero-padded arrays [54],[55] and by combining the eight sub-series before the inverse FFT step, i.e., changing the order of summations in

(3.4.1) and (3.4.2). This requires four FFTs, thirty-two element-by-element multiplications, and four inverse FFTs at each iteration, which can be performed by storing eleven arrays of size $\sim 8N^{3\mathrm{D}}$. Because FFT and inverse FFT costs scale as $N^{3\mathrm{D}} \log N^{3\mathrm{D}}$ while multiplication cost scales as $N^{3\mathrm{D}}$, *the AIM cost per iteration should become comparable to free-space case for large enough problems*. The AIM memory requirement, however, would increase from $\sim N^{\mathrm{corr}} + 16N^{3\mathrm{D}}$ to $\sim N^{\mathrm{corr}} + 88N^{3\mathrm{D}}$. Typically, $N^{\mathrm{corr}} \gg N^{3\mathrm{D}}$ for quasi-planar PEC surfaces and dielectric volumes while N^{corr} can be comparable or (for large problems) much smaller than $N^{3\mathrm{D}}$ for 3-D surfaces; thus, the AIM memory requirement would be 1 to 3.5 times that in the free-space case depending on the shape of the structure and the number of surface and volume unknowns.

3.6 NUMERICAL RESULTS

This section presents several numerical results to demonstrate the performance of the proposed method. First, the accuracy of the rectangular-cavity Green function computation described in Section 3.2 is quantified. Next, the computational complexity of AIM is validated by analyzing the power absorbed by a steak model in a rectangular cavity. Then various problems are solved and the results are compared to independent references. In all simulations, the AIM parameters (except the grid spacings), the preconditioner, and the iterative solver tolerance are the same as those described in Section 2.3. The proposed method is parallelized using an MPI-based implementation of the algorithm as in Chapter II and all simulations are performed on the Lonestar cluster. The reported timing and memory data were “serialized” as described in Section 2.3.

3.6.1 Green Function Accuracy

The accuracy of the Green function computations is investigated by using the relative error norm

$$err_{i_x i_y i_z} = \max_{\mathbf{r}' \in \text{cavity}} \left(\frac{\sum_{\substack{\mathbf{r} \in \text{cavity} \\ \mathbf{r} \neq \mathbf{r}'}} \left| g^{E}_{i_x i_y i_z}(\mathbf{r}, \mathbf{r}') - g^{E,\text{ref}}_{i_x i_y i_z}(\mathbf{r}, \mathbf{r}') \right|^2}{\sum_{\substack{\mathbf{r} \in \text{cavity} \\ \mathbf{r} \neq \mathbf{r}'}} \left| g^{E,\text{ref}}_{i_x i_y i_z}(\mathbf{r}, \mathbf{r}') \right|^2} \right)^{1/2} \tag{3.6.1}$$

This error is computed using 101^3 source/observer points distributed uniformly in an air-filled rectangular cavity, i.e., $\tilde{\varepsilon}_{\text{cav}}$ is equal to the free-space permittivity ε_0. Three different cavities, which are also employed in Sections 3.6.2 and 3.6.3, are simulated. These cavities are of size $1 \times 1 \times 1 \text{ m}^3$, $12.5 \times 8.5 \times 6 \text{ m}^3$, and $0.45 \times 0.42 \times 0.35 \text{ m}^3$; they are operated at 425 MHz, 82 MHz, and 2.45 GHz; and the minimum cavity side length is about $1.64\lambda_{\text{cav}}$, $1.42\lambda_{\text{cav}}$, $2.86\lambda_{\text{cav}}$, respectively.

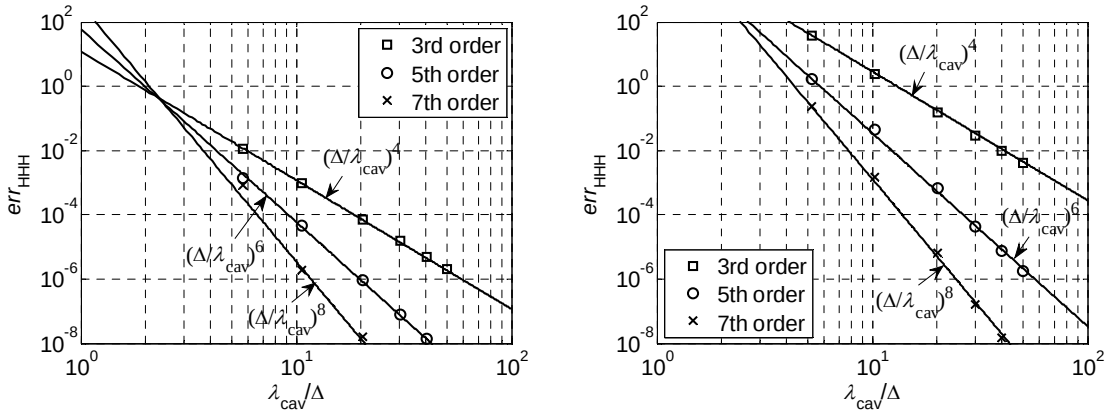

Figure 3.2: Interpolation error vs. the sampling interval size for three different interpolation orders when $P = 9$. (a) Cavity 1. (b) Cavity 2. (c) Cavity 3.

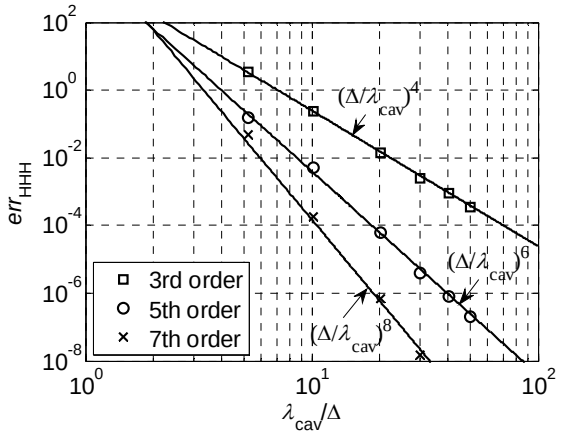

(c)

Figure 3.2: Continued.

First, the accuracy of the 3-D spatial interpolation is quantified by using the error norm in (3.6.1). Here, $g^{E,\mathrm{ref}}_{i_x i_y i_z}$ is directly computed using (3.2.7) with $P = 10$ and E is set as in (3.2.8) even for the largest cavity; to keep enough effective digits in this case, quadruple precision arithmetic is employed. The $g^{E}_{i_x i_y i_z}$ values are interpolated from a table that stores samples as detailed in Section 3.2; these samples are computed by fixing P to 9 and setting E is as in (3.2.8) when the minimum cavity side length is smaller than $2\lambda_{\mathrm{cav}}$ and to 1.5 times the value in (3.2.8) otherwise [80]. The error is calculated for different interpolation orders and sampling intervals Δ. Here, Δ are slightly different in the three Cartesian coordinates for cavity 2 and 3 because they are rectangular, but the difference are only about 1% and thus have negligible effect on the results in Fig. 3.2. The resulting data are plotted in Figs. 3.2(a)-(c) for the three cavities; Fig. 3.2 shows that all interpolation errors converge according to the polynomial order of the interpolant, that they can be very different for different cavities/frequencies, and that for these three cavities,

the interpolation errors are less than 10^{-3} error level when about 20 samples per wavelength and 5th order interpolation are used. Based on these results, P is set to 9, E is either set according to (3.2.8) or—if the minimum cavity dimension is larger than $2\lambda_{\text{cav}}$—set 1.5 times the value in (3.2.8) when filling the interpolation table in all the following simulations. In addition, 5th order Lagrange interpolation with approximately 20 samples per λ_{cav} is used to interpolate the Green functions.

Next, the accuracy of the resulting Green function computations is demonstrated in Fig. 3.3 by comparing g_{cav}^{zz}, which includes all eight sub-series, to an independent reference [71]. Here, the *z*-directed Hertzian dipole is located at $x = y = z = 0.25L$ and the observation points are distributed along the diagonal of the cavity. The results in Fig. 3.3 show good agreement with those in [71].

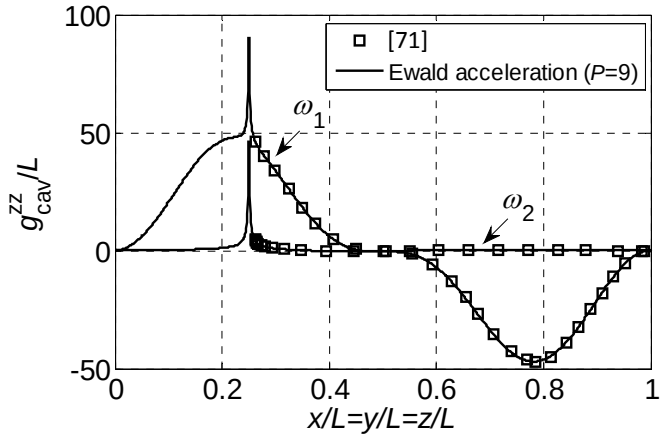

Figure 3.3: One of the Green function components along the cavity diagonal when $P = 9$ and 5th order interpolation is used with 20 samples per wavelength.

3.6.2 Computational Complexity

The computational complexity of the proposed scheme is verified by analyzing scattering from a homogeneous steak model in cavity 3. The procedure is the same as in Section 2.3.1 except the steak is centered in the middle of a rectangular cavity. All the AIM parameters for the cavity and free space simulations are the same and detailed in Table 3.1, which shows that the errors in the cavity and free space simulations are similar when the same AIM parameters are used. The total time-average power absorbed by the steak models are about 1.4×10^4 W and 8.3×10^2 W in the cavity and free space, respectively.

Table 3.1: Parameters for analyzing scattering from a steak model in free space and in a rectangular cavity

Average edge length	N	N^{3D}	Reference	err_{L1}^{P} (%)	
				Cavity	Free space
δ / 1.7	1168	$30 \times 30 \times 7$	MOM/AIM	0.16/0.17	0.15/0.15
δ / 3.7	10 048	$54 \times 54 \times 9$	MOM/AIM	0.53/0.51	0.35/0.35
δ / 7.3	77 002	$105 \times 105 \times 14$	MOM/AIM	0.75/0.72	0.57/0.57
δ / 14.7	585 236	$224 \times 224 \times 25$	AIM	0.32	0.32

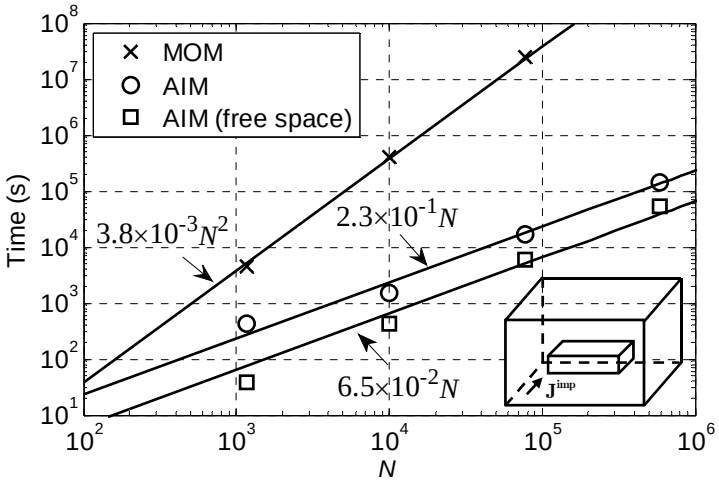

(a)

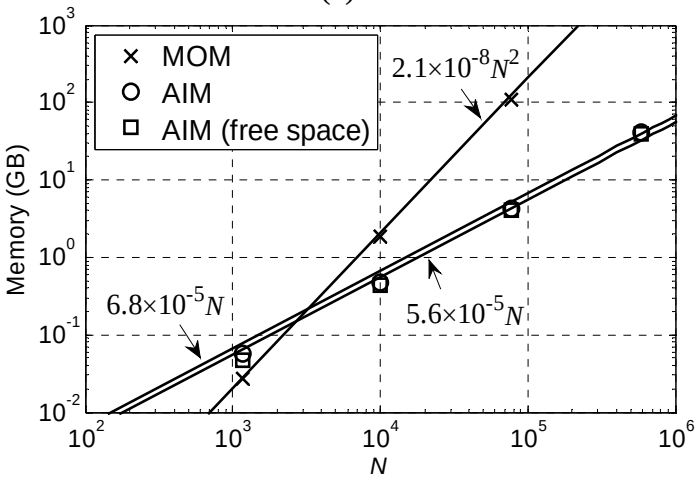

(b)

Figure 3.4: AIM vs. MOM for a steak model in cavity 3 as the mesh density of the steak is increased. (a) Matrix fill time. (b) Memory requirement. (c) Average solution time per iteration.

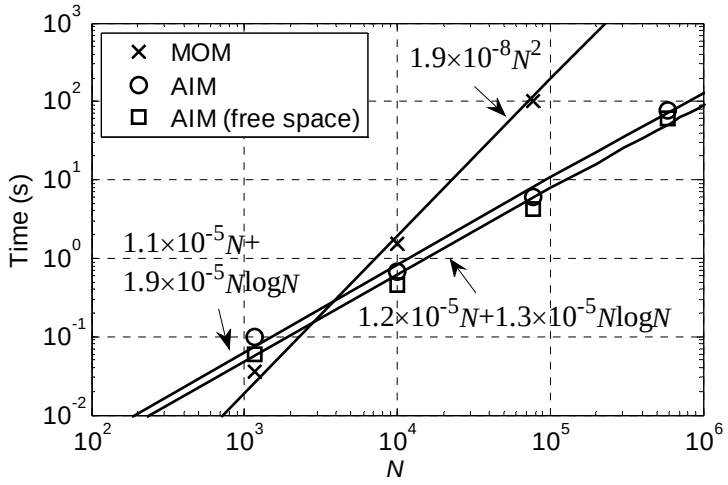

(c)

Figure 3.4: Continued.

The observed computational costs of AIM and MOM simulations are shown in Figs. 3.4(a)-(c); the costs of AIM simulations when the background is free space are also shown. The curves that are fitted to the observed data in Fig. 3.4 are in line with the complexity expressions in Section 3.4. Fig. 3.4(a) shows that AIM outperforms MOM in the matrix fill time requirement starting at $N \approx 100$; this is about 10 times better than the typical crossover point in free space. As described in Section 3.4, this is because the scattering volume is away from all cavity walls and the AIM near-zone correction is required only for the $\mathbf{G}_{\mathrm{TTT}}$ term. In other words, when the background medium is modified from free space to a rectangular cavity, the matrix-fill times of AIM simulations increase not as much as those of MOM simulations. In fact, the AIM matrix-fill times for cavity simulations are about 3.5 times those for free-space simulations. Note that the time needed to fill the interpolation table is included in the matrix fill time and is negligible.

Figs. 3.4(b)-(c) show that AIM outperforms MOM in memory and matrix solution time for $N \approx 3500$, which is comparable to the method's performance for layered media [54],[55]. The AIM memory and matrix solution time requirements for cavity simulations are about 1.2 and 1.5 times those for free-space simulations, respectively; both the memory and solve time requirements are in line with the predictions from the analysis in Section 3.5. The number of iterations N^{it} varied from 316 to 532.

3.6.3 Validation

Next, the viability of the proposed scheme for solving scattering problems is demonstrated by analyzing two scenarios: Wire antennas in a square cavity [69] and plate stirrers in a reverberation chamber [81].

In the first scenario, three z directed thin wires are located in cavity 1, which is filled with a lossy material such that $\varepsilon_{\text{cav}} = \varepsilon_0$ and $\sigma_{\text{cav}} = 1.0 \times 10^{-4}\ \text{S/m}$. The first, second, and third wire is 0.22 m, 0.2 m, and 0.2 m long and is centered at $(0.2\ \text{m}, 0.5\ \text{m}, 0.3\ \text{m})$, $(0.2\ \text{m}, 0.5\ \text{m}, 0.81\ \text{m})$, and $(0.2\ \text{m}, 0.9\ \text{m}, 0.5\ \text{m})$, respectively. The first wire is excited in the center by a 1V delta-gap source at 425 MHz. The wires are modeled as flat strips with width equal to 4 times the wire radius of 1.0 mm in the xoz plane [82]. They are discretized using triangles with 3.83 mm (around $\lambda_{\text{cav}} / 184$) average edge length resulting in $N = 397$ RWG functions. The unusually small average edge lengths here and in the following simulation are caused by the small widths of the strips. The AIM auxiliary grid spacing is chosen as $3.53\ \text{cm}$ (about $\lambda_{\text{cav}} / 20$) in each Cartesian direction, which yields $N^{\text{3D}} = 21 \times 15 \times 24$. The scattered electric field $\mathbf{E}^{\text{sca}}$ is calculated on an observation line from $(0.3\ \text{m}, 0.9\ \text{m}, 0.05\ \text{m})$ to

$(0.3\ \mathrm{m}, 0.9\ \mathrm{m}, 0.95\ \mathrm{m})$. The results found from AIM and MOM simulations are compared to a reference MOM solution using the thin wire EFIE [69] in Fig. 3.5. The MOM and AIM results agree well but are slightly different from the reference mainly because the thin wires are modeled as strips here. The AIM (MOM) simulation required approximately 653.7 (868.9) seconds to fill the matrices, 59.0 (45.0) MB of memory, and 7.5×10^{-2} (1.7×10^{-3}) seconds per iteration; the iterative solution converged in 71 (79) iterations.

In the second scenario, a plate stirrer that is 8 m long in x direction and 0.8 m wide in the y direction is placed in cavity 2, which is filled with $\varepsilon_{\text{cav}} = \varepsilon_0$ and $\sigma_{\text{cav}} = 2.2\times10^{-6}\ \mathrm{S/m}$. The center of the stirrer is located at $(6.25\ \mathrm{m}, 6.6\ \mathrm{m}, 4.25\ \mathrm{m})$ and the cavity is excited by a Hertzian dipole with a magnitude of $\sqrt{3}$ at 82 MHz, which is located at $(10.5\ \mathrm{m}, 2\ \mathrm{m}, 1.6\ \mathrm{m})$ and points in the $(-\hat{\mathbf{x}}+\hat{\mathbf{y}}+\hat{\mathbf{z}})/\sqrt{3}$ direction. The surface of the stirrer is discretized using triangles with 0.18 m (roughly $\lambda_{\text{cav}}/20$) average edge length resulting in $N = 617$ RWG functions. The auxiliary grid spacing is 0.18 m (around $\lambda_{\text{cav}}/20$) in all three directions and $N^{3\text{D}} = 48\times9\times4$. The magnitude of total electric fields on the observation line from $(2\ \mathrm{m}, 1\ \mathrm{m}, 3\ \mathrm{m})$ to $(2\ \mathrm{m}, 7.5\ \mathrm{m}, 3\ \mathrm{m})$ are calculated with the proposed AIM and compared to independent results in Fig. 3.6. The reference results in [81] are obtained by separately modeling the stirrer using MOM and cavity using the discrete singular convolution method and coupling these two methods using boundary conditions. This AIM (MOM) simulation required approximately 442.2 (112.8) seconds for filling the matrices, 51.0 (47.0) MB memory, and 2.0×10^{-2}

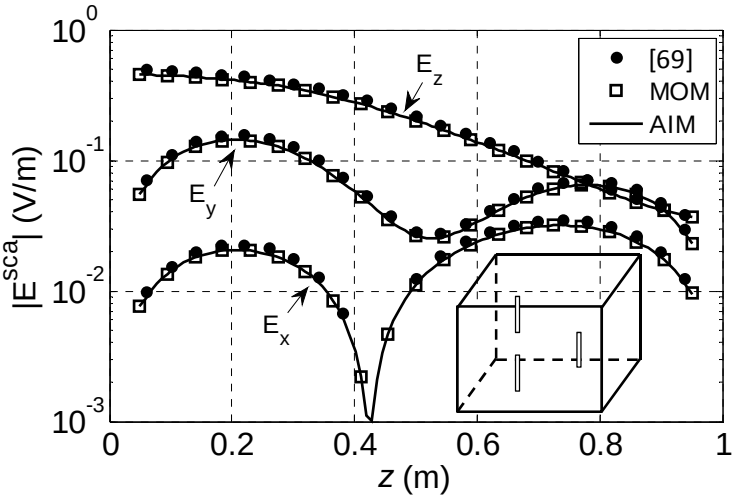

Figure 3.5: Electric field in cavity 1 loaded with thin three wire antennas.

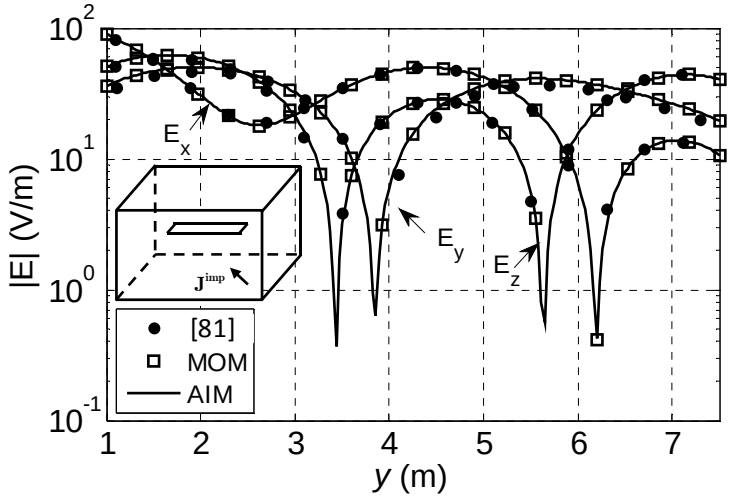

Figure 3.6: Electric field in cavity 2 loaded with a single plate stirrer.

(3.6×10^{-3}) seconds per iteration; the iterative solution converged in 69 (69) iterations.

3.7 SUMMARY

This Chapter presented an FFT-accelerated integral-equation method for efficient analysis of scattering from 3-D single-scale structures composed of PEC surfaces and lossy dielectric volumes with irregular geometries in a rectangular cavity. The proposed method decomposes rectangular-cavity Green function components into eight terms that are in convolution or correlation form in the three Cartesian directions and accelerates the MOM procedure by exploiting the form of these components using FFTs. The proposed AIM for rectangular cavity problems was contrasted in detail to its counterpart for free space problems. The results show that the matrix fill time can be about 3.5 times larger for structures away from cavity walls compared to free space simulations by using interpolation and Ewald method to accelerate the evaluation of rectangular-cavity Green functions; the matrix fill time is expected to be at most about 30 times for structures touching all six cavity walls compared to free space simulations. The memory and the matrix solve time (per iteration) requirement of the method are approximately 1.2 and 1.5 times for rectangular cavity simulations compared to the corresponding requirement for free space simulations. Similar to the AIM scheme in Chapter II, the proposed extension of AIM can accurately and efficiently solve type 1a and 1b multi-scale problems in a rectangular-cavity background when the structures under study only contain a single length scale.

Chapter IV: FFT-Truncated Multilevel Interpolation Method for Homogeneous Backgrounds

This Chapter presents an FFT-truncated multilevel interpolation method (FFT-MLIM) for analyzing scattering from multi-scale structures in homogeneous backgrounds (type 2 multi-scale problems). Section 4.1 presents the proposed FFT-MLIM algorithm, which is a "box centric" oct-tree implementation of the multigrid method truncated by "grid centric" FFTs. Section 4.2 presents numerical results evaluating the accuracy and efficiency of the FFT-MLIM.

4.1 FORMULATION

Consider scattering from a multi-scale 3-D PEC-dielectric structure as shown in Fig. 4.1. First, volume and surface integral equations are formulated as in Section 3.1 and solved using the MOM procedure as in Section 3.3. Then, the FFT-MLIM algorithm is formulated.

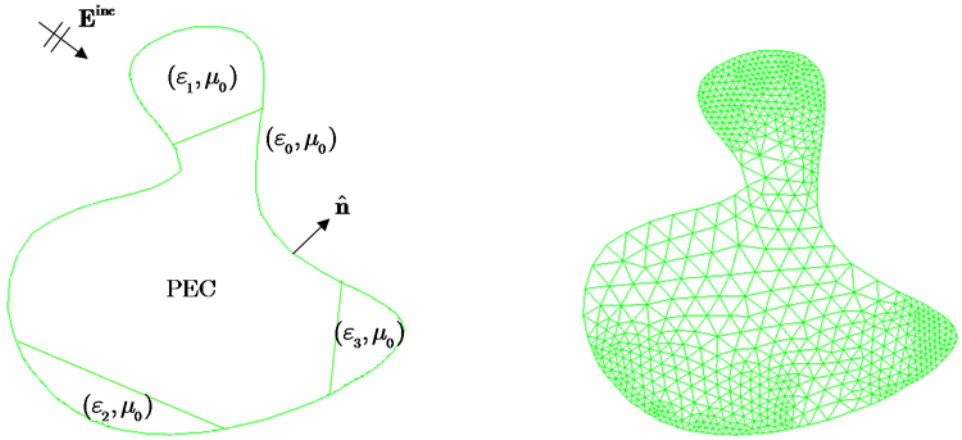

(a) (b)

Figure 4.1: Scattering from an arbitrarily shaped penetrable multi-scale structure. (a) Geometry and excitation. (b) The multi-scale mesh.

4.1.1 FFT-MLIM Algorithm

A truncated oct-tree is constructed as follows (Fig. 4.2): First, a level-0 box that has side length d is used to enclose V. Then, at each level l ($l = 0,\ldots,L$), the non-empty/dense boxes (parent boxes) are divided into 8 equally sized (children) boxes down to level L; thus, there are $NB_l \leq 8^l$ boxes of side length $d_l = d / 2^l$ at level l. The primary mesh of the structure is considered level $L+1$ of the tree. Next, each level l is classified as a "high-frequency (HF) level" or a "low-frequency (LF) level" according to the ratio of the side lengths of the boxes at that level and the pertinent wavelength/skin depth. The oct-tree is truncated at the "truncation (T) level" T which is defined as the low-frequency level that is highest in the hierarchy (has the smallest l). For example, in Fig. 4.2(b), level 0 to level 2 are categorized as HF levels, levels 3 and 4 are LF levels, and level 3 is the T level.

After the truncated oct-tree is constructed, each non-empty box is assigned a unique id b_l ($1 \le b_l \le NB_l$), a parent id $PB(b_l)$, children ids $CB(b_l)$, a far interaction list $FIL(b_l)$, and near interaction list $NIL(b_l)$. Note that boxes at level L do not have children boxes; instead, $CB(b_l)$ is the set of basis functions on the primary mesh whose center of support are inside box b_L. The near and far interaction lists are constructed as follows: At each level $l+1$ ($l = T-1,\ldots,L-1$), if the center to center distance between box A and box B is less than (larger than) a preset buffer number multiplied by d_{l+1} and if the distance between their parent boxes at level l is less than a preset buffer number multiplied by d_l, then box B is in $NIL(A)$ ($FIL(A)$) and box A is in $NIL(B)$ ($FIL(B)$) [87]. Boxes at a given level that are not in the far interaction lists of each other do not interact at that level. The far interactions are computed via auxiliary grids and FFTs at all levels, while the near interactions are computed only at level L directly between the basis in source and observer boxes.

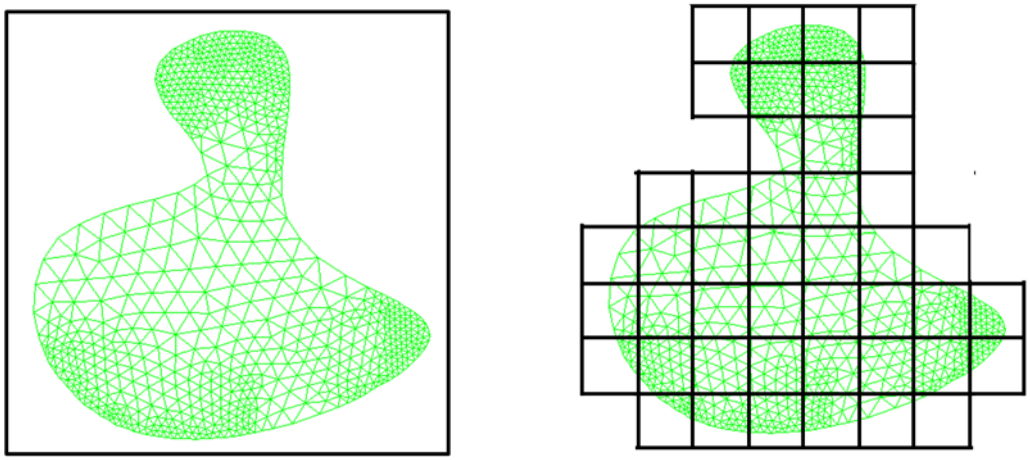

(a)

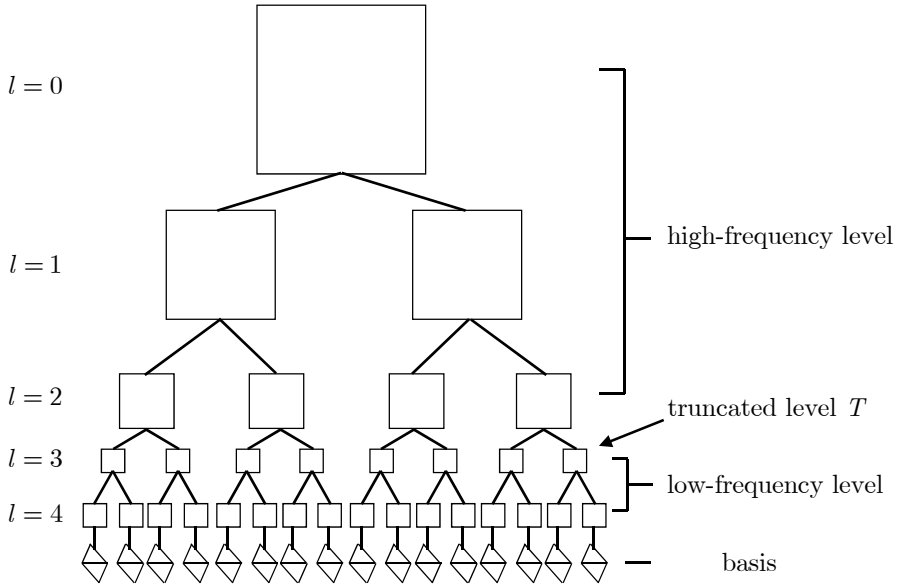

(b)

Figure 4.2: Multilevel division of a 3-D structure. (a) Illustration of the level-0 (left) and level-3 boxes (right). (b) The corresponding 4-level oct-tree. Only 2 of the 8 child boxes at each level are shown.

To traverse the oct-tree, auxiliary regular grids are introduced at each box and Lagrange anter/interpolation is used similar to [42],[43],[88]. For LF levels, the number of grid points per box can be fixed and the grid spacing can be proportionally larger for higher levels (smaller l); whereas for HF levels, the grid spacing must be fixed (to a fraction of the wavelength/skin depth) and the number of grid points per box must increase proportionally for higher levels to maintain accuracy. Therefore, P^3 grid points are assigned to all the boxes from level L to level T. In the literature, the P^3 grid points are always located in/on the box as shown in Fig. 4.3(a) [42],[43],[88]. This leads to a significant loss of accuracy when basis/testing functions are at the boundaries of the boxes because it involves extrapolation operations. For example, both basis functions in Fig. 4.3(a) are anter/interpolated using the same 4^3 grids; but close to half of the top-left basis function resides outside the box (even though its center of support is inside it). To maintain accuracy, an alternative scheme is proposed [89], where the grid points extend beyond the boxes and not all of the P^3 points are used for anter/interpolation, i.e., a sub-domain/sub-box anter/interpolation that uses only M^3 grid points is proposed ($M \leq P$). For example, in Fig. 4.3(b), one more grid point is added in all directions ($P = 6$) and the basis functions are still anter/interpolated onto 4^3 grids ($M = 4$): The top-left and bottom-right basis functions are anter/interpolated using the grid points inside the red and blue dotted squares, respectively. This approach yields a pure anter/interpolation scheme that improves the accuracy by avoiding extrapolation errors but it increases the cost of interaction between boxes as P is larger.

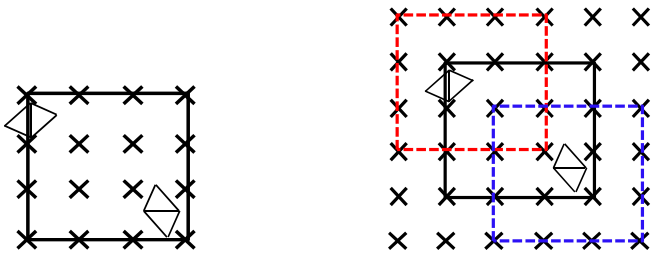

(a) (b)

Figure 4.3: Anter/interpolation schemes for traversing the oct-tree. (a) Typical inaccurate and cheap scheme that involves points in/on the box (b) Proposed more accurate and expensive scheme that involves points that extend beyond the box.

At each MOM iteration, the proposed FFT-MLIM algorithm executes a four-step procedure: Upward pass, FFT truncation, downward pass, and NIL computation. In the following, $\mathbf{I}_{l,b_l}^{\{x,y,z,\nabla\}}$ / $\mathbf{V}_{l,b_l}^{\{x,y,z,\nabla\}}$ are $P^3 \times 1$ vectors that represent the corresponding components of the current/potential on the grid of box b_l at level $l = T,\ldots,L$.

Upward pass: This is implemented in three stages. (i) The currents on the primary mesh are anterpolated onto the grids of corresponding boxes at level L. i.e.,

$$\mathbf{I}_{L,b_L}^{\{x,y,z,\nabla\}} = \sum_{n \in CB(b_L)} \mathbf{\Lambda}_{L,n}^{\{x,y,z,\nabla\}} \mathbf{I}[n] \tag{4.1.1}$$

where $\mathbf{\Lambda}_{L,n}^{\{x,y,z,\nabla\}} = [\mathbf{\Lambda}_{L,n}^{\{x,y,z,\nabla\},S} \; j\omega\mathbf{\Lambda}_{L,n}^{\{x,y,z,\nabla\},V}]$ is a $P^3 \times 2$ matrix. $\mathbf{\Lambda}_{L,n}^{\{x,y,z,\nabla\},S}$ store the $P^3 \times 1$ anterpolation coefficient for $\hat{\mathbf{x}} \cdot \mathbf{b}_n^S$, $\hat{\mathbf{y}} \cdot \mathbf{b}_n^S$, $\hat{\mathbf{z}} \cdot \mathbf{b}_n^S$, $\nabla \cdot \mathbf{b}_n^S$ as in Section 3.4, and $\mathbf{\Lambda}_{L,n}^{\{x,y,z,\nabla\},V}$ store those for $\hat{\mathbf{x}} \cdot \chi_n \mathbf{b}_n^V$, $\hat{\mathbf{y}} \cdot \chi_n \mathbf{b}_n^V$, $\hat{\mathbf{z}} \cdot \chi_n \mathbf{b}_n^V$, and $\nabla \cdot (\chi_n \mathbf{b}_n^V)$ as in Section 3.4, respectively. (ii) For all the non-empty boxes at level $l = L-1, L-2, \ldots, T$, the currents on their children boxes at level $l+1$ are anterpolated onto their grids, i.e.,

$$\mathbf{I}_{l,b_l}^{\{\mathrm{x,y,z},\nabla\}} = \sum_{b_{l+1}\in CB(b_l)} \mathbf{\Lambda}_{l+1,b_{l+1}} \mathbf{I}_{l+1,b_{l+1}}^{\{\mathrm{x,y,z},\nabla\}} \tag{4.1.2}$$

for $b_l = 1,\ldots,NB_l$ and $l = L-1, L-2,\ldots,T$, where $\mathbf{\Lambda}_{l+1,b_{l+1}}$ is a $P^3 \times P^3$ matrix, each column of which stores M^3 anterpolation coefficients. The anterpolation coefficients for different current components between the parent and children boxes are the same. (iii) For each box b_l' at level $l = L-1, L-2,\ldots,T+1$, the fields are propagated to all the non-empty boxes in the FIL of that box using FFTs [43], i.e.,

$$\mathbf{V}_{l,b_l}^{\{\mathrm{x,y,z},\nabla\}} = \mathbf{G}_{l,b_l,b_l'}^{\{\mathrm{x,y,z},\nabla\}} \mathbf{I}_{l,b_l'}^{\{\mathrm{x,y,z},\nabla\}}, \qquad \forall b_l \in FIL(b_l') \tag{4.1.3}$$

Here, $\mathbf{G}_{l,b_l,b_l'}^{\{\mathrm{x,y,z},\nabla\}}$ are the corresponding Green function propagators between box b_l' and box b_l and $\mathbf{V}_{l,b_l}^{\{\mathrm{x,y,z},\nabla\}}$ are $P^3 \times 1$ arrays. This multiplication is computed using FFTs.

FFT truncation: To implement the FFT truncation at level T, a global grid with $N^{3\mathrm{D}} = N^{3\mathrm{D,x}} N^{3\mathrm{D,y}} N^{3\mathrm{D,z}}$ grids is introduced; this grid is the union of the grids of all boxes at level T. A four-stage procedure similar to AIM/pFFT is followed: First, the currents $\mathbf{I}_g^{\{\mathrm{x,y,z},\nabla\}}$ on the global grids are obtained by combining the currents on the (overlapping) grids of all non-empty boxes at level T as

$$\mathbf{I}_g^{\{\mathrm{x,y,z},\nabla\}} = \sum_{b_T=1}^{NB_T} \mathbf{S}_{T,b_T} \mathbf{I}_{T,b_T}^{\{\mathrm{x,y,z},\nabla\}} \tag{4.1.4}$$

where each $\mathbf{S}_{T,b_T}$ is an $N^{3\mathrm{D}} \times P^3$ selection (sub)matrix that has one non-zero entry per column equal to one. Second, the fields of these combined currents are propagated onto the same global grid using FFTs. Similar to (4.1.3), this step can expressed as

$$\mathbf{V}_g^{\{\mathrm{x,y,z},\nabla\}} = \mathbf{G}_g^{\{\mathrm{x,y,z},\nabla\}} \mathbf{I}_g^{\{\mathrm{x,y,z},\nabla\}} \tag{4.1.5}$$

where $\mathbf{G}_g^{\{x,y,z,\nabla\}}$, $\mathbf{I}_g^{\{x,y,z,\nabla\}}$, and $\mathbf{V}_g^{\{x,y,z,\nabla\}}$ are Green function, current, and field arrays of size N^{3D}. Third, the fields are assigned (copied) to the grids of non-empty boxes at level T from the global grid, i.e.,

$$\mathbf{V}_{T,b_T}^{\{x,y,z,\nabla\}} = \mathbf{S}_{T,b_T}^{\dagger} \mathbf{V}_g^{\{x,y,z,\nabla\}} \tag{4.1.6}$$

The contributions from near-zones to these fields should be corrected similar to AIM; however, this is achieved by a "post-correction" and not a pre-correction operation. Fourth, for each box at level T, (inaccurate) fields are propagated to all the non-empty boxes in its NIL using FFTs, which are subtracted from the assigned fields as

$$\mathbf{V}_{T,b_T}^{\{x,y,z,\nabla\}} = \mathbf{V}_{T,b_T}^{\{x,y,z,\nabla\}} - \mathbf{G}_{T,b_T,b'_T}^{\{x,y,z,\nabla\}} \mathbf{I}_{T,b'_T}^{\{x,y,z,\nabla\}}, \qquad \forall b_T \in NIL(b'_T) \tag{4.1.7}$$

These four-stages can be described as "combine, propagate, assign, and post-correct".

Downward pass: In this step, the oct-tree is traversed from level T to $L+1$. (i) For each non-empty box b_l at level l ($l = T+1,\ldots,L$), the fields on its grid points are found by interpolating those on their parent boxes grid points and adding them to those propagated from the boxes in their FIL (found during the upward pass) :

$$\mathbf{V}_{l,b_l}^{\{x,y,z,\nabla\}} = \mathbf{V}_{l,b_l}^{\{x,y,z,\nabla\}} + \boldsymbol{\Lambda}_{l,b_l}^{\dagger} \mathbf{V}_{l-1,b_{l-1}}^{\{x,y,z,\nabla\}} \tag{4.1.8}$$

Similarly, the fields on the primary mesh are interpolated from those on the grids of boxes at level L.

$$\mathbf{V}^{\text{far}}[m] = \sum_{\nu \in \{x,y,z,\nabla\}} \boldsymbol{\Lambda}_{l,b_l}^{\nu\ \dagger} \mathbf{V}_{L,b_L}^{\nu}, \qquad \forall m \in CB(b_L) \tag{4.1.9}$$

NIL Computation: For each non-empty box at level L, the currents on the (basis) functions assigned to it are propagated directly onto the (testing) functions assigned to the boxes in its NIL. For each non-empty source box b'_L, this can be formulated as

$$\mathbf{V}^{\text{near}}[m] = \sum_{n \in CB(b_L')} \mathbf{Z}[m,n]\mathbf{I}[n], \qquad \forall m \in CB(b_L) \text{ and } b_L \in NIL(b_L') \tag{4.1.10}$$

From above 4 steps, the impedance matrix-vector product at each iteration can be approximated as $\mathbf{V} = \mathbf{ZI} \approx \mathbf{V}^{\text{near}} + \mathbf{V}^{\text{far}}$, where $\mathbf{V}^{\text{near}}$ is above and $\mathbf{V}^{\text{far}}$ can be expressed recursively as

$$\begin{aligned}
\mathbf{V}^{\text{far}} &= \sum_{v \in \{\text{x,y,z,}\nabla\}} \boldsymbol{\Lambda}_L^{v\dagger}(\mathbf{Z}_{L-1}^{v} + \mathbf{G}_L^{v})\boldsymbol{\Lambda}_L^{v}\mathbf{I} \\
\mathbf{Z}_{L-1}^{\{\text{x,y,z,}\nabla\}} &= \boldsymbol{\Lambda}_{L-1}^{\{\text{x,y,z,}\nabla\}\dagger}(\mathbf{Z}_{L-2}^{\{\text{x,y,z,}\nabla\}} + \mathbf{G}_{L-1}^{\{\text{x,y,z,}\nabla\}})\boldsymbol{\Lambda}_{L-1}^{\{\text{x,y,z,}\nabla\}} \\
&\vdots \\
\mathbf{Z}_{l-1}^{\{\text{x,y,z,}\nabla\}} &= \boldsymbol{\Lambda}_{l-1}^{\{\text{x,y,z,}\nabla\}\dagger}(\mathbf{Z}_{l-2}^{\{\text{x,y,z,}\nabla\}} + \mathbf{G}_{l-1}^{\{\text{x,y,z,}\nabla\}})\boldsymbol{\Lambda}_{l-1}^{\{\text{x,y,z,}\nabla\}} \\
&\vdots \\
\mathbf{Z}_{T+1}^{\{\text{x,y,z,}\nabla\}} &= \boldsymbol{\Lambda}_{T+1}^{\{\text{x,y,z,}\nabla\}\dagger}(\mathbf{Z}_{T}^{\{\text{x,y,z,}\nabla\}} + \mathbf{G}_{T+1}^{\{\text{x,y,z,}\nabla\}})\boldsymbol{\Lambda}_{T+1}^{\{\text{x,y,z,}\nabla\}} \\
\mathbf{Z}_{T}^{\{\text{x,y,z,}\nabla\}} &= \boldsymbol{\Lambda}_{T}^{\{\text{x,y,z,}\nabla\}\dagger}(\mathbf{S}_T^{\dagger}\mathbf{G}_g^{\{\text{x,y,z,}\nabla\}}\mathbf{S}_T - \mathbf{G}_T^{\{\text{x,y,z,}\nabla\}})\boldsymbol{\Lambda}_L^{\{\text{x,y,z,}\nabla\}}
\end{aligned} \tag{4.1.11}$$

4.1.2 Computational Complexity

The matrix fill time, memory cost, and matrix solve time of the FFT-MLIM algorithm are detailed next. Upward pass: Anterpolation from basis functions onto the grids of boxes at level L require $O(NM^3)$ operations at each iteration and $O(NM^3)$ memory. At each level l ($l = T+1,\ldots,L$), the anterpolation and propagation between boxes in FIL require $O(NB_lP^6)$ and $O(NF_lNB_lP^3\log P^3)$ operations per iteration, respectively, where NF_l is the average number of box in FIL of each box. Storing the current and field in all the boxes requires $O(NB_lP^3)$ storage. (ii) FFT Truncation: At level T, the combine and assigns stages require negligible number of operations. The propagation and correction require $O(N^{3\text{D}}\log N^{3\text{D}})$ and $O(NN_TNB_TP^3\log P^3)$ operations per iteration, respectively, where NN_T is the average number of box in NIL of each box. The memory cost is $O(N^{3\text{D}} + NB_TP^3)$. (iii) Downward pass: The

interpolation costs are identical to the anterpolation costs, i.e., they require a total of $O(NM^3)$ operations per iteration and $O(NM^3)$ memory. (iv) NIL computation: This requires $O(N^{\text{near}})$ operations per iteration and $O(N^{\text{near}})$ memory, where N^{near} is the total number of basis pairs in NIL.

In total, the anter/interpolation matrices, current/field matrices, the NIL computation matrix, and the propagation matrices (dominated by the global grid at level T) have $O(N)$, $O(N)$, $O(N^{\text{near}})$, and $O(N^{\text{3D}})$ unique entries, respectively. Multiplying these matrices with the necessary vector requires $O(N)$, $O(N)$, $O(N^{\text{near}})$, and $O(N^{\text{3D}} \log N^{\text{3D}})$ operations at each iteration, respectively. Thus, the matrix fill time, memory cost, and matrix solve time per iteration of the proposed FFT-MLIM scale as $O(N^{\text{near}} + N^{\text{3D}})$, $O(N^{\text{near}} + N^{\text{3D}})$, and $O(N^{\text{near}} + N^{\text{3D}} \log N^{\text{3D}})$. Because of the multilevel oct-tree structure, unlike the AIM algorithms in Chapters II, III, and V, this algorithm guarantees that $N^{\text{near}} \sim N$ even for multi-scale structures.

4.2 NUMERICAL RESULTS

This section presents numerical results to compare the computational costs of AIM and FFT-MLIM in the high-, low-, and mixed-frequency regimes and validate the accuracy of the proposed method. In all simulations, the preconditioner, and the iterative solver tolerance are the same as those described in Section 2.3. All the FFT-MLIM results in this section are obtained using a serial implementation of the method while the AIM results are obtained using an MPI-based parallel implementation of the method. The reported timing and memory data for AIM were "serialized" as described in Section 2.3.

4.2.1 Computational Complexity

To compare the methods in the high-frequency regime, scattering from a PEC plate is analyzed as its size is increased from $\lambda_0 \times \lambda_0$ to $64\lambda_0 \times 64\lambda_0$ while keeping the surface mesh density constant (average edge length of the mesh is $\lambda_0 / 10$), where λ_0 is the wavelength in free space. To compare them in the low-frequency regime, scattering from a $\lambda_0 \times \lambda_0$ PEC plate is analyzed as the average edge length of the mesh is decreased from $\lambda_0 / 10$ to $\lambda_0 / 640$ while keeping the plate size constant. To compare them in the mixed-frequency regime, scattering from a 2×2 square array of $\lambda_0 \times \lambda_0$ PEC plates is analyzed as the average edge length of the mesh is decreased from $\lambda_0 / 10$ to $\lambda_0 / 320$ while keeping the array spacing ($10\lambda_0$ in each direction) and plate sizes constant. Note that the high- and low-frequency simulations examine the performance of the methods for single-scale structures. The mixed-frequency simulations shows their performance for multi-scale structures as the plate array has large distance between cells (much larger than λ_0) and has detailed mesh in the unit cell (much smaller than λ_0). All the plates are on the *xoy* plane and are illuminated by an $\hat{x}$-polarized plane wave propagating toward the $-\hat{z}$ direction. The accuracy of the simulations are quantified by computing $err^{\theta\theta}$, the relative root-mean-square error in the VV-polarized bistatic radar cross section. For reference, the MOM solution of the same problem is used; when this is not feasible, a more accurate AIM solution is used. The AIM and FFT-MLIM parameters are chosen to minimize the computational costs subject to the constraint that $err^{\theta\theta} < 1\%$.

The computational requirements of FFT-MLIM, AIM, and MOM are contrasted in Figs. 4.4-4.6 for the different simulation regimes. Overall, the observed data and the curves that are fitted to them in Fig. 4.4-4.6 agree well with the asymptotical trends described in

Section 4.1.2. The high- and low-frequency simulations are employed to examine the performance of FFT-MLIM for single-scale structures. The mixed-frequency example shows its performance for multi-scale structure as the plate array has the distance between cells (much larger than λ_0) and meanwhile the unit cell has detailed mesh (much less than λ_0). From Fig. 4.4, the cost of FFT-MLIM is slightly higher than that of pFFT/AIM in high-frequency regime. In low-frequency regime, the matrix fill time and memory scale as $O(N)$ for both FFT-MLIM and pFFT/AIM, but FFT-MLIM has a larger constant in front of N. In Fig. 4.5(c), the matrix solve time of FFT-MLIM and pFFT/AIM scales as $O(N)$ and $O(N \log N)$ ($N^{3D} \sim N$), but FFT-MLIM only outperforms pFFT/AIM beyond $N = 10^6$. Therefore, pFFT/AIM is a better choice for single-scale structures. In Fig. 4.6, the pFFT/AIM becomes less efficient due to the large empty space between cells while FFT-MLIM is not affected, and it outperforms pFFT/AIM after $N = 10^4$. And the matrix solve time per iteration of FFT-MLIM is dominant by $O(N)$ as the number of unknown is increased by making the mesh density denser. If the number of unknown is increased by enlarging the structures, it will scale as $O(N)$. Thus, FFT-MLIM is a better alternative for analyzing multi-scale problems.

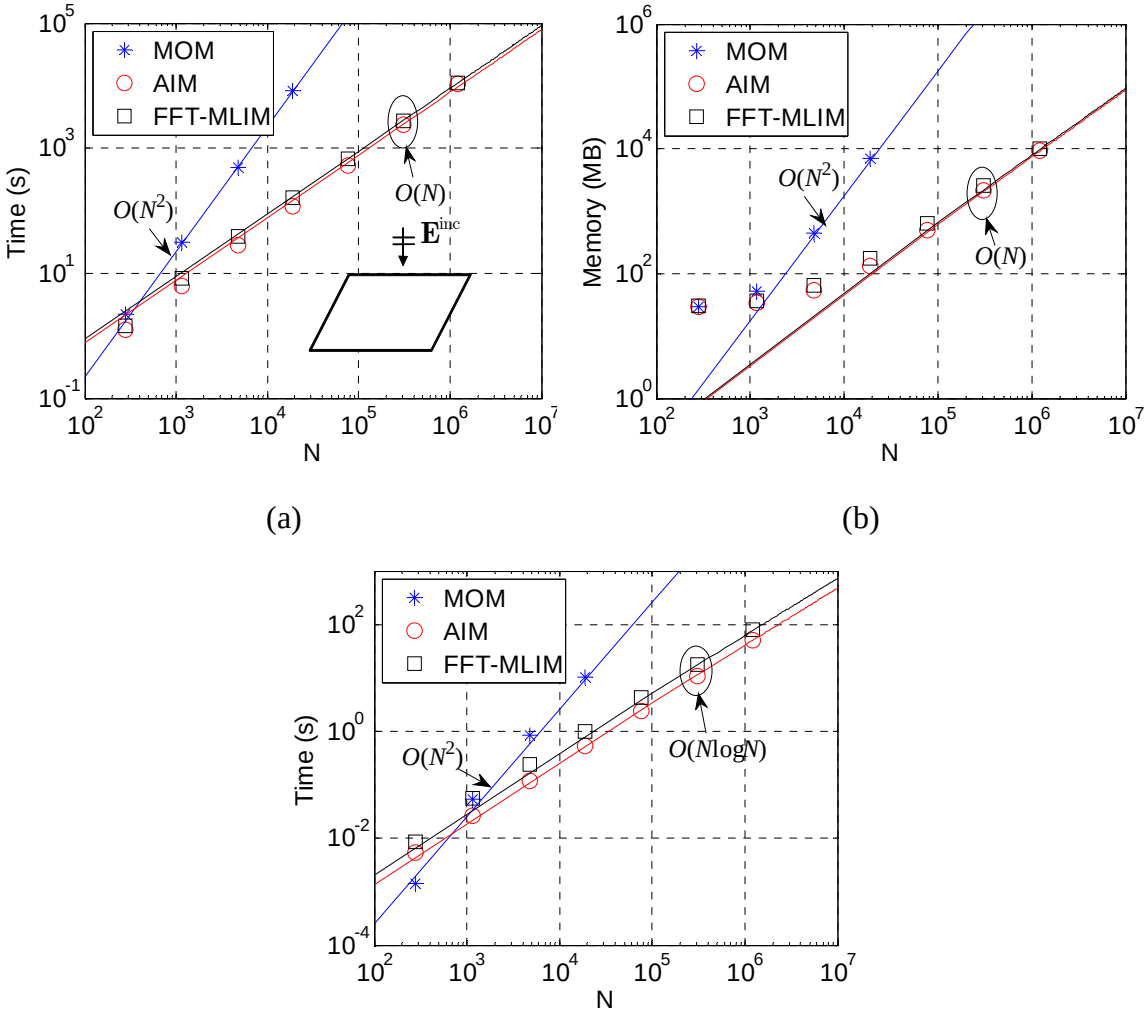

Figure 4.4: Computational costs for plates in high-frequency regime as the size is increased and mesh density is fixed. (a) Matrix fill time. (b) Memory requirement. (c) Time per iteration.

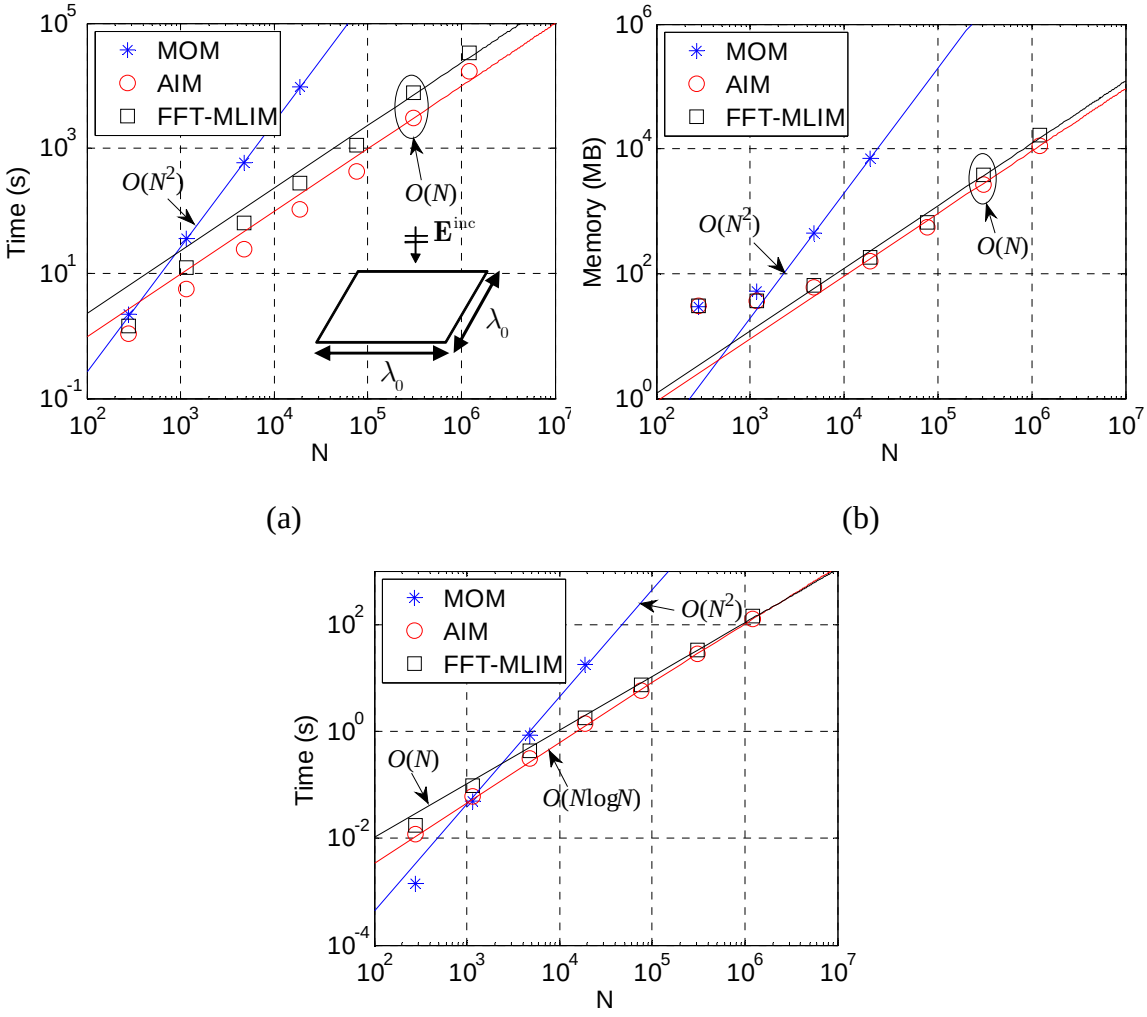

Figure 4.5: Computational costs for plates in low-frequency regime as the mesh is refined and the size is fixed. (a) Matrix fill time. (b) Memory requirement. (c) Time per iteration.

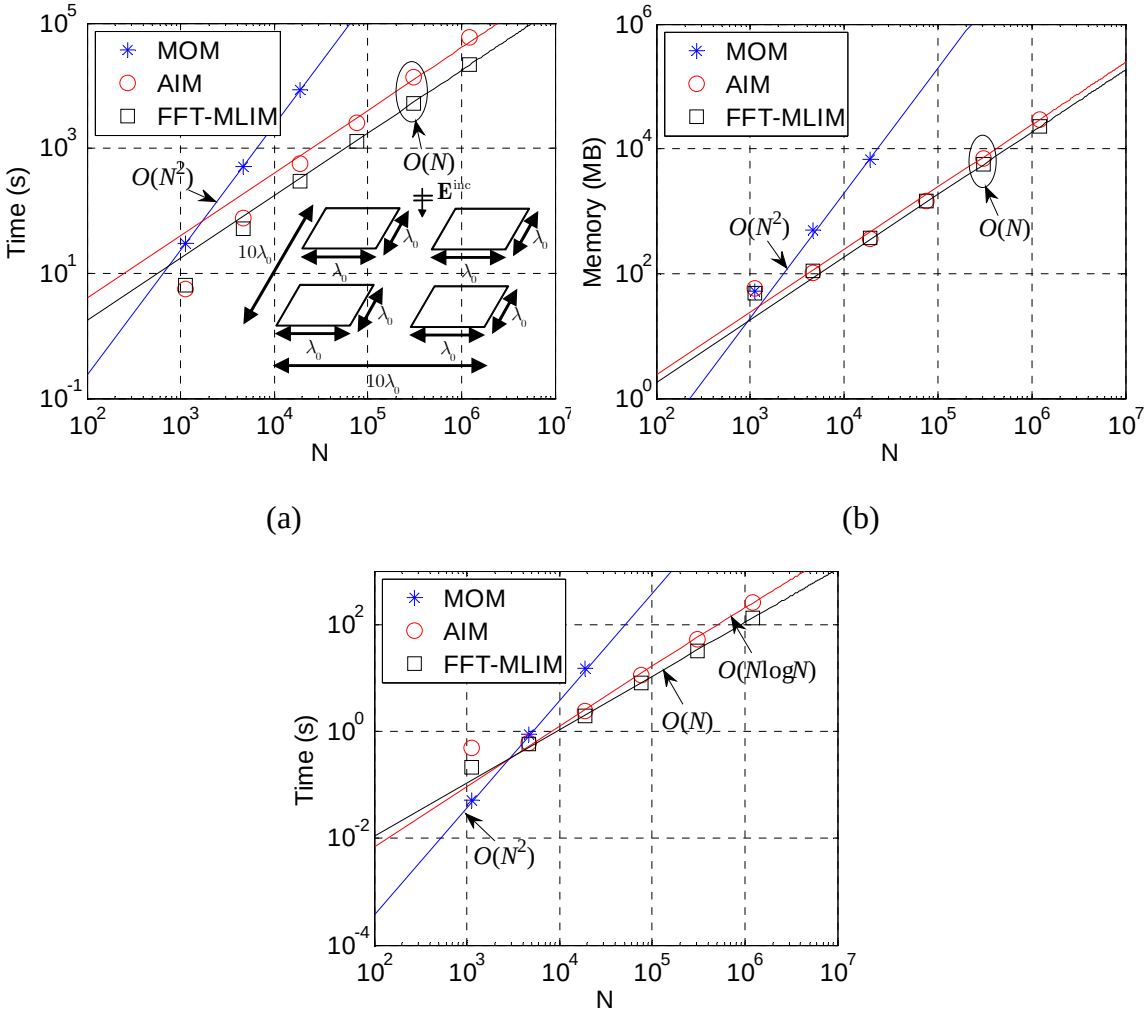

Figure 4.6: Computational costs for the plate array in mixed-frequency regime as the array size is fixed and mesh is refined. (a) Matrix fill time. (b) Memory requirement. (c) Time per iteration.

4.2.2 Validation

Next, the accuracy of the proposed scheme for solving inhomogeneous penetrable problems is demonstrated by analyzing scattering from a 3-D five-period dielectric slab (type 1a problem) [90]. The five-period dielectric slab is shown in Fig. 4.7(a), where $h = 9.0 / k_0$ (k_0 is the wave number in free space), $d = h / 1.713$, $L = 6d$, $d_1 = d_2 = 0.5d$, $\varepsilon_1 = 1.44\varepsilon_0$, and $\varepsilon_2 = 2.56\varepsilon_0$, The dielectric slab is excited by a plane wave incident from $\theta^{\text{inc}} = 45^\circ$ and $\phi^{\text{inc}} = 0^\circ$. The volume of the dielectric slab is discretized using tetrahedrons with $\sim \lambda_0 / 8.1$ average edge length; this yields, $N = 324\ 290$. A 5-level oct tree is constructed and truncated in level 4. The RCS patterns calculated with FFT-MLIM are compared to those calculated by a reference pFFT [90] in Fig. 4.7(b); the results are essentially identical. This simulation required $\sim 1.7 \times 10^4$ seconds for filling the matrices, 4.7 GB memory, 9.3×10^2 seconds per iteration, and $N^{\text{it}} = 140$ iterations.

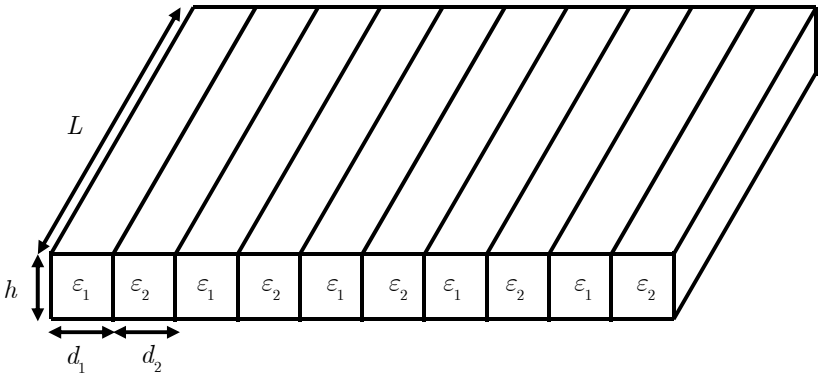

(a)

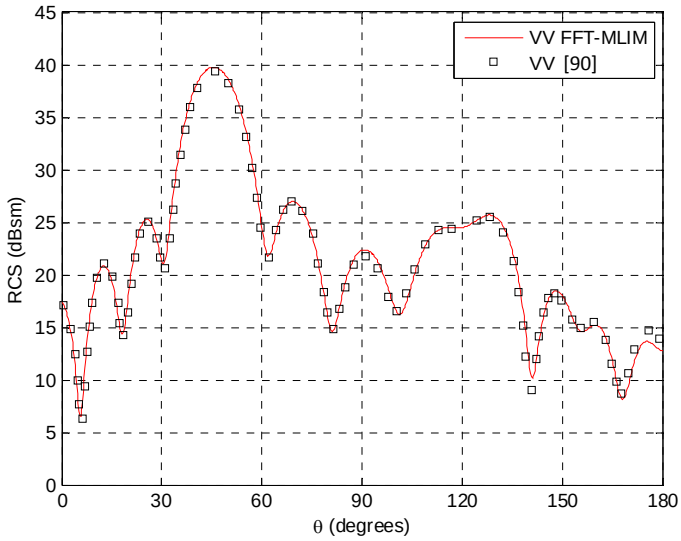

(b)

Figure 4.7: Scattering problem involving a five-period dielectric slab in free space. (a) Geometry. (b) Copolarized bistatic RCS patterns in the $\phi = 0^\circ$ cut.

4.3 SUMMARY

This Chapter presented a FFT-truncated multilevel interpolation method for the analysis of multi-scale structures in homogeneous backgrounds. Numerical results for single- and multi-scale PEC structures show that FFT-MLIM performance is comparable to but slightly worse than that of AIM for single-scale structures but outperforms the latter for multi-scale structures. While the presentation is constrained to homogeneous backgrounds in this Chapter, FFT-MLIM can be extended to type 2 multi-scale problems in rectangular cavities as is done for AIM in Chapter III or type 4 multi-scale problems in layered backgrounds as is done for AIM in Chapter V.

Chapter V: Adaptive Integral Method for Layered Media

This Chapter presents an extended AIM scheme that is efficient for solving single-scale structures in multi-scale backgrounds (type 3a and 3b multi-scale problems). Section 5.1 details the AIM extension for the structures embedded in a single layer of a uniaxial planar-layered medium and validates the mehtod. Section 5.2 further extends the scheme for structures embedded in multiple layers of a planar-layered medium and verifies the method's accuracy and efficiency. The methods are formulated for surface integral equations for brevity but are also applicable to volume integral equations as demonstrated by numerical results in Sections 5.1.5.2 and 6.1.2.

5.1 Single Layer Extension of AIM for Layered Media

This section formulates the surface combined-field integral equation, its classical MOM solution, and the proposed AIM acceleration for structures embedded in a single layer of a uniaxial planar-layered medium.

5.1.1 Surface Combined-Field Integral Equation

Consider an arbitrarily shaped 3-D PEC surface S embedded in layer κ of a uniaxial medium that is stratified into K planar layers in the $\hat{\mathbf{z}}$ direction. A time-harmonic electromagnetic field $\{\mathbf{E}^{\text{inc}}, \mathbf{H}^{\text{inc}}\}$ is incident on the structure. The upper boundary, complex permittivity tensor, and permeability of each layer $k = 1, \ldots, K$ is denoted with z_k, $\underline{\underline{\tilde{\boldsymbol{\varepsilon}}}}_k$, and μ_k, respectively (Fig. 5.1(a)). The complex permittivity tensors is given as

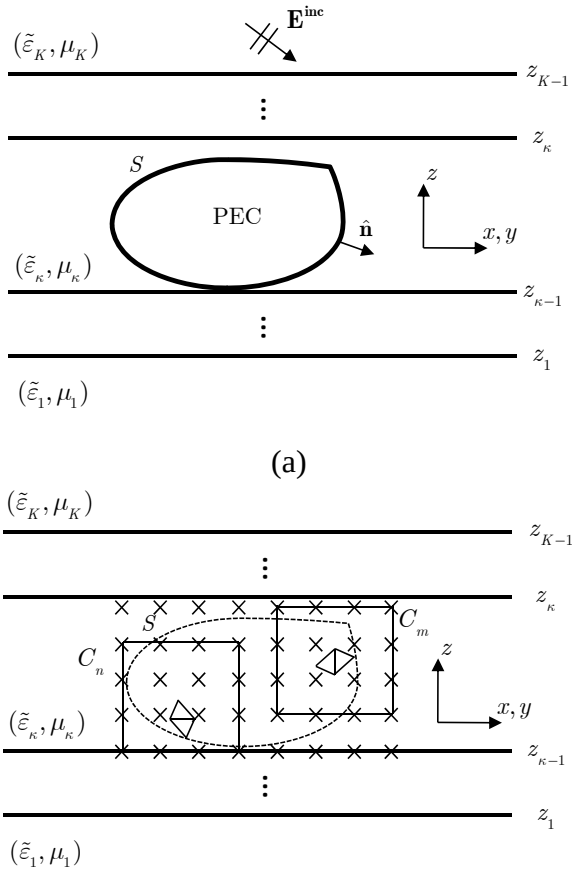

Figure 5.1: Scattering problem involving an arbitrarily shaped 3-D structure residing in one layer of a planar-layered medium. (a) Geometry and excitation definition. (b) The auxiliary grid points and the set of points assigned to two of the RWG basis functions.

$$\underline{\underline{\tilde{\boldsymbol{\varepsilon}}}}_k(\mathbf{r}) = \tilde{\varepsilon}_k^{\mathrm{t}} \begin{bmatrix} 1 & 0 & 0 \\ 0 & 1 & 0 \\ 0 & 0 & \beta_k \end{bmatrix} \varepsilon_0 \tag{5.1.1}$$

Here, $\tilde{\varepsilon}_k^{\mathrm{t}} = \varepsilon_k^{\mathrm{t}} + \sigma_k^{\mathrm{t}} / j\omega$ and β_k denote the horizontal component and the ratio of the vertical to horizontal component of the complex relative permittivity of layer k, respectively. The scattered fields $\{\mathbf{E}^{\mathrm{sca}}, \mathbf{H}^{\mathrm{sca}}\}$ are expressed in mixed potential form as [13]:

$$\begin{aligned}\mathbf{E}^{\mathrm{sca}}(\mathbf{r}) &= -j\omega\mathbf{A}(\mathbf{r}) - \nabla\phi(\mathbf{r}) = -j\omega\mu_0 \iint_S [\underline{\underline{\mathbf{g}}}(\mathbf{r},\mathbf{r}') + \underline{\underline{\mathbf{p}}}(\mathbf{r},\mathbf{r}')] \cdot \mathbf{J}(\mathbf{r}')ds' \\ &\quad + \frac{\nabla}{j\omega\varepsilon_0} \iint_S g^{\phi}(\mathbf{r},\mathbf{r}')\nabla' \cdot \mathbf{J}(\mathbf{r}')ds' \\ \mathbf{H}^{\mathrm{sca}}(\mathbf{r}) &= \frac{1}{\mu_0}\nabla \times \mathbf{A}(\mathbf{r}) = \nabla \times \iint_S \underline{\underline{\mathbf{g}}}(\mathbf{r},\mathbf{r}') \cdot \mathbf{J}(\mathbf{r}')ds'\end{aligned} \tag{5.1.2}$$

where $\mathbf{A}$ and ϕ denote the magnetic vector and electric scalar potentials due to the surface current density $\mathbf{J}$, $\underline{\underline{\mathbf{g}}} = \hat{\mathbf{x}}\hat{\mathbf{x}}g^{\mathrm{xx}} + \hat{\mathbf{y}}\hat{\mathbf{y}}g^{\mathrm{yy}} + \hat{\mathbf{z}}\hat{\mathbf{x}}g^{\mathrm{zx}} + \hat{\mathbf{z}}\hat{\mathbf{y}}g^{\mathrm{zy}} + \hat{\mathbf{z}}\hat{\mathbf{z}}g^{\mathrm{zz}}$ and g^{ϕ} are dyadic and scalar Green functions, and $\mathbf{r} = \rho\hat{\rho} + z\hat{\mathbf{z}}$ and $\mathbf{r}' = \rho'\hat{\rho} + z'\hat{\mathbf{z}}$ denote observer and source points, respectively. Because the scalar potentials of point charges associated with horizontal and vertical dipoles are generally different in layered media, the mixed potential formulation requires the dyadic correction factor $\underline{\underline{\mathbf{p}}} = \hat{\mathbf{x}}\hat{\mathbf{z}}p^{\mathrm{xz}} + \hat{\mathbf{y}}\hat{\mathbf{z}}g^{\mathrm{yz}} + \hat{\mathbf{z}}\hat{\mathbf{z}}p^{\mathrm{zz}}$. All Green function and correction factor components can be calculated using Sommerfeld integrals and transmission line theory [91], e.g.,

$$g^{\mathrm{xx}}(\mathbf{r},\mathbf{r}') = g^{\mathrm{xx}}(|\,\boldsymbol{\rho} - \boldsymbol{\rho}'\,|, z, z') = \frac{1}{2\pi}\int_0^{\infty} \tilde{g}^{\mathrm{xx}}(k_\rho, z, z')J_0(k_\rho\,|\,\boldsymbol{\rho} - \boldsymbol{\rho}'\,|)k_\rho dk_\rho \tag{5.1.3}$$

where $\tilde{g}^{\mathrm{xx}}$ is a spectral domain Green function, J_0 is the zeroth order Bessel function of the first kind, and k_ρ is the Fourier transform variable.

The surface combined-field integral equation (SCFIE) is obtained by enforcing the tangential boundary conditions on S and linearly combining the resulting equations as

$$-\alpha\hat{\mathbf{n}}(\mathbf{r}) \times \hat{\mathbf{n}}(\mathbf{r}) \times \mathbf{E}(\mathbf{r}) + (1-\alpha)\eta_\kappa \hat{\mathbf{n}}(\mathbf{r}) \times \mathbf{H}(\mathbf{r}) = (1-\alpha)\eta_\kappa \mathbf{J}(\mathbf{r}) \tag{5.1.4}$$

Here, $\hat{\mathbf{n}}$ is the outward directed unit vector normal to S, η_κ is the intrinsic impedance of κ^{th} layer, and $0 \le \alpha \le 1$.

5.1.2 MOM

To find $\mathbf{J}$, the electromagnetic fields in (5.1.4) are expressed as a sum of incident and scattered fields, (5.1.2) is substituted in, and the SCFIE is converted to a system of linear equations using the standard MOM procedure: The surface is discretized into triangular patches; the current density is expanded using N basis functions $\mathbf{b}_1^{\text{S}},\ldots,\mathbf{b}_N^{\text{S}}$:

$$\mathbf{J}(\mathbf{r}) \cong \sum_{n=1}^{N} \mathbf{I}[n]\mathbf{b}_n^{\text{S}}(\mathbf{r}) \tag{5.1.5}$$

where $\mathbf{I}$ are the coefficients to be found and the basis functions are chosen to be RWG [22] functions. (5.1.4) is tested with N linearly independent functions $\mathbf{t}_1^{\text{S}},\ldots,\mathbf{t}_N^{\text{S}}$; here, the Galerkin testing is employed, i.e., $\mathbf{t}_m^{\text{S}} = \mathbf{b}_m^{\text{S}}$ for $m = 1,\ldots,N$. This MOM procedure yields the matrix equation

$$\mathbf{ZI} = \mathbf{V}^{\text{inc}} \tag{5.1.6}$$

Here, the entries of impedance matrix $\mathbf{Z}$ and the tested incident field vector $\mathbf{V}^{\text{inc}}$ are given by

$$\begin{aligned}
\mathbf{Z}[m,n] &= j\omega\mu_0\alpha \iint_S \mathbf{t}_m^{\text{S}}(\mathbf{r}) \cdot \iint_S [\underline{\underline{\mathbf{g}}}(\mathbf{r},\mathbf{r}') + \underline{\underline{\mathbf{p}}}(\mathbf{r},\mathbf{r}')] \cdot \mathbf{b}_n^{\text{S}}(\mathbf{r}')ds'ds \\
&\quad + \frac{\alpha}{j\omega\varepsilon_0} \iint_S \nabla\cdot\mathbf{t}_m^{\text{S}}(\mathbf{r}) \iint_S g^{\phi}(\mathbf{r},\mathbf{r}')\nabla'\cdot\mathbf{b}_n^{\text{S}}(\mathbf{r}')ds'ds \\
&\quad + (1-\alpha)\eta_\kappa \iint_S \hat{\mathbf{n}}(\mathbf{r}) \times \mathbf{t}_m^{\text{S}}(\mathbf{r}) \cdot \nabla \times \iint_S \underline{\underline{\mathbf{g}}}(\mathbf{r},\mathbf{r}') \cdot \mathbf{b}_n^{\text{S}}(\mathbf{r}')ds'ds \\
\mathbf{V}^{\text{inc}}[m] &= \iint_S \alpha\mathbf{t}_m^{\text{S}}(\mathbf{r}) \cdot \mathbf{E}^{\text{inc}}(\mathbf{r}) + (1-\alpha)\eta_\kappa \mathbf{t}_m^{\text{S}}(\mathbf{r}) \cdot \hat{\mathbf{n}}(\mathbf{r}) \times \mathbf{H}^{\text{inc}}(\mathbf{r})ds
\end{aligned} \tag{5.1.7}$$

for $1 \le m,n \le N$. The calculation of the impedance matrix (matrix fill time), the memory required for storing it (memory cost), and the solution of (5.1.6) (matrix solve time) are the main computational costs of the above MOM procedure. The matrix fill time and memory cost scale as $O(N^2)$ and the matrix solve time scales as $O(N^{\mathrm{it}}N^2)$ if an iterative solver that converges in N^{it} iterations is used.

The matrix fill time for structures in layered media is significantly larger than for those in free space because of the time-consuming Sommerfeld integrals needed for the $O(N^2)$ Green function evaluations in (5.1.7). Various methods exist for reducing this setup cost [52],[92]-[94]; here, the following are adopted: (i) Interpolation [52]: The number of Sommerfeld integrals can be reduced significantly by interpolating the Green function and correction factor components from tables that store their samples. Specifically, each component in (5.1.7), i.e., $g^{\mathrm{xx,yy,zx,zy,zz}}$ and $p^{\mathrm{xz,yz,zz}}$, is decomposed into functions of $z-z'$ and $z+z'$, e.g.,

$$g^{\mathrm{xx}}(|\boldsymbol{\rho}-\boldsymbol{\rho}'|,z,z') = g^{\mathrm{xx}}_{\mathrm{TTT}}(|\boldsymbol{\rho}-\boldsymbol{\rho}'|,z-z') + g^{\mathrm{xx}}_{\mathrm{TTH}}(|\boldsymbol{\rho}-\boldsymbol{\rho}'|,z+z') \quad (5.1.8)$$

The samples of the convolution and correlation terms are stored in two two dimensional (2-D) tables; thus, each table stores $N_\rho N_h$ samples found by uniformly sampling the interval $0 \le |\boldsymbol{\rho}-\boldsymbol{\rho}'| \le L_{\max}$ and either $z_{\min}-z_{\max} \le z-z' \le z_{\max}-z_{\min}$ or $2z_{\min} \le z+z' \le 2z_{\max}$, where $L_{\max}$ and $z_{\max}(z_{\min})$ denote the maximum radial distance and the largest (smallest) height on S, respectively. The components are interpolated from their samples using 2-D Lagrange interpolation; typically, ~10 samples per minimum wavelength are needed in each dimension of the table for interpolation errors on the order of 10^{-3} (see Section 5.1.5.1). This implies that for surfaces devoid of geometrical details only $N_\rho N_h \sim N$ or $\sim N^{1/2}$ Sommerfeld integrals must be

computed to fill the tables when S is a 3-D or a quasi-planar (when $L_{\max} \gg z_{\max} - z_{\min}$) surface, respectively. (ii) Singularity subtraction [92]: The computation of each Sommerfeld integral is accelerated by extracting an asymptotic term in the spectral domain found by letting $k_\rho \to \infty$; by computing the remaining integral via adaptive numerical integration; and by adding back the closed-form expression for the extracted term in the spatial domain; e.g.,

$$g^{\mathrm{xx}}(|\boldsymbol{\rho}-\boldsymbol{\rho}'|,z,z') = g^{\mathrm{xx}}_{\mathrm{ana}}(|\boldsymbol{\rho}-\boldsymbol{\rho}'|,z,z') + g^{\mathrm{xx}}_{\mathrm{TTT,num}}(|\boldsymbol{\rho}-\boldsymbol{\rho}'|,z-z') + g^{\mathrm{xx}}_{\mathrm{TTH,num}}(|\boldsymbol{\rho}-\boldsymbol{\rho}'|,z+z') \tag{5.1.9}$$

where $g^{\mathrm{xx}}_{\mathrm{ana}}$ denotes the part extracted from the Green function, which is computed using a closed-form analytical expression, and $g^{\mathrm{xx}}_{\mathrm{TTT,num}} + g^{\mathrm{xx}}_{\mathrm{TTH,num}}$ denotes the remaining part, which is computed using numerical integrals and interpolation. Here, the numerical integrals are computed using a 4-leg integration path in the first quadrant of the k_ρ plane: The first leg is along the imaginary axis; it starts at origin and has length $5\times10^{-3}k_0$, where k_0 is the wave number in free space. The second leg is parallel to the real axis in the 1st quadrant; it extends beyond where all poles and branch points can possibly appear, specifically to $1.2k_{\rho,\max}$, where $k_{\rho,\max} = \max_{1\le k\le K}(\omega\sqrt{\varepsilon_k\mu_k})$ [92], The third leg is parallel to the imaginary axis (returns to the real axis), and the last leg is along the real axis (extends to infinity). Unlike the methods in [93],[94], this subtraction approach speeds up the evaluation of Sommerfeld integrals without introducing approximation errors. Because the terms that are added back have closed-form expressions and can be computed quickly, they are not interpolated to preserve the accuracy of Green functions; i.e., interpolation is used only for the results of the numerical integration before the extracted terms are added back. In this Chapter, all the layered-medium Green functions are computed using the procedure

described in this section. Although these methods render the matrix fill time for structures in layered media comparable to that for structures in free space; to solve large-scale problems, they should be combined with fast algorithms that reduce the MOM computational complexity. FFT-based algorithms achieve this reduction by further exploiting the convolution/correlation form of Green functions as detailed next for AIM.

5.1.3 AIM

Similar to the AIM schemes in Chapters II and III, the AIM extension is also formulated by enclosing S with an auxiliary 3-D regular grid with $N^{\mathrm{3D}} = N^{\mathrm{3D,x}} N^{\mathrm{3D,y}} N^{\mathrm{3D,z}}$ nodes; importantly, all nodes of the auxiliary grid are constrained to be in layer κ to enable a Toeplitz-Hankel decomposition of the AIM matrices in the stratification direction (Fig. 5.1(b)). Similar to the classical AIM for structures in free space, the impedance matrix is approximated as $\mathbf{Z} \approx \mathbf{Z}^{\mathrm{corr}} + \mathbf{Z}^{\mathrm{FFT}}$, where $\mathbf{Z}^{\mathrm{corr}}$ is a "pre-corrected" matrix [40] and the $\mathbf{Z}^{\mathrm{FFT}}$ matrix can be expressed as

$$\begin{aligned}\mathbf{Z}^{\mathrm{FFT}} = {} & j\omega\mu_0\alpha \begin{bmatrix} \boldsymbol{\Lambda}^{\mathrm{x,S}} \\ \boldsymbol{\Lambda}^{\mathrm{y,S}} \\ \boldsymbol{\Lambda}^{\mathrm{z,S}} \end{bmatrix}^{\dagger} \begin{bmatrix} \mathbf{G}^{\mathrm{xx}} & \mathbf{0} & \mathbf{P}^{\mathrm{xz}} \\ \mathbf{0} & \mathbf{G}^{\mathrm{yy}} & \mathbf{P}^{\mathrm{yz}} \\ \mathbf{G}^{\mathrm{zx}} & \mathbf{G}^{\mathrm{zy}} & \mathbf{G}^{\mathrm{zz}} + \mathbf{P}^{\mathrm{zz}} \end{bmatrix} \begin{bmatrix} \boldsymbol{\Lambda}^{\mathrm{x,S}} \\ \boldsymbol{\Lambda}^{\mathrm{y,S}} \\ \boldsymbol{\Lambda}^{\mathrm{z,S}} \end{bmatrix} + \frac{\alpha}{j\omega\varepsilon_0} \boldsymbol{\Lambda}^{\nabla,\mathrm{S}\dagger} \mathbf{G}^{\phi} \boldsymbol{\Lambda}^{\nabla,\mathrm{S}} \\ & + (1-\alpha)\eta_{\kappa} \begin{bmatrix} \boldsymbol{\Gamma}^{\mathrm{x,S}} \\ \boldsymbol{\Gamma}^{\mathrm{y,S}} \\ \boldsymbol{\Gamma}^{\mathrm{z,S}} \end{bmatrix}^{\dagger} \begin{bmatrix} \partial_y \mathbf{G}^{\mathrm{zx}} & \partial_y \mathbf{G}^{\mathrm{zy}} - \partial_z \mathbf{G}^{\mathrm{yy}} & \partial_y \mathbf{G}^{\mathrm{zz}} \\ \partial_z \mathbf{G}^{\mathrm{xx}} - \partial_x \mathbf{G}^{\mathrm{zx}} & -\partial_x \mathbf{G}^{\mathrm{zy}} & -\partial_x \mathbf{G}^{\mathrm{zz}} \\ -\partial_y \mathbf{G}^{\mathrm{xx}} & \partial_x \mathbf{G}^{\mathrm{yy}} & \mathbf{0} \end{bmatrix} \begin{bmatrix} \boldsymbol{\Lambda}^{\mathrm{x,S}} \\ \boldsymbol{\Lambda}^{\mathrm{y,S}} \\ \boldsymbol{\Lambda}^{\mathrm{z,S}} \end{bmatrix} \end{aligned} \tag{5.1.10}$$

Here, ∂ represents derivative with respect to the variable in its subscript, the matrices $\boldsymbol{\Lambda}^{\{\mathrm{x,y,z},\nabla\},\mathrm{S}}$ represent anterpolation from basis functions on the primary mesh to point sources on the auxiliary grid, the matrices $\mathbf{G}$ and $\mathbf{P}$ represent "propagation" from sources to observers on the auxiliary grid, and the transpose matrices $\boldsymbol{\Lambda}^{\{\mathrm{x,y,z},\nabla\},\mathrm{S}\dagger}$ and

$\mathbf{\Gamma}^{\{x,y,z,\nabla\},S\dagger}$ represent interpolation from point observers on the auxiliary grid to testing functions on the primary mesh. Each column n of $\mathbf{\Lambda}^{\{x,y,z,\nabla\},S}$ and $\mathbf{\Gamma}^{\{x,y,z,\nabla\},S}$, which are sparse real matrices of size $N^{3D} \times N$, store weighting coefficients found by matching multipole moments of M_n^S points on the auxiliary grid to those of the functions $\hat{\mathbf{x}} \cdot \mathbf{b}_n^S$, $\hat{\mathbf{y}} \cdot \mathbf{b}_n^S$, $\hat{\mathbf{z}} \cdot \mathbf{b}_n^S$, $\nabla \cdot \mathbf{b}_n^S$, $\hat{\mathbf{x}} \cdot \hat{\mathbf{n}} \times \mathbf{b}_n^S$, $\hat{\mathbf{y}} \cdot \hat{\mathbf{n}} \times \mathbf{b}_n^S$, and $\hat{\mathbf{z}} \cdot \hat{\mathbf{n}} \times \mathbf{b}_n^S$, respectively [39],[95] (testing functions are the same as basis functions). In this Chapter, the M_n^S grid points are chosen to be symmetrical around the center of mass of $\mathbf{b}_n^S$ whenever possible; the set of grid points are unsymmetrical along the z direction when $\mathbf{b}_n^S$ is close to or on the layer interfaces because the auxiliary grid is confined to a single layer (Fig. 5.1(b)). The unsymmetrical choice of points does not affect the accuracy of the method significantly as demonstrated in Section 5.1.5 and in [96]. In (5.1.10), the entries of the propagation matrices, which are dense $N^{3D} \times N^{3D}$ matrices, are

$$\begin{aligned} \mathbf{G}^{xx,yy,zx,zy,zz,\phi}[u,v] &= g^{xx,yy,zx,zy,zz,\phi}(\mathbf{r}_u, \mathbf{r}_v) \\ \mathbf{P}^{xz,yz,zz}[u,v] &= g^{xz,yz,zz}(\mathbf{r}_u, \mathbf{r}_v) \end{aligned} \tag{5.1.11}$$

for nodes $u \neq v$ on the auxiliary grid; the Toeplitz part of $\mathbf{G}[u,u]$ and $\mathbf{P}[u,u]$ are set to 0 since they are singular when $\mathbf{r}_u = \mathbf{r}_v$; the Hankel part of $\mathbf{G}[u,u]$ and $\mathbf{P}[u,u]$ are set to 0 only when $\mathbf{r}_u$ is located on the layer interface. The entries of the pre-corrected matrix, which is a sparse $N \times N$ matrix, are

$$\mathbf{Z}^{corr}[m,n] = \begin{cases} \mathbf{Z}[m,n] - \mathbf{Z}^{FFT}[m,n], & \text{if } \mathrm{dist}^{SS'}[m,n] < \gamma \\ 0, & \text{else} \end{cases} \tag{5.1.12}$$

for $1 \leq m,n \leq N$. $\mathrm{dist}^{SS'}[m,n]$ also denotes the minimum "grid distance" between the functions $\mathbf{t}_m^S$ and $\mathbf{b}_n^S$ as defined in Section 2.2. $N^{corr} \sim N$ for single-scale structures [39],[48],[59] in type 3a and 3b multi-scale problems.

Unlike for structures in free space, where the AIM propagation matrices have a 3-level block-Toeplitz structure, the propagation matrices in (5.1.10) have only a 2-level block-Toeplitz structure because layered-medium Green functions are not translationally invariant in the stratification direction. To be able to use 3-D FFTs, each Green function and correction factor component is split into a term that is in convolution form in all directions and one that is in convolution form in x and y directions and correlation form in the z direction [52],[53],[59]-[62]; e.g., g^{xx} is expressed as in (5.1.8). Consequently, each propagation matrix can be split into a 3-level block-Toeplitz and a Hankel-2-level block-Toeplitz matrix; e.g., $\mathbf{G}^{\mathrm{xx}} = \mathbf{G}^{\mathrm{xx}}_{\mathrm{TTT}} + \mathbf{G}^{\mathrm{xx}}_{\mathrm{TTH}}$. Both types of matrices can be efficiently multiplied with vectors using 3-D FFTs as described in Section 3.4. For example, consider the calculation of $\mathbf{G}^{\mathrm{xx}}\boldsymbol{\Lambda}^{\mathrm{x,S}}\mathbf{I} = \mathbf{G}^{\mathrm{xx}}_{\mathrm{TTT}}\boldsymbol{\Lambda}^{\mathrm{x,S}}\mathbf{I} + \mathbf{G}^{\mathrm{xx}}_{\mathrm{TTH}}\boldsymbol{\Lambda}^{\mathrm{x,S}}\mathbf{I}$: For the former multiplication, first, a 3-D array of size $(2N^{\mathrm{3D,x}}-1)\times(2N^{\mathrm{3D,y}}-1)\times(2N^{\mathrm{3D,z}}-1) \sim 8N^{\mathrm{3D}}$ is constructed by re-organizing and zero-padding the $\boldsymbol{\Lambda}^{\mathrm{x,S}}\mathbf{I}$ vector; the 3-D FFT of this array is computed; and the result is stored in ${}^{\mathrm{FFT}}\mathbf{I}^{\mathrm{x,S}}$. Second, ${}^{\mathrm{FFT}}\mathbf{I}^{\mathrm{x,S}}$ is multiplied element-by-element with ${}^{\mathrm{FFT}}\mathbf{G}^{\mathrm{xx}}_{\mathrm{TTT}}$, which is the 3-D FFT of an identical-sized array constructed from the unique entries of $\mathbf{G}^{\mathrm{xx}}_{\mathrm{TTT}}$. Third, the inverse 3-D FFT of the array resulting from this multiplication is found; and last, N^{3D} entries are extracted and re-organized to yield the desired vector $\mathbf{G}^{\mathrm{xx}}_{\mathrm{TTT}}\boldsymbol{\Lambda}^{\mathrm{x,S}}\mathbf{I}$. For the latter multiplication, it should be observed that Hankel blocks can be converted to Toeplitz ones by using a block anti-diagonal permutation matrix $\mathbf{Q}_{\mathrm{TTH}}$; i.e., $\mathbf{G}^{\mathrm{xx}}_{\mathrm{TTH}}\boldsymbol{\Lambda}^{\mathrm{x,S}}\mathbf{I} = (\mathbf{G}^{\mathrm{xx}}_{\mathrm{TTH}}\mathbf{Q}_{\mathrm{TTH}})(\mathbf{Q}^{-1}_{\mathrm{TTH}}\boldsymbol{\Lambda}^{\mathrm{x,S}}\mathbf{I})$, where $\mathbf{Q}^{-1}_{\mathrm{TTH}}\boldsymbol{\Lambda}^{\mathrm{x,S}}\mathbf{I}$ simply reorders the vector $\boldsymbol{\Lambda}^{\mathrm{x,S}}\mathbf{I}$ and $\mathbf{G}^{\mathrm{xx}}_{\mathrm{TTH}}\mathbf{Q}_{\mathrm{TTH}}$ is a 3-level block-Toeplitz matrix that can be multiplied with the reordered vector as before. The number of operations needed for this multiplication can be reduced significantly by recycling the FFTs found for

the former multiplication [59]-[62]. That is, $\mathbf{G}_{\mathrm{TTH}}^{\mathrm{xx}}\boldsymbol{\Lambda}^{\mathrm{x,S}}\mathbf{I}$ can be computed by multiplying ${}^{\mathrm{FFT}}\mathbf{I}^{\mathrm{x,S}}$ element-by-element with ${}^{\mathrm{FFT}}\mathbf{G}_{\mathrm{TTH}}^{\mathrm{xx}}$—the 3-D FFT of an array constructed from the unique entries of $\mathbf{G}_{\mathrm{TTH}}^{\mathrm{xx}}\mathbf{Q}_{\mathrm{TTH}}$, which is multiplied with a phase shift term to account for the reordering—inverse FFTing the resulting array, and extracting N^{3D} entries. This implies that if ${}^{\mathrm{FFT}}\mathbf{G}_{\mathrm{TTT}}^{\mathrm{xx}}$ and ${}^{\mathrm{FFT}}\mathbf{G}_{\mathrm{TTH}}^{\mathrm{xx}}$ are pre-computed before the iterative solution, as is typical, then computing $\mathbf{G}^{\mathrm{xx}}\boldsymbol{\Lambda}^{\mathrm{x,S}}\mathbf{I}$ requires no extra FFTs and a negligible number of extra operations compared to computing $\mathbf{G}_{\mathrm{TTT}}^{\mathrm{xx}}\boldsymbol{\Lambda}^{\mathrm{x,S}}\mathbf{I}$.

The anterpolation/interpolation matrices, the pre-corrected matrix, and the propagation matrices have $O(N)$, $O(N^{\mathrm{corr}})$, and $O(N^{\mathrm{3D}})$ unique entries and can be multiplied with a vector in $O(N)$, $O(N^{\mathrm{corr}})$, and $O(N^{\mathrm{3D}}\log N^{\mathrm{3D}})$ operations, respectively. Thus, the matrix fill time, memory cost, and matrix solve time of the proposed AIM scale as $O(N^{\mathrm{corr}}+N^{\mathrm{3D}})$, $O(N^{\mathrm{corr}}+N^{\mathrm{3D}})$, and $O(N^{\mathrm{it}}[N^{\mathrm{corr}}+N^{\mathrm{3D}}\log N^{\mathrm{3D}}])$ in general and as $O(N)$, $O(N^{1.5})$, and $O(N^{\mathrm{it}}N^{1.5})$ for single-scale 3-D PEC structures, respectively.

5.1.4 Comparison to Free Space

Next, the proposed 3-D AIM for structures in layered media is contrasted to the classical 3-D AIM for structures in free space. In the following cost analysis, it is assumed that the AIM implementations attempt to minimize the computation time rather than memory use; e.g., the FFTs of the arrays constructed from the propagation matrices are assumed to be pre-computed and stored rather than re-computed at each iteration.

For structures in free space, (5.1.10) is simplified as

$$\mathbf{Z}^{\mathrm{FFT}} = j\omega\mu_0\alpha \begin{bmatrix} \mathbf{\Lambda}^{\mathrm{x,S}} \\ \mathbf{\Lambda}^{\mathrm{y,S}} \\ \mathbf{\Lambda}^{\mathrm{z,S}} \end{bmatrix}^{\dagger} \begin{bmatrix} \mathbf{G} & \mathbf{0} & \mathbf{0} \\ \mathbf{0} & \mathbf{G} & \mathbf{0} \\ \mathbf{0} & \mathbf{0} & \mathbf{G} \end{bmatrix} \begin{bmatrix} \mathbf{\Lambda}^{\mathrm{x,S}} \\ \mathbf{\Lambda}^{\mathrm{y,S}} \\ \mathbf{\Lambda}^{\mathrm{z,S}} \end{bmatrix} + \frac{\alpha}{j\omega\varepsilon_0} \mathbf{\Lambda}^{\nabla,\mathrm{S}\dagger} \mathbf{G} \mathbf{\Lambda}^{\nabla,\mathrm{S}}$$
$$+(1-\alpha)\eta_\kappa \begin{bmatrix} \mathbf{\Gamma}^{\mathrm{x,S}} \\ \mathbf{\Gamma}^{\mathrm{y,S}} \\ \mathbf{\Gamma}^{\mathrm{z,S}} \end{bmatrix}^{\dagger} \begin{bmatrix} \mathbf{0} & -\partial_z \mathbf{G} & \partial_y \mathbf{G} \\ \partial_z \mathbf{G} & \mathbf{0} & -\partial_x \mathbf{G} \\ -\partial_y \mathbf{G} & \partial_x \mathbf{G} & \mathbf{0} \end{bmatrix} \begin{bmatrix} \mathbf{\Lambda}^{\mathrm{x,S}} \\ \mathbf{\Lambda}^{\mathrm{y,S}} \\ \mathbf{\Lambda}^{\mathrm{z,S}} \end{bmatrix} \tag{5.1.13}$$

Notice that there is only a single propagation matrix $\mathbf{G}$, whose entries are given in terms of the free-space Green function as in (5.1.11). At each iteration, 4 FFTs (for the different current components), 4 element-by-element multiplications, and 4 inverse FFTs must be computed for the EFIE contribution. These operations can be executed one current/field component at a time; thus, only 2 arrays of size $\sim 8N^{3\mathrm{D}}$ are needed (one for the pre-computed FFT for $\mathbf{G}$ and one for ${}^{\mathrm{FFT}}\mathbf{I}^{\{\mathrm{x,y,z},\nabla\},\mathrm{S}}$ or the result of the element-by-element multiplication). Similarly, 3 FFTs, 6 element-by-element multiplications, and 3 inverse FFTs must be computed for the MFIE contribution. This requires 7 arrays of size $\sim 8N^{3\mathrm{D}}$ (three for the pre-computed FFTs for $\partial_x\mathbf{G}$, $\partial_y\mathbf{G}$, and $\partial_z\mathbf{G}$; three for ${}^{\mathrm{FFT}}\mathbf{I}^{\{\mathrm{x,y,z}\},\mathrm{S}}$, and one for the result of element-by-element multiplications). In total, 4 FFTs, 10 element-by-element multiplications, and 7 inverse FFTs must be computed for the CFIE at each iteration. This requires 8 arrays of size $\sim 8N^{3\mathrm{D}}$. The computational cost of the CFIE can be reduced by employing numerical differentiation to calculate the MFIE contribution [95],[97]; this approach reduces the number of element-by-element multiplications and inverse FFTs to 4 and requires 5 arrays of size $\sim 8N^{3\mathrm{D}}$.

For structures in layered media, there are 15 different propagation matrices in (5.1.10) ($\mathbf{G}^{\mathrm{xx}} = \mathbf{G}^{\mathrm{yy}}$ and $\mathbf{G}^{\mathrm{zz}} + \mathbf{P}^{\mathrm{zz}}$ is stored as one matrix); each of these are decomposed into Toeplitz and Hankel terms that are stored and multiplied separately to

utilize 3-D FFTs (note ${}^{\mathrm{FFT}}\mathbf{G}^{\mathrm{zx,zy}}_{\mathrm{TTT}} = {}^{\mathrm{FFT}}\mathbf{P}^{\mathrm{xz,yz}}_{\mathrm{TTT}}$ and ${}^{\mathrm{FFT}}\mathbf{G}^{\mathrm{zx,zy}}_{\mathrm{TTH}} = -{}^{\mathrm{FFT}}\mathbf{P}^{\mathrm{xz,yz}}_{\mathrm{TTH}}$ when the structure confined in a single layer). At each iteration, at least 4 FFTs (for the different current components), 16 element-by-element multiplications (8 for Toeplitz and 8 for Hankel terms), and 4 inverse FFTs must be computed for the EFIE contribution. Because of the off-diagonal terms in (5.1.10), these operations cannot be executed one current/field component at a time without increasing the number of FFTs; instead, the FFTs for the Cartesian current components are computed once and stored; thus, 16 arrays of size $\sim 8N^{\mathrm{3D}}$ are needed (10 for the pre-computed FFTs for the Toeplitz and Hankel propagation matrices; 4 for ${}^{\mathrm{FFT}}\mathbf{I}^{\{\mathrm{x,y,z,\nabla\}\mathrm{,S}}}$; 1 for reordering ${}^{\mathrm{FFT}}\mathbf{I}^{\{\mathrm{x,y,z,\nabla\}\mathrm{,S}}}$, and 1 for inverse FFTs of field components;). Similarly, 3 FFTs, 16 element-by-element multiplications, and 3 inverse FFTs must be computed for the MFIE contribution. This requires 21 arrays of size $\sim 8N^{\mathrm{3D}}$ (16 for the pre-computed FFTs for propagation matrices; 3 for ${}^{\mathrm{FFT}}\mathbf{I}^{\{\mathrm{x,y,z\}\mathrm{,S}}}$; 1 for reordering ${}^{\mathrm{FFT}}\mathbf{I}^{\{\mathrm{x,y,z\}\mathrm{,S}}}$; and 1 for inverse FFTs of field components). In total, 4 FFTs, 32 element-by-element multiplications, and 7 inverse FFTs must be computed for the CFIE at each iteration. This requires 32 arrays of size $\sim 8N^{\mathrm{3D}}$. Although using numerical differentiation to calculate the MFIE contribution increases the number of inverse FFTs from 7 to 9, it also reduces both the number of element-by-element multiplications and the number of arrays to be stored from 32 to 18. In the following, the more accurate analytical differentiation is employed to calculate the MFIE contribution whenever possible; for larger N^{3D}, numerical differentiation is utilized.

In short, when solving the CFIE, AIM should require ~3.6 times the memory (18 instead of 5 arrays of size N^{3D}) and ~1.6 times the number of operations at each iteration

(13 instead of 8 forward and inverse FFTs) for large-scale structures in layered media as compared to the same structures in free space.

5.1.5 Numerical Results

This section presents several numerical results to demonstrate the performance of the proposed method. First, the accuracy of the Green function interpolation scheme is confirmed. Second, the AIM computational complexity is validated by analyzing scattering from PEC spheres in the top layer of a two-layer medium. Third, and last, various scattering problems are solved and compared to independent reference results. In all simulations, the AIM parameters (except the grid spacings), the preconditioner, and the iterative solver tolerance are the same as those described in Section 2.3. The proposed method is parallelized using an MPI-based implementation of the algorithm as in Chapter II and all simulations are performed on the Ranger cluster. The reported timing and memory data were "serialized" as described in Section 2.3.

5.1.5.1 Interpolation Error

A procedure similar to the one in [98] is used to confirm the accuracy of the spatial interpolation scheme detailed in Section 5.1.2. The interpolated Green functions are compared to those found by direct numerical integration for an isotropic two-layer medium whose top half is free space ($\tilde{\varepsilon}_2^{\mathrm{t}} = \varepsilon_0$, $\beta_2 = 1$) and bottom half is a dielectric with permittivity $\tilde{\varepsilon}_1^{\mathrm{t}} = 4\varepsilon_0$ and $\beta_1 = 1$. The interpolation error is quantified by computing the maximum relative error

$$err^{\mathrm{xx}} = \max_{\substack{\mathbf{r},\mathbf{r}'\in\mathrm{cube} \\ \mathbf{r}\neq\mathbf{r}'}} \frac{|\, \hat{g}^{\mathrm{xx}}_{\mathrm{TTT,num}}(\mathbf{r},\mathbf{r}') + \hat{g}^{\mathrm{xx}}_{\mathrm{TTH,num}}(\mathbf{r},\mathbf{r}') - g^{\mathrm{xx}}_{\mathrm{num}}(\mathbf{r},\mathbf{r}') \,|}{|\, g^{\mathrm{xx}}_{\mathrm{num}}(\mathbf{r},\mathbf{r}') \,|} \tag{5.1.14}$$

for a λ_1^3-m^3 cubic region whose top surface is λ_1-m below the interface; here, λ_1 is the wavelength in the bottom layer at 300 MHz. In (5.1.14), $g_{\mathrm{num}}^{\mathrm{xx}}$ is found directly via adaptive integration of the Sommerfeld integral, $\hat{g}_{\mathrm{TTT,num}}^{\mathrm{xx}}$ and $\hat{g}_{\mathrm{TTH,num}}^{\mathrm{xx}}$ are found by 2-D Lagrange interpolation, and the maximum is computed over 101^3 source/observer points uniformly distributed in the cubic region (the points are separated by $0.01\lambda_1$ in each direction). Fig. 5.2 plots the error versus the sample spacing for different interpolation orders; here, the sampling interval Δ is the same in the ρ and z directions, central interpolation is used wherever possible, and forward or backward interpolation is used otherwise (e.g., for $\left|\boldsymbol{\rho}-\boldsymbol{\rho}'\right|<\Delta$ or $2z_{\max}-\Delta<z+z'$). Fig. 5.2 shows that the error convergence is of polynomial order and that ~0.1% worst-case error can be obtained when ~10 samples per wavelength and fifth order interpolation are used. Similar plots were obtained for the other Green function and correction factor components but are not shown here for brevity. Accordingly, in all the following simulations, 10 samples per wavelength and fifth order interpolation are used when evaluating Green fucntions. Note that even

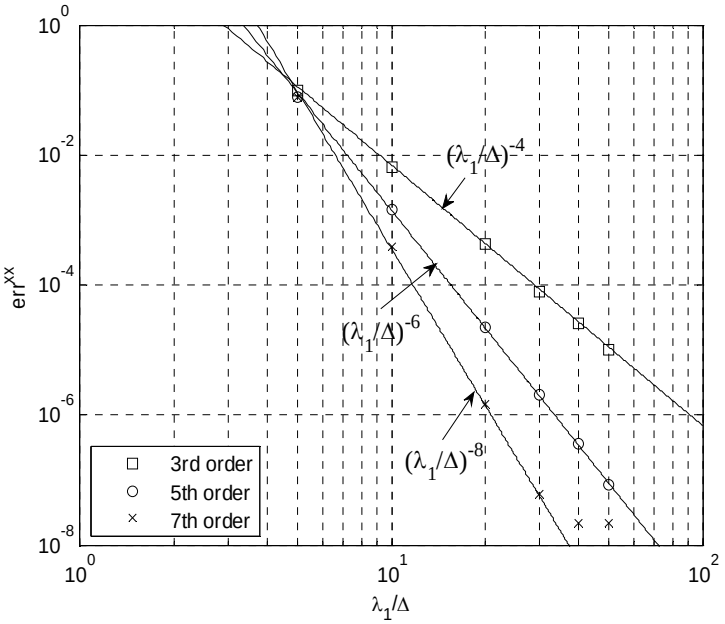

Figure 5.2: Green function interpolation error.

though double-precision arithmetic is used, the error is bounded by 10^{-8} in Fig. 5.2; this is because the samples found from direct numerical integration had only about 8 correct digits (due to numerical cancellation errors).

5.1.5.2 Computational Complexity

Next, the computational complexity of the proposed scheme is verified for {surface, volume} integral equation by analyzing scattering from a series of progressively larger {PEC, dielectric} spheres.

For surface integral equation, increasingly larger simulations are performed at 300 MHz by repeatedly doubling the sphere radius (from 0.5 m to 16 m) and keeping the surface

mesh density constant (average triangle edge length is $\sim \lambda_0 / 9$). This procedure is identical to the one in [64],[65] except the spheres are located not in free space but in the isotropic two-layer medium described in Section 5.1.5.1 (the bottoms of all spheres are located 0.5 m above the interface). As in [65], the spheres are illuminated by an x polarized plane wave propagating toward $-z$ direction and the accuracy of the simulations are quantified by computing $err^{\theta\theta}$, the relative root-mean-square error in the VV-polarized bistatic RCS. For reference, the MOM solution of the same problem is used; when this is not feasible, a more accurate AIM solution is used (fifth order moments are matched $[M_n^{\mathrm{S}} = 6 \times 6 \times 6]$, $\gamma = 3$, and the MFIE terms are computed via analytical differentiation). The AIM parameters are chosen to minimize the computational costs subject to the constraint that $err^{\theta\theta} < 0.5\%$; these parameters and the observed errors are detailed in Table 5.1. It is found that the parameters for the layered-medium simulations are only slightly more costly than those for the free-space ones; e.g., for the 16 m radius sphere, $N^{3\mathrm{D}} = 256^3$ when it is in free-space and $N^{3\mathrm{D}} = 288^3$ when it is in the two-layer medium (compare Table 5.1 to Table 2 in [65]). Note that to minimize the computational costs, the MFIE contributions are found by numerical differentiation when the sphere radius is more than 2 m and by analytical differentiation otherwise.

The computational requirements of AIM and MOM are contrasted in Figs. 5.3(a)-(c). The figures also compare layered-medium and free-space simulations on the same computer using the AIM parameters and the code developed in [65] for the free-space case. Overall, the observed data and the curves that are fitted to them in Fig. 5.3 agree well with the asymptotical trends described in Section 5.1.3. Several interesting features of the proposed method are evident in the plots. Fig. 5.3(a) shows that although the AIM matrix

fill time scales as $O(N)$ for both layered-medium and free-space simulations, matrix fill operations for layered medium simulations are only ~30 times slower than those for the corresponding free-space ones. This is because the evaluation of Green functions (and not numerical integrations) dominates the matrix fill time in layered media. Indeed, the 2-D interpolations, whose cost scales as $O(N)$, dominate other operations, including filling the tables until $N \sim 10^6$. Nevertheless, filling the tables, i.e., evaluating $\sim N$ Sommerfeld integrals, requires $O(N^{1.5})$ operations and will dominate the matrix fill time for $N > 10^6$ [Fig. 5.3(a)]. This is because the spectral-domain integrands oscillate faster with respect to k_ρ as the structure becomes larger and $L_{\max}$ increases (e.g., see the Bessel function in (5.1.3)); indeed, the cost of numerical integrations appear to scale proportionally with $|\boldsymbol{\rho} - \boldsymbol{\rho}'|$. The table fill time can be reduced by using approximate methods [93],[94] or amortized across different excitations and structures. Figs. 5.3(b)-(c) show that the AIM memory requirement and solution time per iteration asymptotically scales as $O(N^{1.5})$ and $O(N^{1.5} \log N)$ but the $O(N)$ memory costs and operations associated with the pre-correction and interpolation matrices are dominant until $N \sim 10^5$. As expected from Section 5.1.4, the memory requirements and (per iteration) solution times for layered-medium simulations are ~4 and ~2 times those for free-space simulations, respectively. For all simulations, only $N^{\mathrm{it}} = 20 - 50$ iterations were needed for convergence and N^{it} was insensitive to the sphere size because of the well-conditioned SCFIE formulation.

Table 5.1: Parameters for analyzing scattering from PEC spheres above half-space

Radius (m)	N	N^{3D}	γ	Reference	$err^{\theta\theta}(\%)$
0.5	684	9^3	2	MOM/AIM	0.09/0.09
1	3384	18^3	2	MOM/AIM	0.17/0.14
2	10 947	36^3	2	MOM/AIM	0.46/0.38
4	44 595	80^3	3	MOM/AIM	0.35/0.34
8	179 130	144^3	3	AIM	0.30
16	742 059	288^3	3	AIM	0.26

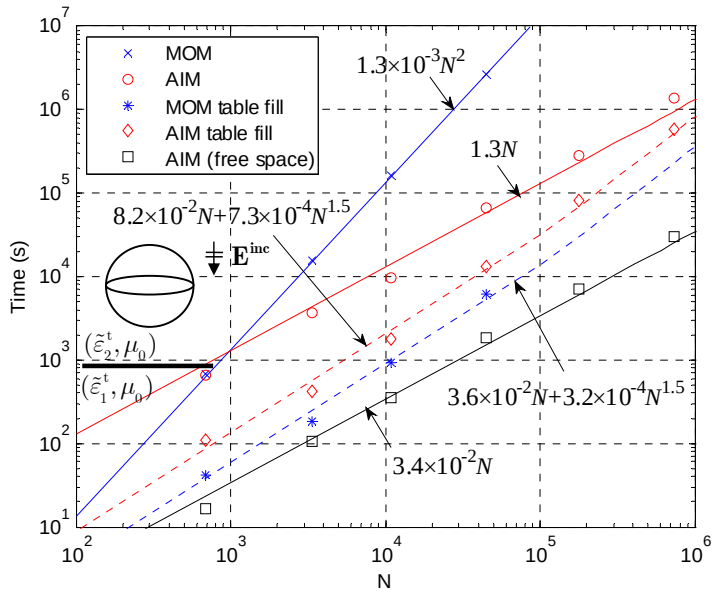

(a)

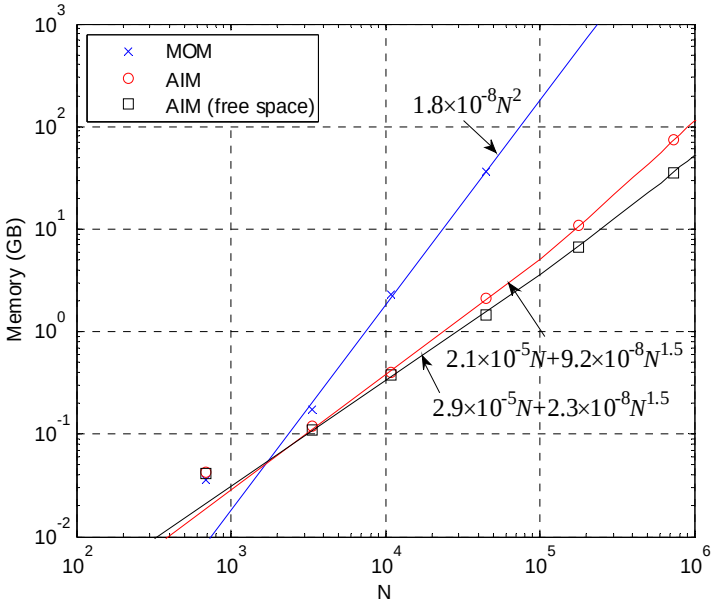

(b)

Figure 5.3: AIM vs. MOM for a PEC sphere in a two-layer medium as the sphere radius is increased. (a) Matrix fill time. (b) Memory requirement. (c) Average solution time per iteration.

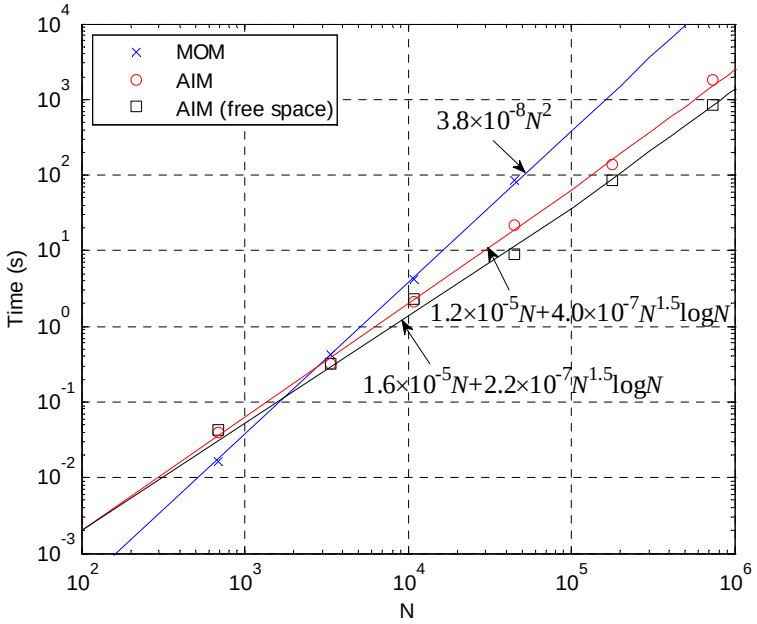

(c)

Figure 5.3: Continued.

For volume integral equation, increasingly larger simulations are performed at 0.25 Hz by repeatedly doubling the radius of a dielectric sphere (from 0.2 km to 1.6 km) and by keeping the mesh density constant, i.e., the average tetrahedron edge length is kept at $\delta_{\min}/10$, where $\delta_{\min} \approx 1.01\ \mathrm{km}$ denotes the minimum skin depth in the object or background medium. This procedure is identical to the previous one except the sphere is uniaxial ($\underline{\underline{\boldsymbol{\varepsilon}}}_{\mathrm{V}} = \varepsilon_0 \underline{\underline{\mathbf{I}}}$, $\sigma_{\mathrm{V}}^{\mathrm{xx}} = \sigma_{\mathrm{V}}^{\mathrm{yy}} = 0.01\ \mathrm{S/m}$, and $\sigma_{\mathrm{V}}^{\mathrm{zz}} = 2.5 \times 10^{-3}\ \mathrm{S/m}$) and is located in a three-layer medium composed of an unbounded uniaxial sea floor, a 1-km thick layer of sea water, and an unbounded air layer. The layer interfaces are at $z_1 = 0$ and $z_2 = 1\ \mathrm{km}$. The objects of interest are always illuminated by an impressed x-directed

Hertzian dipole located at $(x, y, z) = (0, 0, 50)\ \mathrm{m}$. All background media are assumed to be non-magnetic and $\varepsilon_k^{\mathrm{t}}$ of all layers k are set to 1. The electromagnetic properties of the layers are given as $\sigma_1^{\mathrm{t}} = 1\ \mathrm{S/m}$, $\sigma_2^{\mathrm{t}} = 10 / 3\ \mathrm{S/m}$, $\sigma_3^{\mathrm{t}} = 10^{-6}\ \mathrm{S/m}$, $\beta_1 = 1 / 3$, and $\beta_2 = \beta_3 = 1$. In each simulation, the top of the sphere is located 1 km below the sea floor-water interface and its center is aligned with the Hertzian dipole. After each simulation, a post-processing step is performed to find the electric field at $40\,401$ receiver points uniformly distributed on the sea floor –10 km to 10 km in x and y directions. The accuracy of the solution is quantified by computing err^{xx}, the relative root-mean-square error in the x-component of the electric field at the receiver locations. The MOM and a more-accurate AIM solution (fourth order moments are matched and $\gamma = 3$) of the same problem are used as reference in Table 5.2, which lists the AIM parameters that were used, the number of iterations needed for convergence, and the observed errors. Table 5.2 shows that the errors with respect to the MOM solution are similar to those with respect to the more-accurate AIM solution; hence, the latter can be used to estimate the error when the MOM solution is infeasible. The corresponding AIM and MOM computational costs are contrasted in Fig. 5.4. Similar to the surface integral equation, the observed data and the curves that are fitted to them agree well with the expected asymptotical trends described in Section 5.1.3, where the matrix fill time, memory cost, and matrix solve time per iteration of the proposed AIM scale as $O(N)$, $O(N)$, and $O(N \log N)$ for single-scale 3-D dielectric structures, respectively. AIM outperforms MOM in all the performance metrics for N greater than ~5000.

Table 5.2: Parameters for uniaxial spheres in a three-layer medium

Radius (km)	N	N^{3D}	γ	Reference	# of iteration	$err^{xx}(\%)$
0.2	849	14^3	2	MOM/AIM	33/34	0.21/0.01
0.4	6364	21^3	2	MOM/AIM	36/36	0.09/0.06
0.8	49 128	40^3	2	MOM/AIM	46/46	0.06/0.02
1.6	375 949	72^3	2	AIM	63	0.04

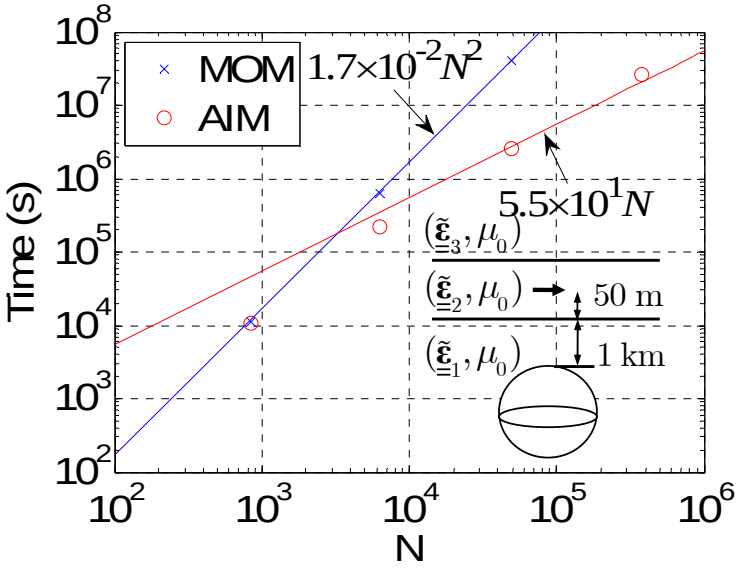

(a)

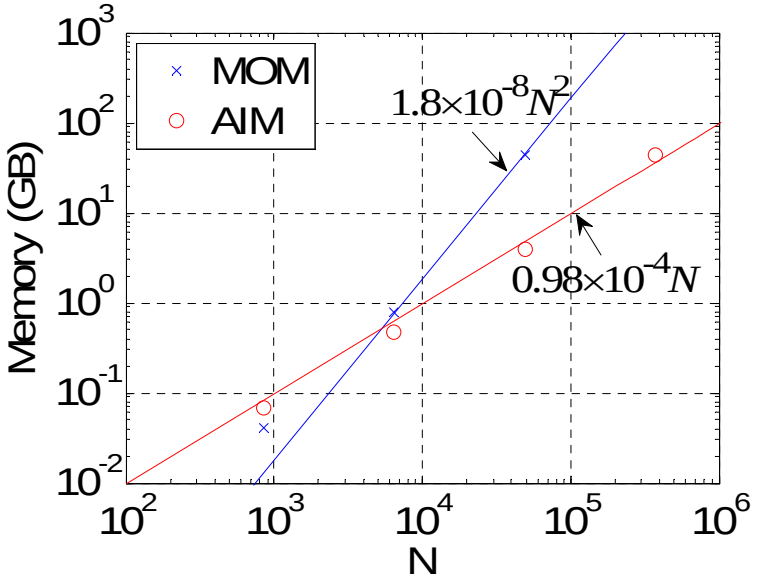

(b)

Figure 5.4: AIM vs. MOM for a uniaxial sphere as the sphere radius is increased. (a) Matrix fill time. (b) Memory requirement. (c) Average solution time per iteration.

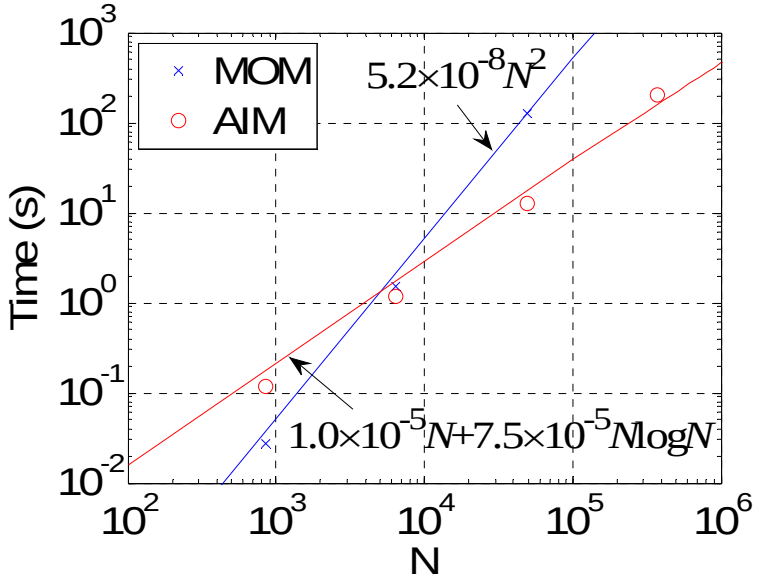

(c)

Figure 5.4: Continued.

5.1.5.3 Validation

Next, the viability of the proposed scheme for scattering analysis is demonstrated by analyzing scattering from two 3-D PEC structures: An unexploded ordnance (UXO) model [13] and a cylinder [99]. In the following simulations, the AIM parameters are set as follows: Third order moments are matched, $\gamma = 3$, and the SMFIE terms are computed using numerical differentiation. All background media are assumed to be isotropic and β_k of all layers k are set to 1.

The UXO model, which is a hemisphere capped cylinder, is 153 cm long and has a diameter of 40.6 cm; its axis lies in the yoz plane and is tilted 75° with respect to the vertical axis. Its top is located 30.4 cm below the interface of a two-layer dielectric medium, where $\tilde{\varepsilon}_1^{\mathrm{t}} = 3.47 - j0.31$ (Yuma soil with 5% water content), $\tilde{\varepsilon}_2^{\mathrm{t}} = 1$, and the interface

is at $z_1 = 0$. The UXO is excited by a 500-MHz plane wave incident from $\theta^{\text{inc}} = 60^\circ$ and $\phi^{\text{inc}} = 0^\circ$. The surface of the UXO is discretized using triangles with $\sim \lambda_1 / 10.5$ average edge length and the auxiliary grid spacing is $\sim \lambda_1 / 10$ in all three directions, where λ_1 is the wavelength in the bottom layer; hence, $N = 7617$ and $N^{\text{3D}} = 20 \times 48 \times 47$. The RCS patterns calculated with 3-D AIM are compared to those calculated by a reference high order MOM [13] in Fig. 5.5; the results are essentially identical. This simulation required $\sim 1.4 \times 10^4$ seconds for filling the matrices ($\sim 2.9 \times 10^2$ seconds for filling the tables), 310 MB memory, 18.8 seconds per iteration, and N^{it}=36 iterations.

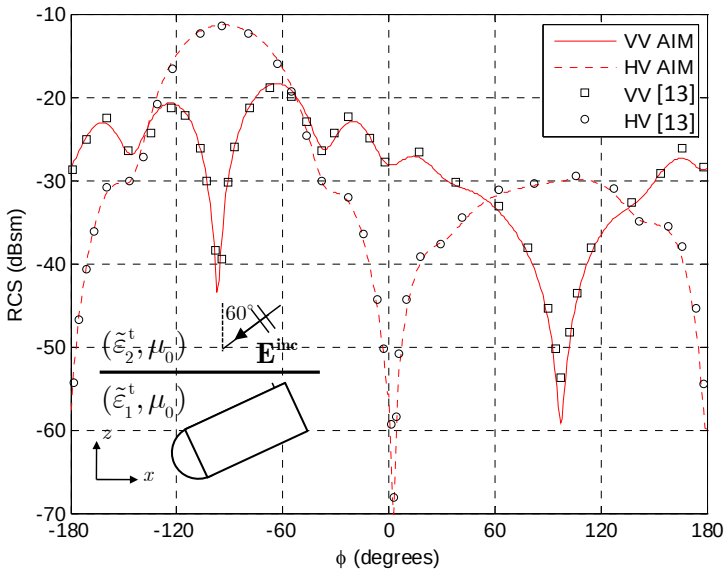

Figure 5.5: V-polarized bistatic RCS of the UXO in a two-layer medium in the $\theta = 50^\circ$ cut at 500 MHz.

The cylinder is 3 m long, has a radius of 0.5 m, and its bottom is located 0.2 m above the top interface of a three-layer dielectric medium, where $\tilde{\varepsilon}_1^{\mathrm{t}} = 6.5 - j0.6$, $\tilde{\varepsilon}_2^{\mathrm{t}} = 2.56$, $\tilde{\varepsilon}_3^{\mathrm{t}} = 1$, and the interfaces are at $z_1 = 0$ and $z_2 = 0.3\ \mathrm{m}$. The cylinder is excited by a 600-MHz plane wave incident from $\theta^{\mathrm{inc}} = 60^\circ$ and $\phi^{\mathrm{inc}} = 0^\circ$. The surface of the cylinder is discretized using triangles with $\sim \lambda_0 / 7.4$ average edge length and the auxiliary grid spacing is $\sim \lambda_0 / 10$ in all three directions, where λ_0 is the wavelength in free space; hence, $N = 10\ 800$ and $N^{\mathrm{3D}} = 30 \times 30 \times 70$. The RCS patterns calculated with the proposed 3-D AIM are compared to those calculated by the classical MOM and a reference fast inhomogeneous plane wave algorithm (FIPWA) accelerated MOM [99] in Fig. 5.6. The patterns are visually identical. This simulation required $\sim 1.1 \times 10^4$ seconds for filling the matrices ($\sim 1.8 \times 10^3$ seconds for filling the tables), 565 MB memory, 19.6 seconds per iteration, and $N^{\mathrm{it}} = 74$ iterations.

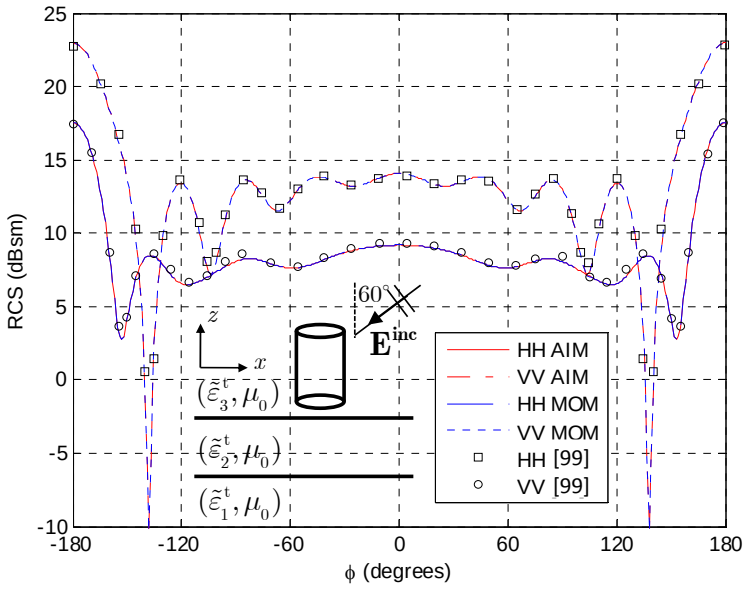

Figure 5.6: Copolarized bistatic RCS patterns of the cylinder in a three-layer medium in the $\theta = 60^\circ$ cut at 600 MHz.

5.2 MULTILAYER EXTENSION OF AIM FOR LAYERED MEDIA

This section first formulates the AIM extension for the structures embedded in multiple layers of a uniaxial planar-layered medium. Then, this extension is validated by numerical results.

5.2.1 AIM

Consider a time-harmonic electric field $\mathbf{E}^{\text{inc}}$ that is incident on a PEC structure residing in the same planar-layered medium as in Section 5.1.1. To highlight the key properties of the algorithm, it is assumed that the structure is composed of K arbitrarily shaped *disjoint* 3-D surfaces $S_1,\ldots,S_K$ such that each surface S_k is embedded in a different layer k (Fig. 5.7(a)). The surface electric-field integral equation is formulated

as in Section 5.1.1 by setting $\alpha = 1$ and solved using the MOM procedure as in Section 5.1.2, which yields the dense linear system of equations

$$\begin{bmatrix} \mathbf{Z}_{1,1} & \cdots & \mathbf{Z}_{1,k} & \cdots & \mathbf{Z}_{1,K} \\ \vdots & & \vdots & & \vdots \\ \mathbf{Z}_{k,1} & \cdots & \mathbf{Z}_{k,k} & \cdots & \mathbf{Z}_{k,K} \\ \vdots & & \vdots & & \vdots \\ \mathbf{Z}_{K,1} & \cdots & \mathbf{Z}_{K,k} & \cdots & \mathbf{Z}_{K,K} \end{bmatrix} \begin{bmatrix} \mathbf{I}_1 \\ \vdots \\ \mathbf{I}_k \\ \vdots \\ \mathbf{I}_K \end{bmatrix} = \begin{bmatrix} \mathbf{V}_1^{\text{inc}} \\ \vdots \\ \mathbf{V}_k^{\text{inc}} \\ \vdots \\ \mathbf{V}_K^{\text{inc}} \end{bmatrix} \tag{5.2.1}$$

Here, the $\mathbf{V}_k^{\text{inc}}$ sub-vector accounts for the incident field on S_k and the $\mathbf{Z}_{kk'}$ sub-matrix accounts for the field scattered onto S_k by the current on $S_{k'}$; their entries are the same as in (5.1.7) by setting $\alpha = 1$. The MOM computational complexity is reduced by using the following extension of AIM.

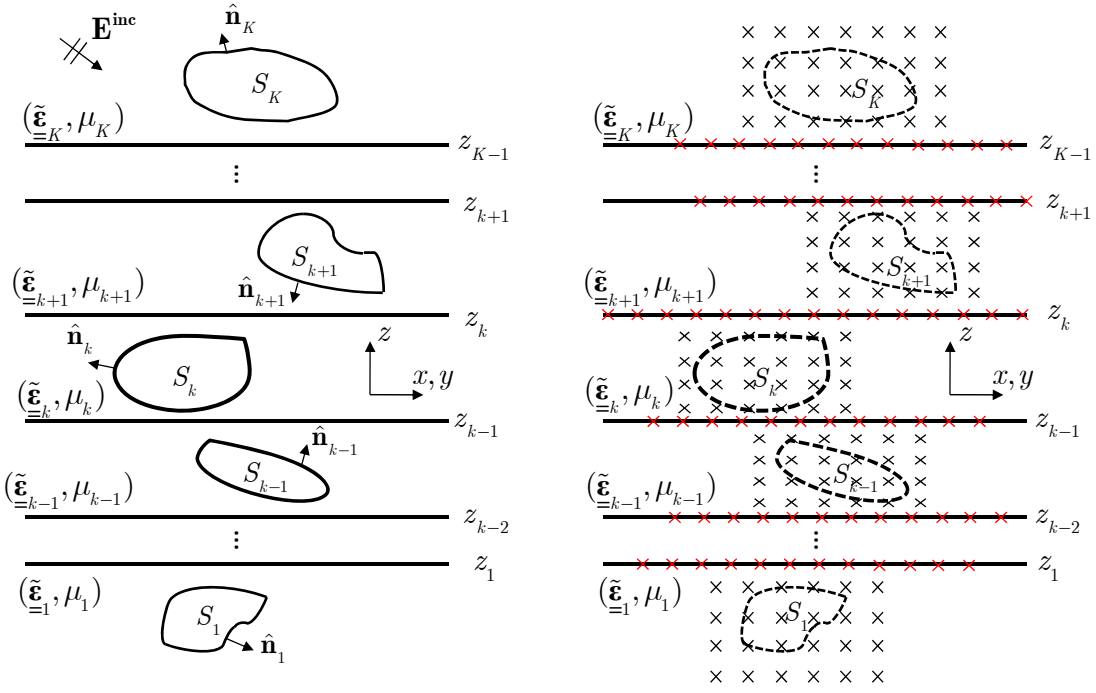

Figure 5.7: Scattering from a 3-D structure composed of K disjoint surfaces that reside in different layers of a stratified medium with K layers. (a) Geometry and excitation definition. (b) The auxiliary 2-D and 3-D grid points.

In the proposed algorithm, first $2K-1$ auxiliary grids are introduced: Each auxiliary grid $k=1,\ldots,K$ is a 3-D regular grid composed of $N_k^{\text{3D}} = N_k^{\text{3D,x}} N_k^{\text{3D,y}} N_k^{\text{3D,z}}$ nodes that are separated by a distance of Δx_k^{3D}, Δy_k^{3D}, and Δz_k^{3D} from their neighbors in the three Cartesian directions, respectively (black crosses in Fig. 5.7(b)); these nodes must be located such that they enclose the surface S_k and reside entirely inside the layer k. Each auxiliary grid $k=K+1,\ldots,2K-1$ is a 2-D regular grid composed of $N_k^{\text{2D}} = N_k^{\text{2D,x}} N_k^{\text{2D,y}}$ nodes that are separated by a distance of Δx_k^{2D} and Δy_k^{2D} from

their neighbors in the horizontal plane (red crosses in Fig. 5.7(b)); these nodes are located at the interface of layers $k-K$ and $k-K+1$. To be able to calculate the inter-layer interactions with FFTs, the node spacing of all 2-D and 3-D auxiliary grids are constrained to be identical in the transverse directions, i.e., $\{\Delta x^{\mathrm{3D}}_{1,\ldots,K}, \Delta y^{\mathrm{3D}}_{1,\ldots,K}\} = \{\Delta x, \Delta y\}$ and $\{\Delta x^{\mathrm{2D}}_{K+1,\ldots,2K-1}, \Delta y^{\mathrm{2D}}_{K+1,\ldots,2K-1}\} = \{\Delta x, \Delta y\}$.

Similar to the classical AIM for structures in free space, the auxiliary grids are used to approximate each impedance sub-matrix as $\mathbf{Z}_{k,k'} \approx \mathbf{Z}^{\mathrm{corr}}_{k,k'} + \mathbf{Z}^{\mathrm{FFT}}_{k,k'}$, where $\mathbf{Z}^{\mathrm{corr}}_{k,k'}$ is a "pre-corrected" matrix that insures the accuracy of the method by replacing the contribution from the $\mathbf{Z}^{\mathrm{FFT}}_{k.k'}$ matrix with that from the $\mathbf{Z}_{k,k'}$ matrix when the basis and testing functions are near each other (the size of correction region is defined by the parameter γ). The $\mathbf{Z}^{\mathrm{FFT}}_{k.k'}$ matrices represent anterpolation (mesh-to-grid), propagation (grid-to-grid), and interpolation (grid-to-mesh) operations; they are formulated next.

The propagation step is divided into two parts (the intra-layer and inter-layer interactions) based on whether basis and testing functions are in the same layer. The intra-layer interactions between basis and testing functions in each layer k are approximated by the $\mathbf{Z}^{\mathrm{FFT}}_{k.k'}$ matrix. These interactions are calculated by the AIM procedure (anterpolation to, propagation on, and interpolation from only the 3-D regular grid k) described in the previous section; thus, the matrix can be expressed as

$$\mathbf{Z}^{\mathrm{FFT}}_{k,k'} = \begin{bmatrix} \boldsymbol{\Lambda}^{\mathrm{x,S}}_{k} \\ \boldsymbol{\Lambda}^{\mathrm{y,S}}_{k} \\ \boldsymbol{\Lambda}^{\mathrm{z,S}}_{k} \\ \boldsymbol{\Lambda}^{\nabla,\mathrm{S}}_{k} \end{bmatrix}^{\dagger} \underbrace{\begin{bmatrix} \mathbf{G}^{\mathrm{xx}}_{k,k'} & \mathbf{0} & \mathbf{P}^{\mathrm{xz}}_{k,k'} & \mathbf{0} \\ \mathbf{0} & \mathbf{G}^{\mathrm{yy}}_{k,k'} & \mathbf{P}^{\mathrm{yz}}_{k,k'} & \mathbf{0} \\ \mathbf{G}^{\mathrm{zx}}_{k,k'} & \mathbf{G}^{\mathrm{zy}}_{k,k'} & \mathbf{G}^{\mathrm{zz}}_{k,k'} + \mathbf{P}^{\mathrm{zz}}_{k,k'} & \mathbf{0} \\ \mathbf{0} & \mathbf{0} & \mathbf{0} & \mathbf{G}^{\phi}_{k,k'} \end{bmatrix}}_{\mathbf{G}^{\mathrm{3D,3D}}_{k,k'}} \begin{bmatrix} j\omega\mu_0 \boldsymbol{\Lambda}^{\mathrm{x,S}}_{k'} \\ j\omega\mu_0 \boldsymbol{\Lambda}^{\mathrm{y,S}}_{k'} \\ j\omega\mu_0 \boldsymbol{\Lambda}^{\mathrm{z,S}}_{k'} \\ \dfrac{1}{j\omega\varepsilon_0} \boldsymbol{\Lambda}^{\nabla,\mathrm{S}}_{k'} \end{bmatrix} \tag{5.2.2}$$

Intra-Layer Propagation Step: In (5.2.2), the $\mathbf{G}_{k,k'}^{\mathrm{xx,yy,zx,zy,zz},\phi}$ and $\mathbf{P}_{k,k'}^{\mathrm{xz,yz,zz}}$ are dense $N_k^{\mathrm{3D}} \times N_k^{\mathrm{3D}}$ matrices that represent propagation from sources on auxiliary grid k to observers on the same auxiliary grid. As detailed in the previous section, these propagation matrices can be expressed as the sum of a three-level block-Toeplitz and a Hankel-two-level-block Toeplitz matrix, which can be multiplied with a size N_k^{3D} vector in $O(N_k^{\mathrm{3D}} \log N_k^{\mathrm{3D}})$ operations by using 3-D FFTs. This decomposition is not applicable, however, if the sources and observers are in different layers.

The inter-layer interactions between basis functions in layer k' and testing functions in layer $k \neq k'$ are approximated by the $\mathbf{Z}_{k.k'}^{\mathrm{FFT}}$ matrix. In the proposed scheme, these interactions are calculated by using not only the 3-D grids k and k' but also all 2-D grids that reside between them, i.e. in the expression,

$$\mathbf{Z}_{k,k'}^{\mathrm{FFT}} = \begin{bmatrix} \mathbf{\Lambda}_k^{\mathrm{x,S}} \\ \mathbf{\Lambda}_k^{\mathrm{y,S}} \\ \mathbf{\Lambda}_k^{\mathrm{z,S}} \\ \mathbf{\Lambda}_k^{\nabla,\mathrm{S}} \end{bmatrix}^{\dagger} \mathbf{G}_{k,k'}^{\mathrm{3D,3D}} \begin{bmatrix} j\omega\mu_0 \mathbf{\Lambda}_{k'}^{\mathrm{x,S}} \\ j\omega\mu_0 \mathbf{\Lambda}_{k'}^{\mathrm{y,S}} \\ j\omega\mu_0 \mathbf{\Lambda}_{k'}^{\mathrm{z,S}} \\ \dfrac{1}{j\omega\varepsilon_0} \mathbf{\Lambda}_{k'}^{\nabla,\mathrm{S}} \end{bmatrix} \tag{5.2.3}$$

the matrix $\mathbf{G}_{k,k'}^{\mathrm{3D,3D}}$ is replaced by

$$\mathbf{G}_{k,k'}^{\mathrm{3D,3D}} \approx \begin{cases} \mathbf{G}_{k,K+k-1}^{\mathrm{3D,2D}} \left(\prod_{j=-k-K+1}^{-K-k'-1} \mathbf{G}_{-j,-j-1}^{\mathrm{2D,2D}} \right) \mathbf{G}_{K+k',k'}^{\mathrm{2D,3D}} & \text{if } k > k' \\ \mathbf{G}_{k,K+k}^{\mathrm{3D,2D}} \left(\prod_{j=K+k}^{K+k'-2} \mathbf{G}_{j,j+1}^{\mathrm{2D,2D}} \right) \mathbf{G}_{K+k'-1,k'}^{\mathrm{2D,3D}} & \text{if } k < k' \end{cases} \tag{5.2.4}$$

As shown in the above expression, neither the anterpolation nor the interpolation stages of the AIM scheme are varied in the proposed scheme. Instead, the propagation stage is now performed in three steps for inter-layer interactions.

Inter-Layer Propagation Step 1: The 3-D grid to 2-D grid propagation matrix $\mathbf{G}^{2D,3D}_{K+k',k'}$ ($\mathbf{G}^{2D,3D}_{K+k'-1,k'}$) is used to find the samples of the tangential electric and magnetic fields (only E_x, E_y, H_x, H_y) on the upper (lower) interface of layer k' due to four components of sources ($\boldsymbol{\Lambda}^{x,S}_{k'}, \boldsymbol{\Lambda}^{y,S}_{k'}, \boldsymbol{\Lambda}^{z,S}_{k'}, \boldsymbol{\Lambda}^{\nabla,S}_{k'}$) on the 3-D grid in that layer based on (5.1.2) ; this propagation matrix is given as

$$\mathbf{G}^{2D,3D}_{j,k'} = \begin{bmatrix} -\mathbf{G}^{xx}_{j,k'} & \mathbf{0} & -\mathbf{P}^{xz}_{j,k'} & -\partial_x \mathbf{G}^{\phi}_{j,k'} \\ \mathbf{0} & -\mathbf{G}^{yy}_{j,k'} & -\mathbf{P}^{yz}_{j,k'} & -\partial_y \mathbf{G}^{\phi}_{j,k'} \\ \dfrac{\partial_y \mathbf{G}^{zx}_{j,k'}}{j\omega\mu_0} & \dfrac{\partial_y \mathbf{G}^{zy}_{j,k'} - \partial_z \mathbf{G}^{yy}_{j,k'}}{j\omega\mu_0} & \dfrac{\partial_y \mathbf{G}^{zz}_{j,k'}}{j\omega\mu_0} & \mathbf{0} \\ \dfrac{\partial_z \mathbf{G}^{xx}_{j,k'} - \partial_x \mathbf{G}^{zx}_{j,k'}}{j\omega\mu_0} & \dfrac{-\partial_x \mathbf{G}^{zy}_{j,k'}}{j\omega\mu_0} & \dfrac{-\partial_x \mathbf{G}^{zz}_{j,k'}}{j\omega\mu_0} & \mathbf{0} \end{bmatrix} \quad (5.2.5)$$

where $j = K + k'$ ($j = K + k' - 1$). Here, $\partial_{x,y,z}$ represents the partial derivative with respect to x, y, z, respectively. The first two rows of $\mathbf{G}^{2D,3D}_{j,k'}$ store the propagators that are used to computed the samples of E_x and E_y while the last two rows of $\mathbf{G}^{2D,3D}_{j,k'}$ store the propagators that are used to computed the samples of H_x and H_y.

Inter-Layer Propagation Step 2: The electric and magnetic field samples on the interface are converted to equivalent magnetic and electric current sources by calculating their cross-product with the $\hat{\mathbf{z}}$ vector if $k > k'$ and $-\hat{\mathbf{z}}$ vector if $k < k'$. Then, the samples of the fields on the next interface above or below are found by using a 2-D grid to 2-D grid propagation matrix. In (5.2.3), the $\mathbf{G}^{2D,2D}_{K+k'+1,K+k'}$ matrix includes the effect of the cross product as well as the propagation and is given as

$$\mathbf{G}_{j,i}^{\mathrm{2D,2D}} = \begin{bmatrix} -\mathbf{G}_{j,i}^{\mathrm{EM,xy}} & \mathbf{G}_{j,i}^{\mathrm{EM,xx}} & \mathbf{G}_{j,i}^{\mathrm{EJ,xy}} & -\mathbf{G}_{j,i}^{\mathrm{EJ,xx}} \\ -\mathbf{G}_{j,i}^{\mathrm{EM,yy}} & \mathbf{G}_{j,i}^{\mathrm{EM,yx}} & \mathbf{G}_{j,i}^{\mathrm{EJ,yy}} & -\mathbf{G}_{j,i}^{\mathrm{EJ,yx}} \\ -\mathbf{G}_{j,i}^{\mathrm{HM,xy}} & \mathbf{G}_{j,i}^{\mathrm{HM,xx}} & \mathbf{G}_{j,i}^{\mathrm{HJ,xy}} & -\mathbf{G}_{j,i}^{\mathrm{HJ,xx}} \\ -\mathbf{G}_{j,i}^{\mathrm{HM,yy}} & \mathbf{G}_{j,i}^{\mathrm{HM,yx}} & \mathbf{G}_{j,i}^{\mathrm{HJ,yy}} & -\mathbf{G}_{j,i}^{\mathrm{HJ,yx}} \end{bmatrix} \tag{5.2.6}$$

where $i = K + k'$ and $j = K + k' + 1$. The expression for $\mathbf{G}_{K+k'-2,K+k'-1}^{\mathrm{2D,2D}}$ is found by setting $i = K + k' - 2$ and $j = K + k' - 1$ in (5.2.6) and multiplying the right-hand side with -1. Here, $\mathbf{G}_{j,i}^{\{\mathrm{EM,EJ,HM,HJ}\},\mathrm{uv}}$ are the propagators that compute the u-directed electric or magnetic field on the 2-D grid j due to a v-directed electric or magnetic dipoles located on the 2-D grid i. Different from the propagators in (5.2.2) and (5.2.5), $\mathbf{G}_{j,i}^{\{\mathrm{EM,EJ,HM,HJ}\},\mathrm{uv}}$ store dyadic rather than mixed-potential layered-medium Green functions as only the dipole current samples are known on the interface. The expressions for dyadic layered-medium Green functions can be found in [91],[101].

Inter-Layer Propagation Step 3: The step 2 is repeated until all the layers between the source and observer grid are traversed. Once the electric and magnetic field samples are found on the interface below (above) layer k, the vector and scalar potentials on the 3-D grid in layer k are found by using the 2-D grid to 3-D grid propagation matrix $\mathbf{G}_{k,K+k-1}^{\mathrm{3D,2D}}$, which is given as

$$\mathbf{G}_{k,j}^{\mathrm{3D,2D}} = \begin{bmatrix} \mathbf{G}_{k,j}^{\mathrm{EM,xy}} & -\mathbf{G}_{k,j}^{\mathrm{EM,xx}} & \mathbf{0} & \mathbf{G}_{k,j}^{\mathrm{xx}} \\ \mathbf{G}_{k,j}^{\mathrm{EM,yy}} & -\mathbf{G}_{k,j}^{\mathrm{EM,yx}} & -\mathbf{G}_{k,j}^{\mathrm{yy}} & \mathbf{0} \\ \mathbf{G}_{k,j}^{\mathrm{EM,zy}} & -\mathbf{G}_{k,j}^{\mathrm{EM,zx}} & -\mathbf{G}_{k,j}^{\mathrm{zy}} & \mathbf{G}_{k,j}^{\mathrm{zx}} \\ \mathbf{0} & \mathbf{0} & \begin{pmatrix} -\partial_y \mathbf{G}_{k,j}^{\mathrm{yy}} \\ -\partial_z \mathbf{G}_{k,j}^{\mathrm{zy}} \end{pmatrix} & \begin{pmatrix} \partial_z \mathbf{G}_{k,j}^{\mathrm{zx}} \\ +\partial_x \mathbf{G}_{k,j}^{\mathrm{xx}} \end{pmatrix} \end{bmatrix} \tag{5.2.7}$$

where $j = K + k - 1$. The expression for $\mathbf{G}_{k,K+k}^{\mathrm{3D,2D}}$ is found by setting $j = K + k$ in (5.2.7) and multiplying the right-hand side with -1. The first two columns of $\mathbf{G}_{k,j}^{\mathrm{3D,2D}}$ store

the propagators that are used to compute the tested vector and scalar potential due to tangential magnetic currents while the last two columns of $\mathbf{G}_{k,j}^{\mathrm{3D,2D}}$ store the propagators that are used to computed the tested vector and scalar potential due to tangential electric current.

Because layered-medium Green functions are translationally invariant in the transverse directions, all the matrices in (5.2.5)-(5.2.7) are (two level) block-Toeplitz matrices and can be efficiently multiplied with vectors using 2-D FFTs. For example, consider the calculation of $\mathbf{G}_{K+k',k'}^{\mathrm{xx}}\boldsymbol{\Lambda}_{k'}^{\mathrm{x,S}}\mathbf{I}_{k'}$: After the anterpolation step is performed and the $\boldsymbol{\Lambda}_{k'}^{\mathrm{x,S}}\mathbf{I}_{k'}$ vector is found, first, $N_{k'}^{\mathrm{3D,z}}$ different 2-D arrays of size $N_{K+k',k'}^{\mathrm{xy}}$ are constructed by re-organizing and zero-padding the $\boldsymbol{\Lambda}_{k'}^{\mathrm{x,S}}\mathbf{I}_{k'}$ vector, where $N_{K+k',k'}^{\mathrm{xy}} = (N_{k'}^{\mathrm{3D,x}} + N_{K+k'}^{\mathrm{2D,x}} - 1)(N_{k'}^{\mathrm{3D,y}} + N_{K+k'}^{\mathrm{2D,y}} - 1)$. Second, the 2-D FFTs of $N_{k'}^{\mathrm{3D,z}}$ other arrays of the same size that are constructed from the unique entries of $\mathbf{G}_{K+k',k'}^{\mathrm{xx}}$ are computed. Third, these are multiplied element by element and added to form one 2-D array. Fourth, the inverse 2-D FFTs of the array resulting from this multiplication is found and $N_{K+k'}^{\mathrm{2D}}$ entries are extracted and re-organized as part of the desired vector $\mathbf{G}_{K+k',k'}^{\mathrm{xx}}\boldsymbol{\Lambda}_{k'}^{\mathrm{x,S}}\mathbf{I}_{k'}$. The intra-layer interactions are computed efficiently by performing an upward and a downward pass as follows:

Upward Pass: Starting at layer $k' = 1$, (i) anterpolate from the triangular mesh of $S_{k'}$ to the 3-D grid k' ; (ii) propagate from the 3-D grid k' to the 2-D grid $K + k'$ at the upper boundary of the layer if it exists (if $k' < K$) (*inter-layer propagation step 1*); (iii) if the 2-D grid $K + k' - 1$ at the lower boundary of the layer exists (if $k' > 1$) then also propagate from this 2-D grid to the 2-D grid $K + k'$ at the upper boundary of the layer if it exists (if $k' < K$) (*inter-layer propagation step 2*) and to the 3-D grid k'

(*inter-layer propagation step 3*); (iv) interpolate from the 3-D grid k' onto the triangular mesh of $S_{k'}$ if it received any information from the layers below it during the upward pass (if $k' > 1$). Then, increase k' by 1 and repeat these four steps if $k' \leq K$.

Downward Pass: Starting at layer $k' = K$, (i) anterpolate from the triangular mesh of $S_{k'}$ to the 3-D grid k'; (ii) propagate from the 3-D grid k' to itself (*intra-layer propagation step*) and to the 2-D grid $K + k' - 1$ at the lower boundary of the layer if it exists (if $k' > 1$) (*inter-layer propagation step 1*); (iii) if the 2-D grid $K + k'$ at the upper boundary of the layer exists (if $k' < K$) then also propagate from this 2-D grid to the 2-D grid $K + k' - 1$ at the lower boundary of the layer if it exists (if $k' > 1$) (*inter-layer propagation step 2*) and to the 3-D grid k' (*inter-layer propagation step 3*); (iv) interpolate from the 3-D grid k' on to the triangular mesh of $S_{k'}$. Decrease k' by 1 and repeat these four steps if $k' \geq 1$.

At each iteration, the dominant costs of the algorithm are the steps (ii) and (iii) of the upward and downward pass. Step (ii) of upward pass requires $O(\sum_{k'=1}^{K-1} N_{k'}^{\mathrm{3D,z}} N_{K+k',k'}^{\mathrm{xy}} \log N_{K+k',k'}^{\mathrm{xy}})$ operations and step (iii) of upward pass requires $O(\sum_{k'=2}^{K-1} N_{K+k',K+k'-1}^{\mathrm{xy}} \log N_{K+k',K+k'-1}^{\mathrm{xy}} + N_{k'}^{\mathrm{3D,z}} N_{k',K+k'-1}^{\mathrm{xy}} \log N_{k',K+k'-1}^{\mathrm{xy}})$ operations. Step (ii) of downward pass requires $O(\sum_{k'=1}^{K} N_{k'}^{\mathrm{3D}} \log N_{k'}^{\mathrm{3D}}$ $+\sum_{k'=2}^{K} N_{k'}^{\mathrm{3D,z}} N_{K+k'-1,k'}^{\mathrm{xy}} \log N_{K+k'-1,k'}^{\mathrm{xy}})$ operations and step (iii) of downward pass requires $O(\sum_{k'=2}^{K-1} N_{K+k'-1,K+k'}^{\mathrm{xy}} \log N_{K+k'-1,K+k'}^{\mathrm{xy}} + \sum_{k'=1}^{K-1} N_{k'}^{\mathrm{3D,z}} N_{k',K+k'}^{\mathrm{xy}} \log N_{k',K+k'}^{\mathrm{xy}}$ operations. If the size of all the 2-D grids on the interfaces and the transverse size of all the 3-D grids inside each layer are comparable, then all these steps require approximately the same number of operations.

5.2.2 Numerical Results

This section presents numerical results that demonstrate the performance of the proposed method. In all simulations, the AIM parameters (except the grid spacings), the preconditioner, and the iterative solver tolerance are the same as those described in Section 2.3. All the results in this section are obtained on the Stampede cluster using a serial implementation of the method. The viability of the proposed scheme for scattering analysis is demonstrated by analyzing the scattering from four PEC spheres located in a four-layer dielectric medium and from a half-buried UXO in a half space.

5.2.2.1 Validation

First, all the spheres have the same radius of 0.5 m and their centers are located at $(0\ \mathrm{m}, 0\ \mathrm{m}, -0.6\ \mathrm{m})$, $(0\ \mathrm{m}, 0\ \mathrm{m}, 0.6\ \mathrm{m})$, $(0\ \mathrm{m}, 0\ \mathrm{m}, 1.8\ \mathrm{m})$, and $(0\ \mathrm{m}, 0\ \mathrm{m}, 3.0\ \mathrm{m})$. The three interfaces of the four-layer dielectric medium are at $z_1 = 0$, $z_2 = 1.2\ \mathrm{m}$, and $z_3 = 2.4\ \mathrm{m}$ and the permittivity of layers are $\tilde{\varepsilon}_1^{\mathrm{t}} = 6 - j0.6$, $\tilde{\varepsilon}_2^{\mathrm{t}} = 4$, $\tilde{\varepsilon}_3^{\mathrm{t}} = 2.5 - j0.3$, and $\tilde{\varepsilon}_4^{\mathrm{t}} = 1$. The spheres are excited by a unit electric Hertzian dipole at 300 MHz. The dipole is located at $(-1\ \mathrm{m}, 0\ \mathrm{m}, 1.6\ \mathrm{m})$ and pointing in the $(\hat{\mathbf{x}} + \hat{\mathbf{y}} + \hat{\mathbf{z}}) / \sqrt{3}$ direction. The spheres surfaces are discretized using triangles with $\sim \lambda_{\min} / 6.4$ average edge length and the auxiliary grid spacing is $\sim \lambda_{\min} / 6$ in all three directions, where $\lambda_{\min}$ is the minimum wavelength in all the layers; hence, $N = 11\,064$ and $N_1^{3\mathrm{D}} = N_2^{3\mathrm{D}} = N_3^{3\mathrm{D}} = N_4^{3\mathrm{D}} = 20 \times 20 \times 18$. The 2-D auxiliary grid is chosen to be a square about $5\lambda_{\min} \times 5\lambda_{\min}$ at each interface and resulting $N_5^{2\mathrm{D}} = N_6^{2\mathrm{D}} = N_7^{2\mathrm{D}} = 31 \times 31$. The scattered electric field $\mathbf{E}_{\mathrm{x}}^{\mathrm{sca}}$ is calculated on an observation line from $(-2\ \mathrm{m}, 1\ \mathrm{m}, 0.6\ \mathrm{m})$ to $(2\ \mathrm{m}, 1\ \mathrm{m}, 0.6\ \mathrm{m})$. The results found from the proposed

extension of AIM are compared to those calculated by the MOM and another version of AIM that only employs 2-D FFTs to speedup the intra- and inter-layer interactions [51] in Fig. 5.8; the results from three methods are essentially identical. The simulation costs of two AIMs and MOM are compared in Table 5.3. As expected, the proposed AIM has a clear advantage over MOM as well as its counterpart that only uses 2-D FFTs.

Table 5.3: Computational costs of the different methods for spheres

$N = 11\,064$	Matrix fill time (s)	Memory (MB)	Matrix solve time per iteration (s)
MOM	5.48×10^5	1126	1.33
AIM (2-D FFT)	2.07×10^5	1536	2.36
AIM (Proposed)	1.67×10^4	382	0.57

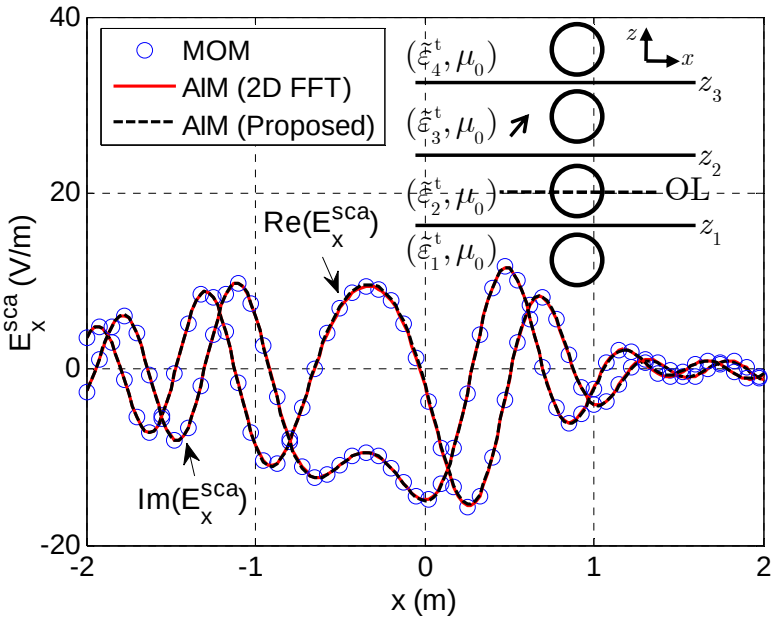

Figure 5.8: Scattering from four PEC spheres residing in four different layers. The scattered electric field is observed along the dashed line shown in the inset figure.

Next, the UXO model is the same as that in the second example of Section 5.1.5.3 except that its axis is tilted 30° with respect to the vertical axis and the UXO penetrates the interface of a two-layer dielectric medium (its top located 57.5 cm above the interface), where $\tilde{\varepsilon}_1^{\mathrm{t}} = 3.47 - j0.31$ (Yuma soil with 5% water content), $\tilde{\varepsilon}_2^{\mathrm{t}} = 1$, and the interface is at $z_1 = 0$. The UXO is excited by a 500-MHz plane wave incident from $\theta^{\mathrm{inc}} = 60^\circ$ and $\phi^{\mathrm{inc}} = 0^\circ$. The surface of the UXO is discretized using triangles with $\sim \lambda_{\min} / 10.5$ average edge length and the auxiliary grid spacing is $\sim \lambda_{\min} / 7$ in all three directions; hence, $N = 7848$, $N_1^{3\mathrm{D}} = 14 \times 21 \times 20$, and $N_2^{3\mathrm{D}} = 14 \times 20 \times 18$. The 2-D auxiliary grid is chosen to be a square about $4\lambda_{\min} \times 4\lambda_{\min}$ at each interface and resulting

$N_3^{2D} = 29 \times 28$. The RCS patterns calculated with the proposed AIM are compared to those calculated by a reference high order MOM [13] and another version of 2-D FFT AIM in Fig. 5.9. The simulation costs of two AIMs and MOM are compared in Tables 5.4 and $N^{it} = 417$. Fig. 5.9 validates the proposed AIM can also be applied to structures expanded in multiple layers.

Table 5.4: Computational costs of the different methods for half buried UXO in Yuma soil with 5% water content

7848	Matrix fill time (s)	Memory (MB)	Matrix solve time per iteration (s)
MOM	3.37×10^4	1229	0.63
AIM (2-D FFT)	9.45×10^3	390	0.55
AIM (Proposed)	1.04×10^4	296	0.35

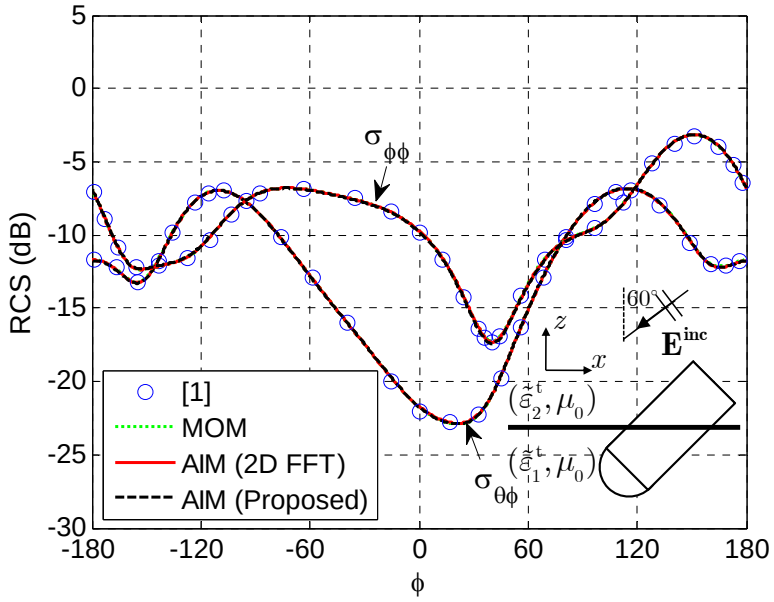

Figure 5.9: Bistatic RCS from half buried UXO residing in 5% water content Yuma soil with different water content.

5.3 SUMMARY

This Chapter presented an extension of AIM for fast analysis of scattering from 3-D structures located in multiple layers of a planar-layered medium. The proposed scheme accelerates the iterative MOM solution by employing 3-D auxiliary regular grids, each of which encloses the parts of the structure in a different layer, and 2-D auxiliary regular grids, each of which is located at a different interface of the layered medium. The auxiliary grids are used to execute the standard four-stage AIM procedure (anterpolation, propagation, interpolation, and correction) but the propagation stage of the procedure is divided into intra-layer and inter-layer components. Only the 3-D grids and both 3-D and 2-D grids are used for intra- and inter-layer propagation stages, respectively. Numerical results validated the accuracy and efficiency of the proposed method. The proposed extension of AIM is

best suited for solving type 1a, 1b, 3a, and 3b multi-scale problems in a planar-layered medium background, i.e., for single-scale structures. The combination of the AIM extension described in this Chapter and the FFT-MLIM method in Chapter IV is expected to be the most suitable method for solving type 4a and 4b multi-scale problems.

Chapter VI Complex Scattering Applications

This Chapter presents extensive numerical results to demonstrate the capabilities of the methods developed in Chapters II-V. The methods are used to solve different types of multi-scale problems encountered in geophysics, microwave-assisted material synthesis, and microstrip circuits.

6.1 GEOPHYSICAL EXPLORATION

In this section, the AIM for homogeneous and layered-medium backgrounds is employed to solve scattering problems in geophysics including remote sensing, controlled-source electromagnetic (CSEM) surveys, and well logging.

6.1.1 Remote Sensing

First, the AIM is applied to solve a type 1a multi-scale problem where the electromagnetic scattering from a large-scale underground bunker model is calculated and compared to the independent result. The bunker model is a $5\times5\times2$ m^3 rectangular box and its top is located 2.5 m below the interface of a two-layer isotropic dielectric medium, where $\tilde{\varepsilon}_1^{\mathrm{t}} = 3.3 - j0.3$, $\tilde{\varepsilon}_2^{\mathrm{t}} = 1$, and the interface is at $z_1 = 0$. The bunker is excited by a 900-MHz plane wave incident from $\theta^{\mathrm{inc}} = 60^\circ$ and $\phi^{\mathrm{inc}} = -90^\circ$. The surface of the bunker is discretized using triangles with $\sim \lambda_1 / 10.1$ average edge length and the auxiliary grid spacing is $\sim \lambda_1 / 10$ in all three directions; hence, $N = 1\,067\,850$, and $N^{\mathrm{3D}} = 240\times240\times96$. The RCS patterns calculated with the AIM are compared to those calculated with a reference fast inhomogeneous plane wave algorithm (FIPWA) accelerated MOM [99] in Fig. 6.1. All results agree well except when

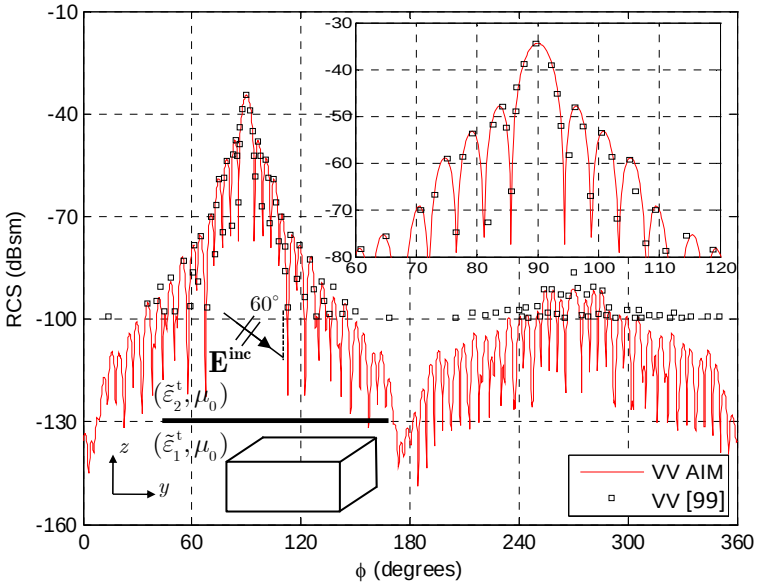

Figure 6.1: Bistatic RCS of the bunker in a two-layer medium in the $\theta = 60^{\circ}$ cut at 900 MHz. The reference results were available only down to -100 dBsm.

the RCS is less than -85dB; the difference is likely due to the fact the reference results used a less accurate iterative solution with $tol = 10^{-3}$ [99]. This simulation required $\sim 1.8 \times 10^{6}$ seconds for filling the matrices ($\sim 1.1 \times 10^{4}$ seconds for filling the tables), 72.5 GB memory, 6.8×10^{3} seconds per iteration, and $N^{\mathrm{it}} = 36$ iterations.

Next, the AIM is applied to solve a type 3a multi-scale problem where the electromagnetic scattering from a large-scale half buried UXO model is calculated and compared to the independent result. The same scattering problem as that in the second example of Section 5.2.2.1 is solved except that the UXO is now half buried in the Yuma soil with 20% water content, where $\tilde{\varepsilon}_1^{\mathrm{t}} = 21.45 - j1.92$, $\tilde{\varepsilon}_2^{\mathrm{t}} = 1$. The surface of the UXO is discretized using triangles with $\sim \lambda_{\min} / 10.5$ average edge length and the auxiliary

grid spacing is ~ $\lambda_{\min}/7$ in all three directions; hence, $N = 31\,392$, $N_1^{3D} = 25 \times 48 \times 45$, and $N_2^{3D} = 25 \times 45 \times 40$. The 2-D auxiliary grid is chosen to be a square about $9\lambda_{\min} \times 9\lambda_{\min}$ at each interface and resulting $N_3^{2D} = 66 \times 66$. The RCS patterns calculated with the proposed AIM are also compared to those calculated by a reference high order MOM [13] and another version of 2-D FFT AIM in Fig. 6.2. The simulation costs of two AIMs and MOM are compared in Table 6.1 and $N^{it} = 4592$.

Table 6.1: Computational costs of the different methods for half buried UXO in Yuma soil with 20% water content

31 392	Matrix fill time (s)	Memory (GB)	Matrix solve time per iteration (s)
MOM	5.97×10^5	18.0	11.01
AIM (2-D FFT)	9.31×10^4	4.2	8.64
AIM (Proposed)	4.80×10^4	1.3	3.21

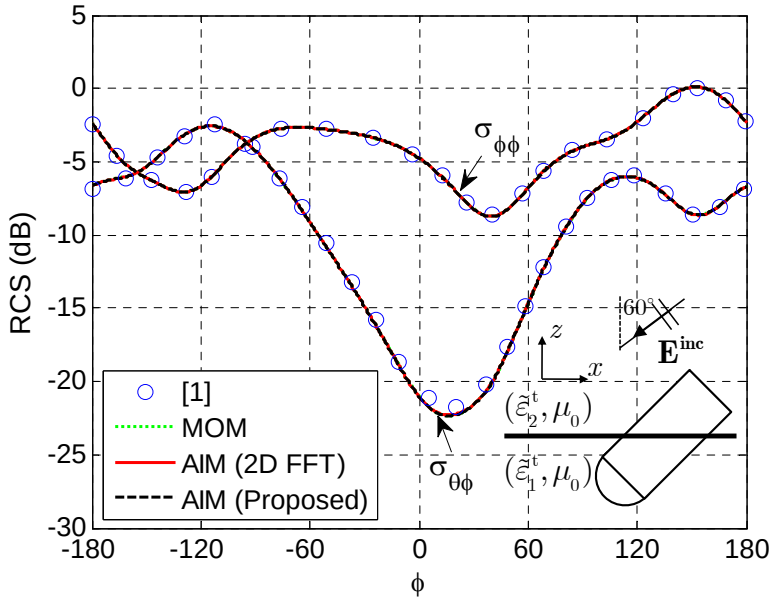

Figure 6.2: Bistatic RCS from half buried UXO residing in 20% water content Yuma soil with different water content.

6.1.2 CSEM

In this section, the capability of AIM is demonstrated by analyzing scattering for two CSEM examples (type 3a multi-scale problem): (i) An isotropic reservoir in a three-layer uniaxial medium and (ii) an anisotropic reservoir in a three-layer isotropic medium. In both cases, the results are compared to independent references that model the reservoirs as 2-D objects (infinitely long in the y direction). The finite length of the reservoirs in the below 3-D models were found by repeatedly increasing their lengths from very small values until the fields observed in the center cut showed no variation.

The isotropic reservoir is 3 km wide in x direction, 15 km long in y direction, and has a height of 0.1 km in z direction; Its permittivity and conductivity are set to $\underline{\underline{\boldsymbol{\varepsilon}}}_{\mathrm{V}} = \varepsilon_0 \underline{\underline{\mathbf{I}}}$ and $\sigma_{\mathrm{V}}^{\mathrm{xx}} = \sigma_{\mathrm{V}}^{\mathrm{yy}} = \sigma_{\mathrm{V}}^{\mathrm{zz}} = 0.01\ \mathrm{S/m}$. The background is identical to the one in

the second example in Section 5.1.5.2. The center of the reservoir is at $(x, y, z) = (3.5, 0, -1.05)$ km and the receivers are located on the sea floor at horizontal distances varying from 1 to 10 km from the transmitter in x direction. The reservoir is discretized with $N = 72\ 430$ SWG functions (average tetrahedron edge length $\sim \delta_{\min} / 8.9$) and $N^{3D} = 70 \times 320 \times 6$. The x component of the electric field calculated by the AIM is compared to the one in [1] in Fig. 6.3. Here, the iterative solver required 23 iterations to converge; the simulation required $\sim 5.99 \times 10^{5}$ seconds to fill the matrices, ~3.0 GB of memory, and $\sim 1.06 \times 10^{1}$ seconds per iteration. Fig. 6.3 shows good agreement with reference.

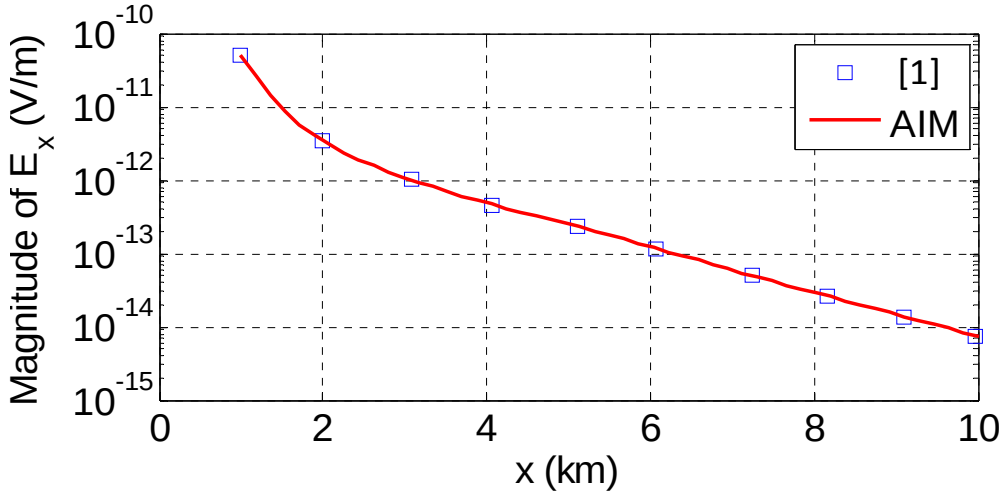

(a)

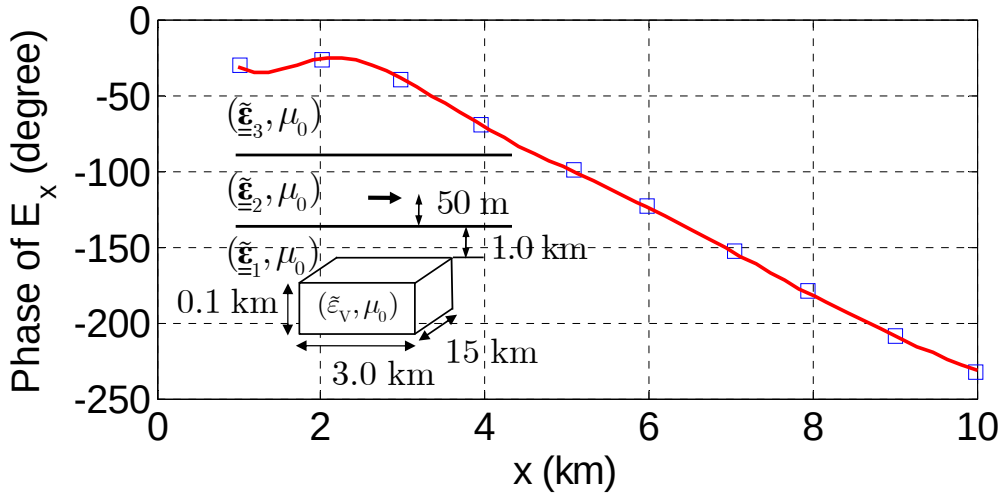

(b)

Figure 6.3: The x component of the electric field as a function of the transmitter-receiver distance. (a) Magnitude. (b) Phase.

The anisotropic reservoir is 6 km wide in x direction, 12 km long in y direction, and has a height of 0.1 km in z direction; Two anisotropy values are modeled: In the first case (R1), $\underline{\underline{\boldsymbol{\varepsilon}}}_{\mathrm{V}} = \varepsilon_0 \underline{\underline{\mathbf{I}}}$ and $\sigma_{\mathrm{V}}^{\mathrm{xx}} = \sigma_{\mathrm{V}}^{\mathrm{yy}} = 0.02\ \mathrm{S/m}$, and $\sigma_{\mathrm{V}}^{\mathrm{zz}} = 2\times10^{-3}\ \mathrm{S/m}$; in the second case (R2), $\underline{\underline{\boldsymbol{\varepsilon}}}_{\mathrm{V}} = \varepsilon_0 \underline{\underline{\mathbf{I}}}$, $\sigma_{\mathrm{V}}^{\mathrm{xx}} = \sigma_{\mathrm{V}}^{\mathrm{zz}} = 0.02\ \mathrm{S/m}$, and $\sigma_{\mathrm{V}}^{\mathrm{yy}} = 2\times10^{-3}\ \mathrm{S/m}$. The background is the same as before except the air layer is lossless and the sea-floor is isotropic, i.e., $\beta_1 = 1$. The center of the reservoir is at $(x,y,z) = (0,0,-1.05)\ \mathrm{km}$; and the receivers are located on the sea floor from $x = -10\ \mathrm{km}$ to $x = 10\ \mathrm{km}$ at $y = 0\ \mathrm{m}$. The reservoir is discretized with $N = 116\ 262$ SWG functions (average tetrahedron edge length $\sim \delta_{\min} / 9.0$) and $N^{\mathrm{3D}} = 135\times256\times6$. The x-component of the observed electric field calculated with the AIM scheme is compared to the one in [100] in Fig. 6.4. The simulation required $\sim 9.93\times10^{5}$ seconds to fill the matrices, ~4.7 GB to store the matrices, and $\sim 1.79\times10^{1}$ seconds per iteration in both cases, but the iterative solver converged in $N^{\mathrm{it}} = 81$ iterations in the first case and $N^{\mathrm{it}} = 129$ iterations in the second case; this is because of the different object anisotropy in the two cases that results in different MOM matrix entries and matrix conditioning. Fig. 6.4 shows good agreement with reference.

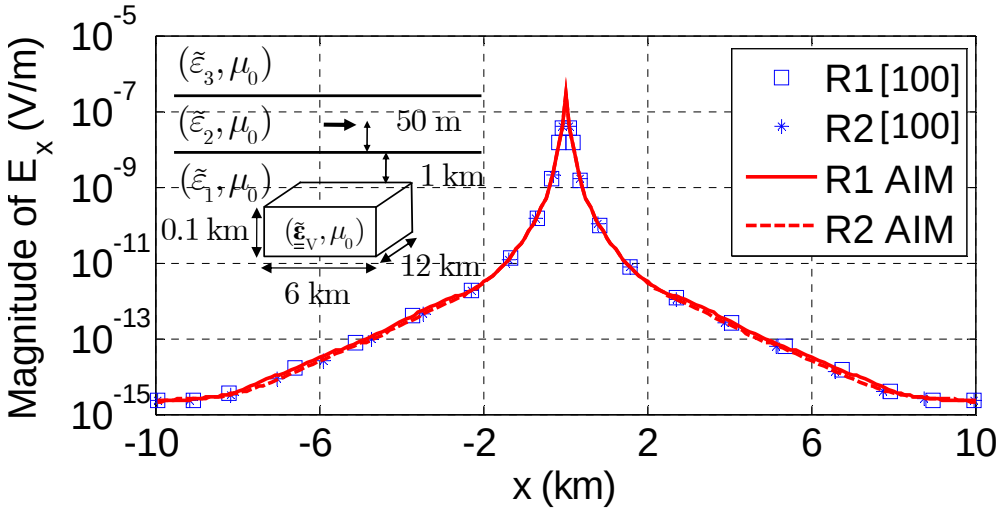

(a)

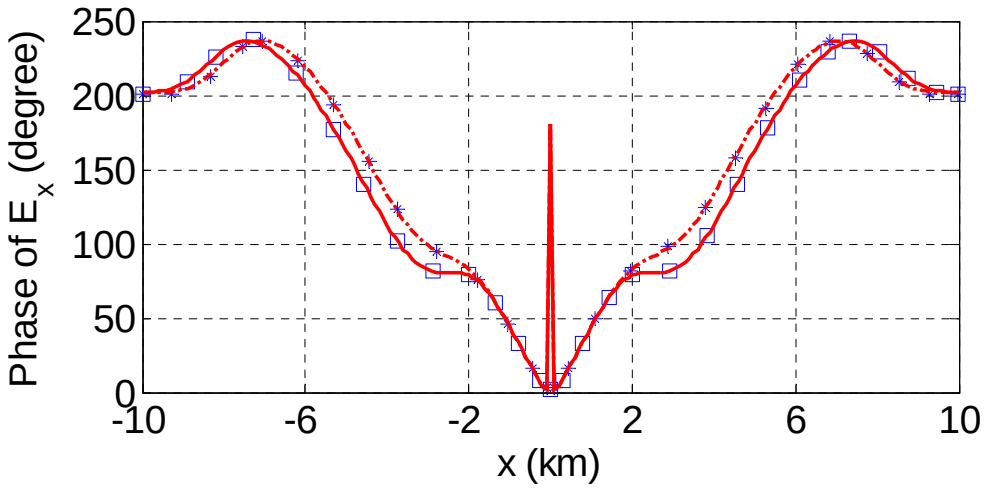

(b)

Figure 6.4: The x component of the electric field as a function of the transmitter-receiver distance. (a) Magnitude. (b) Phase.

6.1.3 Detection and Appraisal of Hydro-Fractures

Next, multi-component open-hole horizontal borehole resistivity measurements of 3-D hydro-fractures are modeled by AIM and the impact of various parameters on the detection and appraisal of the fractures are investigated.

The borehole is modeled as two 50-m long concentric cylinders. The {inner, outer} cylinder has a radius of {5.7, 10.7} cm [103],[104] and represents the {mandrel, mud} regions; the conductivities of mandrel, mud, and background are set to 10^{-4} S/m, 1 S/m, $1/3$ S/m, respectively [103],[104]. It is assumed that the fractures are filled with an electrically conductive proppant to increase their effective conductivity, denoted by σ_{eff}, which is a parameter to be investigated. All fractures are modeled as a 5-mm thick layer [103],[104] of arbitrary cross sectional area A and dip angle φ (Fig. 6.5), which are also parameters of interest. In the following, for the sake of brevity, the fracture areas are specified by including the small area where the borehole intersects the fracture, e.g., in Fig. 6.5, the area is specified as $A \sim 9\pi$ m^2 instead of $A = (9 - 2 \times 0.107^2)\pi$ m^2. In all cases, the center of the fracture intersects the borehole axis at $y = 0$, which is 35 m away from one end and 15 m away from the other end of the borehole (Fig. 6.5).

The logging tool is assumed to consist of one transmitter and two receivers located at a distance d_1 and d_2 away from the transmitter. Two types of tools are considered: $\{d_1, d_2\}$ is $\{1.2, 1.5\}$ m for the "short spacing" and $\{18, 19.2\}$ m for the "long spacing" measurements [103],[104]. In both cases, the transmitter is modeled as an arbitrarily-oriented unit impressed magnetic Hertzian dipole located on the borehole axis. In this two-receiver configuration, the contribution of the incident field to the detected

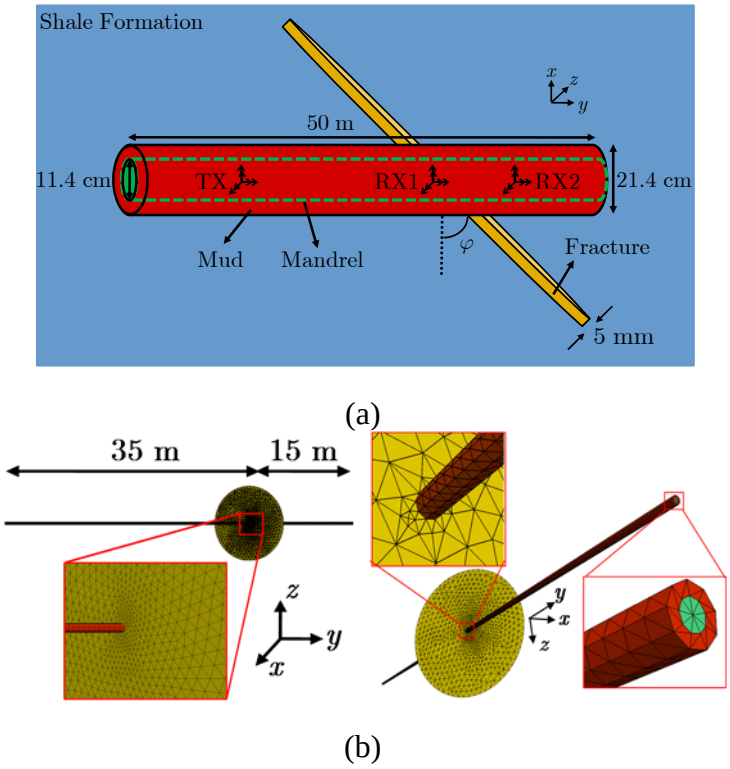

Figure 6.5: Model of an open-hole horizontal borehole resistivity measurement. (a) Mandrel, mud, and fracture dimensions. (b) Two views of the tetrahedral mesh for the circle-shaped fracture of area $A \sim 9\pi \text{ m}^2$ and dip $\varphi = 45^\circ$.

signal, which contains no information about the anomalous volume, is reduced by linearly combining the voltages detected by the two receivers [105],[106]. By modeling the receivers as identical small loops around the mandrel, this combination is expressed as

$$\Delta U^{\text{uv}} = \text{Im}\{-j\omega\mu_0 0.057^2 \pi \hat{\mathbf{u}} \cdot [\mathbf{H}^{\text{v}}(\mathbf{r}_{\text{RX2}}) - \mathbf{H}^{\text{v}}(\mathbf{r}_{\text{RX1}}) \frac{d_1^3}{d_2^3}]\} \tag{6.1.1}$$

Here, ΔU^{uv} denotes the detected signal and the superscript $\{u, v\}$ designates the {receiver, transmitter} orientation. Only the imaginary part is used as it is dominant (Fig.

2.3). To identify whether a fracture is detectable, the relative signal strength $(\Delta U^{\mathrm{uv}}_{\mathrm{frac}} - \Delta U^{\mathrm{uv}}_{\mathrm{bore}}) / \Delta U^{\mathrm{yy}}_{\mathrm{bore}}$ is used as the figure of merit; here, $\{\Delta U^{\mathrm{uv}}_{\mathrm{frac}}, \Delta U^{\mathrm{uv}}_{\mathrm{bore}}\}$ is detected by the *u*-directed receivers due to the *v*-directed source when the fracture is {present, absent} and $\Delta U^{\mathrm{yy}}_{\mathrm{bore}}$ is detected in the axially co-polarized measurements when the fracture is absent. To account for the noise and measurement uncertainties in the logging instrument, a fracture is considered detectable by the measurement only if the maximum relative signal strength $\max(|\Delta U^{\mathrm{uv}}_{\mathrm{frac}} - \Delta U^{\mathrm{uv}}_{\mathrm{bore}}|/\Delta U^{\mathrm{yy}}_{\mathrm{bore}})$ is larger than 2% and a fracture is considered differentiable from a reference one if their relative signal strengths differ by more than 2%.

In the following simulations, the tetrahedra discretizing the borehole volume have an average edge length of approximately $8\ \mathrm{cm}$; this mesh, which is limited by the borehole cross-section (Fig. 6.5(b)), gives rise to $\sim 1.1\times 10^5$ unknowns in the borehole. The fracture meshes are irregular (Fig. 6.5(b)) because the fracture thickness ($5\ \mathrm{mm}$) is much smaller than its cross-sectional dimensions, which range from $\sim 0.2\ \mathrm{m}$ to $\sim 430\ \mathrm{m}$, and because a much higher mesh density is used near the borehole compared to a few skin depths away from it: depending on the fracture size, the average edge length is in the range $\sim 0.1-0.3\ \mathrm{m}$ near the borehole and $\sim 0.5-2\ \mathrm{m}$ away from it. When the fracture is small, the mesh density on the borehole and fracture are comparable, thus, this is still a type 1b multi-scale problem. When the fracture size keeps increasing, this example becomes a type 2b multi-scale problem eventually because the mesh density on the borehole and fracture can be in multiple length scales. The FFT-MLIM, whose performance is less sensitive to the shape of the scattering volume, are expected to be more efficient than AIM when simulating the largest fractures. Nevertheless, AIM efficiency

was found to be satisfactory for the following analysis. The number of unknowns in the fractures range from $\sim 10^4$ for the smallest fracture to $\sim 3.6\times10^5$ for the largest one. The auxiliary grid spacing ranges from 0.15 m to 1.5 m; thus, N^{3D} ranges from $243\times243\times7$ to $224\times224\times315$.

6.1.3.1 Frequency and Conductivity Contrast

First, the importance of the frequency of operation and effective conductivity of the fracture are investigated. Figs. 6.6(a)-(b) and Figs. 6.7(a)-(b) present the relative signal strength as a function of the center of the receivers for the short and the long spacing measurements, respectively. Data are shown for a small and a large circular fracture; the {small, large} fracture has an area of $A\sim\{0.36\pi, 2.3\times10^4\pi\}\ \mathrm{m}^2$ and the auxiliary grid spacing was chosen as $\{0.15, 1.0\}\ \mathrm{m}$, which resulted in a total of $N\sim\{1.2\times10^5, 3.2\times10^5\}$ unknowns and $N^{3D}=\{243\times243\times12, 224\times224\times315\}$ grid point. The {small, large} circular fracture simulations required approximately $\{9.1\times10^4, 1.1\times10^5\}$ seconds for filling the matrices, {13, 34} GB of memory, and {15, 239} seconds per iteration. The number of iterations varied slightly with tool position (51 positions are simulated); on average, the iterative solver converged in {20, 22} iterations for the short and {20, 25} iterations for the long spacing tool. Fig. 6.6(c) and Fig. 6.7(c) present the maximum relative signal strength detected by the tool as a function of the fracture area.

Results are plotted for three operating frequencies in Fig. 6.6, where the effective conductivity of the fractures were set to $\sigma_{\mathrm{eff}}=\{10, 100\}\ \mathrm{S/m}$ for the {short, long} spacing measurements. A higher effective conductivity had to be used in the long-spacing

measurements to achieve signal strengths comparable to the short-spacing ones; this is because the detected signals were weakened by the larger distance the incident fields travel from the transmitter to the fracture and the scattered fields from the fracture to the receivers (for the same center position of the receivers).

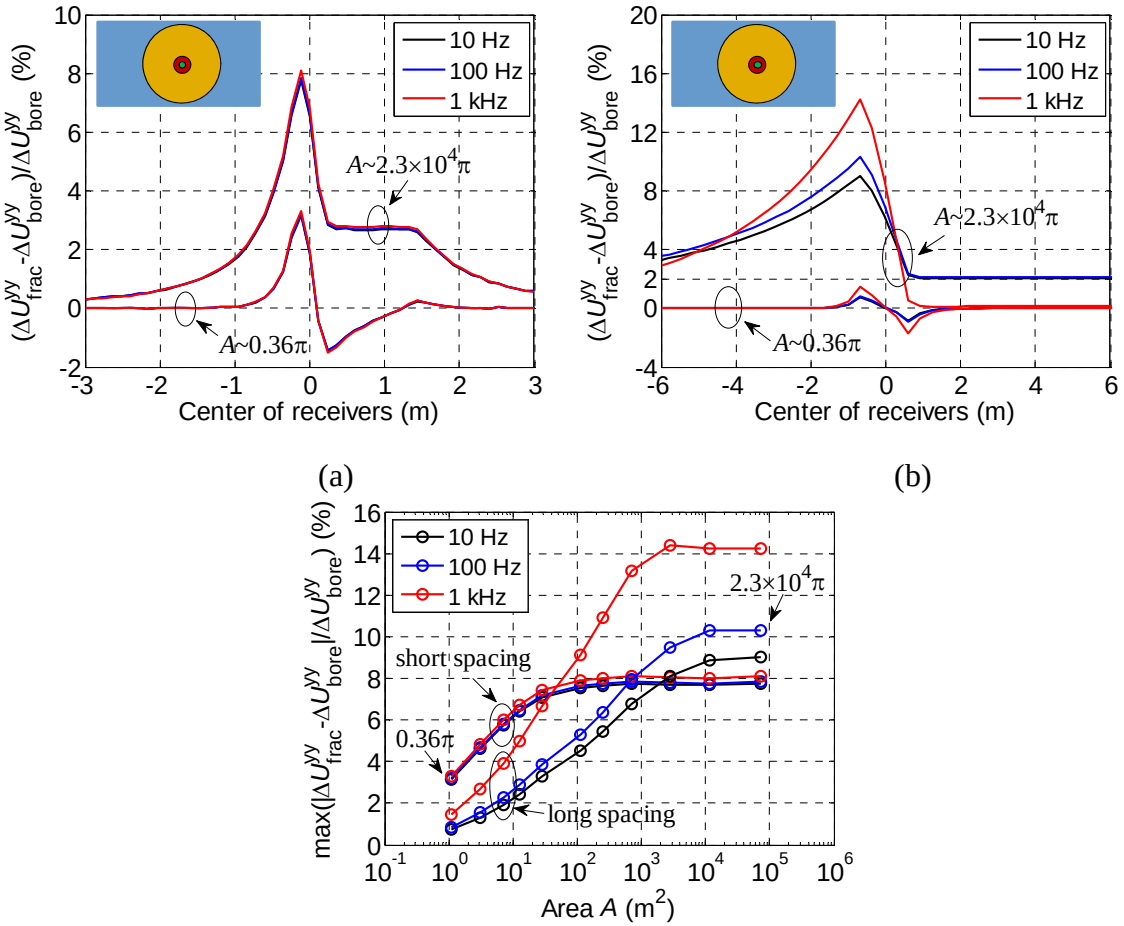

Figure 6.6: Sensitivity of borehole resistivity measurements to the operating frequency for circular fractures. (a) Short spacing measurements. (b) Long spacing measurements. (c) Peak signal detected. The effective conductivities of the fractures are set to $\{10, 100\}\ \mathrm{S/m}$ for {short, long} spacing measurements.

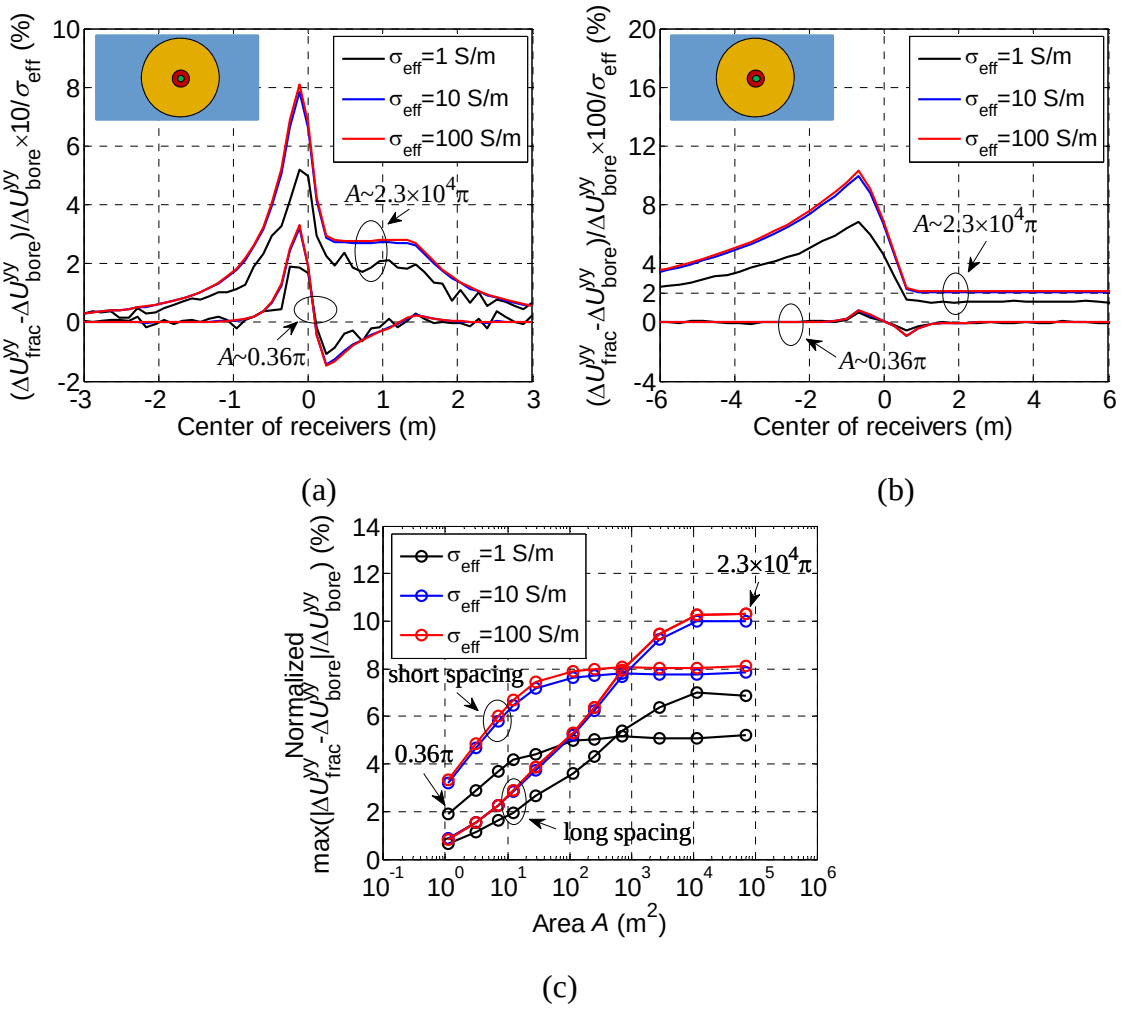

Figure 6.7: Sensitivity of borehole resistivity measurements to the fracture's effective conductivity for circular fractures. (a) Short spacing measurements. (b) Long spacing measurements. (c) Peak signal detected. The operating frequency is 100 Hz and the signals are normalized by $\{\sigma_{\text{eff}} / 10, \sigma_{\text{eff}} / 100\}$ for {short, long} spacing measurements in all three plots; although they appear comparable in the figures because of this normalization, the signals for $\sigma_{\text{eff}} = 100\ \text{S/m}$ are actually about 10 times larger than those for $\sigma_{\text{eff}} = 10\ \text{S/m}$ and the peak signal values in the short spacing measurements are actually about 8 times larger than those in the long spacing ones.

Fig. 6.6(a) shows that there are three different detection regimes as the logging tool passes through the fracture: (i) The signal becomes larger as the tool approaches the fracture and peaks when the transmitter and the first receiver is in front of the fracture and the second receiver is behind it, i.e., when the center of the receivers is close to $y = 0$. (ii) The signal becomes negative for smaller and constant for larger fractures when the transmitter is in front of the fracture and both receivers are behind it. (iii) The signal vanishes rapidly as the transmitter moves behind the fracture. The first two regimes and especially the signal spike can be used to identify the location and size of the fracture. Fig. 6.6(a) also shows that signals are larger than 2% in a wider range of tool positions for the large fracture, i.e., the tool can detect the small fracture only when the center of the receivers is at most 0.5 m ahead of the fracture but can detect the large fracture when the center is up to 1 m ahead and 1.5 m behind the fracture. Fig. 6.6(b) shows similar results (the third regime is not shown) with two key differences: the spikes in long spacing measurements are smoother and the signal is more frequency dependent. Both Figs. 6.6(a) and 6.6(b) indicate that the strength of the signal spike depends on the fracture area; this dependence is quantified in Fig. 6.6(c), where it is clear that the peak signal strength increases with fracture area and converges to a constant for both types of measurements. Fig. 6.6(c) shows that short spacing measurements can detect smaller fractures while long spacing measurements can differentiate larger fractures: Short spacing measurements can detect fractures as small as $A \sim 1\ \mathrm{m}^2$ and can distinguish fractures only until $A \sim 10\ \mathrm{m}^2$ for all three frequencies. Long spacing measurements cannot detect fractures smaller than $A \sim 10\ \mathrm{m}^2$ but can distinguish fractures until $A \sim 1000\ \mathrm{m}^2$ at 10 and 100 Hz; whereas the smallest fracture they can detect is $A \sim 1\ \mathrm{m}^2$ and the largest one they

can distinguish is $A \sim 300\ \mathrm{m}^2$ at 1 kHz. Thus, in this frequency range, the detection range is observed to be independent of the operating frequency for the short spacing measurements and depend moderately on frequency for long spacing measurements. This is because the distances between the transmitter, receivers, and fracture are very small compared to the penetration depth in the formation for the short spacing measurements; it implies that the incident field from the transmitter is frequency independent, the impedance matrix entries are proportional to the frequency, the unknown coefficients are inversely proportional to the frequency, the unknown induced current is frequency independent, and the field scattered to the receivers is frequency independent. The distances become comparable to the penetration depth in the formation for the long spacing measurements and the results begin to exhibit frequency dependence. Specifically, in the short spacing measurement, where the distance from the {transmitter, receiver} to any point on the largest fracture that can be differentiated ($A = 10\ \mathrm{m}^2$) is less than $R^{\max} \approx \{4.7, 3.6\}$ m, i.e., $\left|\gamma_{\mathrm{b}} R^{\max}\right| \approx \{0.17, 0.13\}$ at 1 kHz, where γ_{b} is the complex propagation constant; thus, all distances are small enough such that the results are frequency independent. By contrast, in the long spacing measurement, the distance from the {transmitter, receiver} to the largest fracture that can be differentiated ($A = 1000\ \mathrm{m}^2$) is less than $R^{\max} \approx \{30.4, 19\}$ m, i.e., $\left|\gamma_{\mathrm{b}} R^{\max}\right| \approx \{1.1, 0.69\}$ at 1 kHz; thus, the distances become large enough in terms of the background penetration depth that the results begin to exhibit frequency dependency.

Results are plotted for three effective conductivities in Fig. 6.7; here, the operating frequency is 100 Hz and the signals are divided by $\{\sigma_{\mathrm{eff}} / 10, \sigma_{\mathrm{eff}} / 100\}$ for {short, long} spacing measurements to show them clearly in the same plot. Fig. 6.7(a) shows that the

signals have the same shape as in Fig. 6.6(a) and that the shape is independent of σ_{eff}. Fig. 6.7(a) indicates that when $\sigma_{\text{eff}} \geq 10\ \text{S/m}$, the signal strength is proportional to the fracture's effective conductivity—note the normalization with σ_{eff}. This proportionality is because the scattered magnetic field from the fracture scales with σ_{eff} when $\sigma_{\text{eff}} \gg \sigma_{\text{b}}$. When $\sigma_{\text{eff}} = 1\ \text{S/m}$, the signal is very weak: it is within 0.5% of the borehole only case for the largest fracture. The signal is not smooth because the significant digits in the scattered magnetic field computed by the proposed method are cancelled when $\Delta U^{\text{yy}}_{\text{frac}}$ and $\Delta U^{\text{yy}}_{\text{bore}}$ are calculated; in other words, the computational errors become visible. These errors can be reduced by increasing the computational costs, e.g., by refining the borehole mesh or using high-order basis functions. Similar conclusions can be drawn from Fig. 6.7(b) for the long spacing measurements except that the signals are weaker (about 8 times at the peak) compared to the short spacing measurements—it is important to note the factor of 10 difference in scaling between Fig. 6.7(a) and Fig. 6.7(b). The cancellation when computing $\Delta U^{\text{yy}}_{\text{frac}}$ and $\Delta U^{\text{yy}}_{\text{bore}}$ is less severe for the long spacing measurement and thus the computational errors are not visible in Fig. 6.7(b) even though the signals are weaker than in Fig. 6.7(a). Fig. 6.7(c) shows that the detection range of the both measurements depends strongly on fracture's effective conductivity: For short spacing measurements, when $\sigma_{\text{eff}} = 1\ \text{S/m}$, none of the fractures are detectable; when $\sigma_{\text{eff}} = 10\ \text{S/m}$, fractures as small as $A \sim 1\ \text{m}^2$ can be detected and as large as $A \sim 10\ \text{m}^2$ can be distinguished; when $\sigma_{\text{eff}} = 100\ \text{S/m}$, the minimum detectable area is $A \sim 0.1\ \text{m}^2$ (by extrapolating data in Fig. 6.7(c)) and the maximum area that can be distinguished is as large as $A \sim 100\ \text{m}^2$. For long spacing measurements, when $\sigma_{\text{eff}} = 1$ or $10\ \text{S/m}$, none of the fractures are detectable; when $\sigma_{\text{eff}} = 100\ \text{S/m}$, fractures larger

than $A \sim 10\ \mathrm{m}^2$ can detected and fractures as large as $A \sim 1000\ \mathrm{m}^2$ can be distinguished.

To summarize: short spacing measurements can detect and distinguish circular fractures whose areas are in the range $A \sim 1-10\ \mathrm{m}^2$ at 100 Hz when $\sigma_{\text{eff}} = 10\ \mathrm{S/m}$ While increasing the frequency does not improve the results, increasing the effective conductivity of the fracture strengthens the signal and increases the range, e.g., to $A \sim 0.1-100\ \mathrm{m}^2$ for $\sigma_{\text{eff}} = 100\ \mathrm{S/m}$. In contrast, long spacing measurements can detect and distinguish larger fractures, e.g., in the range $A \sim 10-1000\ \mathrm{m}^2$ at 100 Hz when $\sigma_{\text{eff}} = 100\ \mathrm{S/m}$, but the signals are weaker. Although increasing the frequency helps somewhat to strengthen the signal for the long spacing measurements, it also reduces the maximum area that can be distinguished, e.g., the range becomes $A \sim 1-300\ \mathrm{m}^2$ at 1 kHz ($\sigma_{\text{eff}} = 100\ \mathrm{S/m}$). Based on the results in Figs. 6.6-6.7, the operating frequency is set to $100\ \mathrm{Hz}$ and σ_{eff} is set as $\{10, 100\}\ \mathrm{S/m}$ for {short, long} spacing measurements in the simulations in Sections 6.1.3.2-6.1.3.4.

6.1.3.2 Geometrical Properties: Shape

Next, the importance of the cross-section shape of the fracture is investigated. Fig. 6.8 shows the simulation results for small and large fractures with three different cross-section shapes: circle, square, and ellipse with major axis in the *x* direction and aspect ratio 8. The square and elliptical fractures in Figs. 6.8(a)-(d) have the same areas as the circular ones. The auxiliary grid spacing for the {small, large} fracture was chosen as $\{0.15, 1.0\}\ \mathrm{m}$ for the square fractures, which resulted in a total of $N \sim \{1.2\times10^5,\ 3.1\times10^5\}$ unknowns and $N^{3\mathrm{D}} = \{243\times243\times12,\ 196\times196\times280\}$

grid points; it was chosen as $\{0.15, 1.5\}$ m for the elliptical fracture, which resulted in $N \sim \{1.2\times10^5, 4.3\times10^5\}$ unknowns and $N^{3D} = \{243\times243\times7, 420\times420\times75\}$ grid points. As a result, matrix fill time, memory requirement, time per iteration, and average numbers of iteration for the square and elliptical fractures were comparable to those of the circular fracture of the same area. Figs. 6.8(e)-(f) describe the maximum relative signal strength as a function of the areas of the different shaped fractures.

Figs. 6.8(a), 6.8(c), and 6.8(e) show that the area rather than the cross-section shape of the fractures determines the signals in the axially co-polarized (*yy*-oriented) measurements; indeed, the signals for the axially symmetric (circle/square) fractures are practically identical if their areas are the same and differ less than 2% from the signals for the axially asymmetric (ellipse) fracture. This is because the fields induced in the fractures near the borehole (the strongest fields) are similar for all fracture shapes. Clearly, axially co-polarized measurements cannot distinguish the fracture shape at any size.

Figs. 6.8(b), 6.8(d), and 6.8(f) show that the signals in the transverse co-polarized (*xx*-oriented) measurements are also determined by the area but are more sensitive to the shape of the fracture. Fig. 6.8(b) shows that the signals in the *xx*-oriented short spacing measurements have similar shapes but are mostly negative and have larger magnitude compared to the signals in the *yy*-oriented short spacing measurements of Fig. 6.8(a). Fig. 6.8(d) shows that the signals in the long spacing measurements are much stronger (about 7 times at the peak) and have sharper peaks in the *xx*-orientation compared to those in the *yy*-orientation in Fig. 6.8(c). Fig. 6.8(f) shows that the transverse co-polarized measurements cannot discern axially symmetric fractures but can distinguish axially symmetric fractures from asymmetric ones up to a certain fracture size. The {short, long} spacing

measurements can distinguish axial asymmetry in the range $A \sim \{1-10, 1-1000\}\ \mathrm{m}^2$ —note the factor of 10 scaling for the long spacing measurements in Fig. 6.8(f).

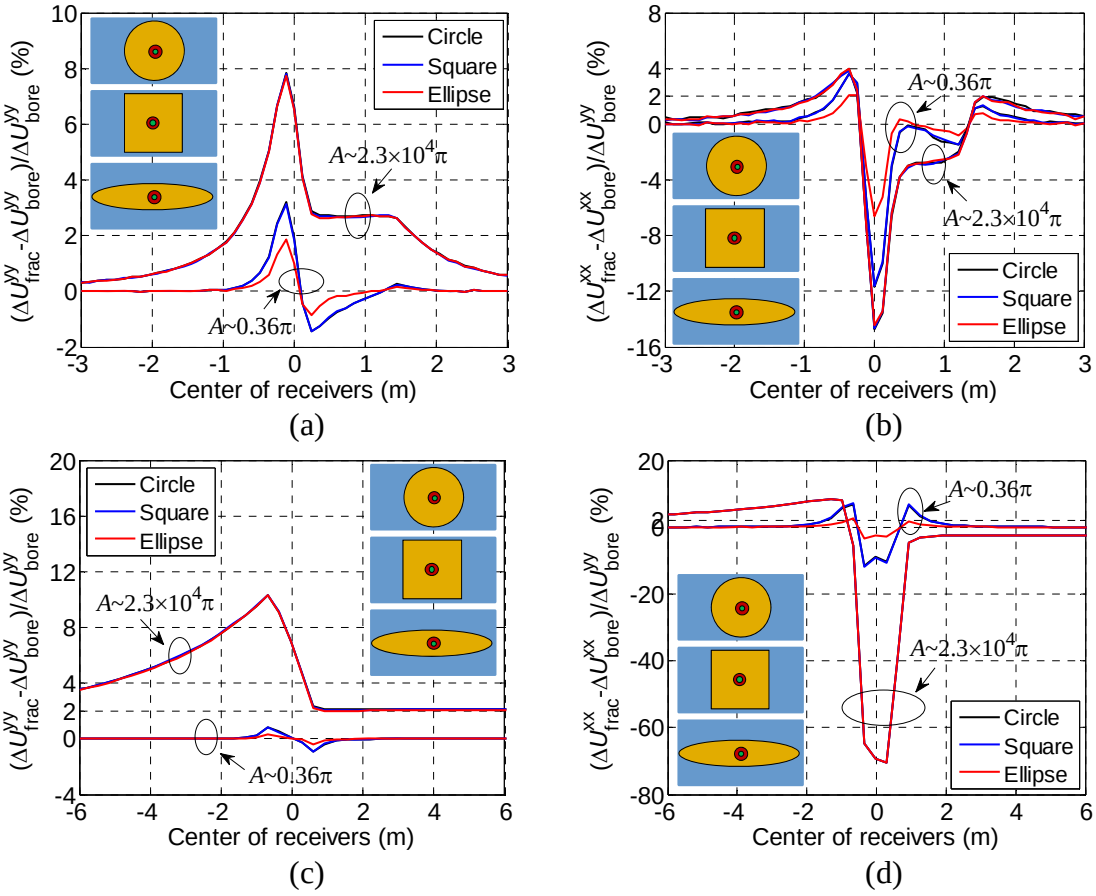

Figure 6.8: Sensitivity of co-polarized borehole resistivity measurements to fracture shape at 100 Hz. Left column: *yy*-oriented measurements. Right column: *xx*-oriented measurements. Top row: Short spacing measurements. Middle row: Long spacing measurements. Bottom row: Peak signal detected. The effective conductivities of the fractures are set to $\{10, 100\}\ \mathrm{S/m}$ for {short, long} spacing measurements.

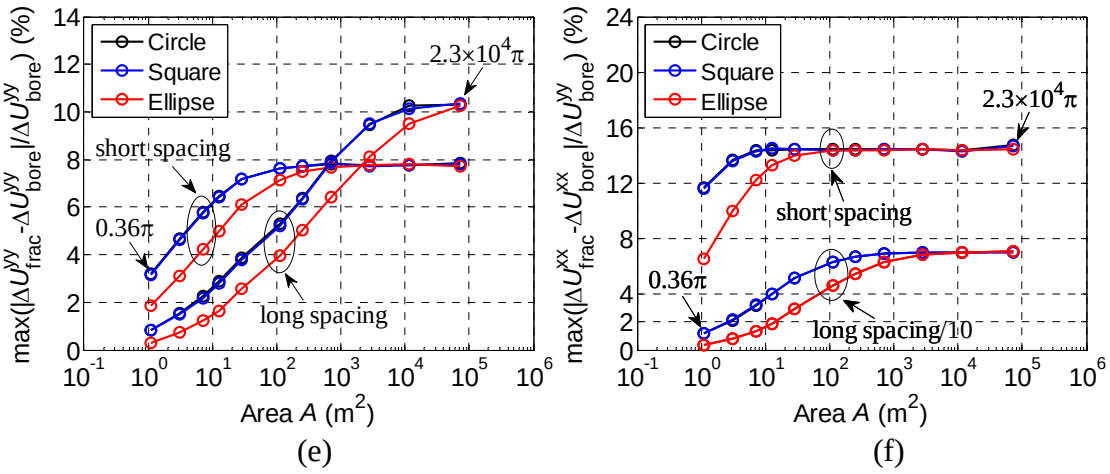

Figure 6.8: Continued.

To summarize: Co-polarized measurements, whether they are oriented parallel or transverse to the borehole axis, cannot differentiate axially symmetric fractures from each other. The transverse co-polarized measurements can discern axially asymmetric fractures from symmetric ones, e.g., the {short, long} spacing measurements can distinguish elliptical fractures with aspect ratio of 8 from axially symmetric fractures if their areas are in the range $A \sim \{1-10, 1-1000\}\ \mathrm{m}^2$.

6.1.3.3 Geometrical Properties: Dip

Next, the effects of the fracture dip are investigated. Fig. 6.9 describes the simulation results for a small and a large circular fracture with three different dips ($0^\circ, 15^\circ, 60^\circ$) in the xoy plane; fractures with different dips in Figs. 6.9(a)-(d) have the same areas as those in Section 6.1.3.1. Because the fractures get closer to the borehole as dip angle increases, a larger number of elements was used as φ increased. This resulted

in slightly larger N (up to 1.3 times) for the same area fracture when it is tilted and also led to more non-zero entries in $\mathbf{Z}^{\text{corr}}$; thus, tilted fractures required up to approximately 2-3 times larger matrix fill time and memory space. The time per iteration and the average numbers of iteration were comparable to those of the untilted fractures. Figs. 6.9(e)-(f) describes the maximum relative signal strength as a function of the fracture area.

Figs. 6.9(a) and 6.9(c) show that the signals in the axially co-polarized (*yy*-oriented) measurements become weaker when the dip angle increases. This behavior is correlated to the projection of the tilted fracture onto the xoz plane, which also becomes smaller as the dip angle increases. Moreover, the shape of signals for the small dip angle is similar to those for the untilted fractures, but the shape changes for the larger dip angle. Fig. 6.9(e) shows that the detection range for the 15° dipping fractures is essentially the same as that for the untilted fractures whereas the 60° dipping fractures {short, long} spacing measurements can only detect fractures larger than $A \sim \{10, 1000\}\ \mathrm{m}^2$ and not distinguish them from larger fractures. Moreover, the short and long spacing measurements cannot discern untilted fractures from 15° tilted ones but can differentiate them from 60° tilted fractures whenever they can detect them.

Figs. 6.9(b) and 6.9(d) show that the signals in the cross-polarized (*xy*-oriented) measurements for dipping fractures also have three different regimes as the logging tool passes through the fracture but the third regime is more complicated as the signals do not vanish monotonically. Fig. 6.9(b) shows that the detected signals in the short spacing measurements depend on dip angle: They are almost zero for untilted fractures and have stronger spikes as the angle increases. Fig. 6.9(d) shows similar signals for the long spacing measurements (the third regime is not shown) except the spikes are smoother. Fig. 6.9(f)

indicates that the detection range of cross-polarized measurements increases with the dip angle: When $\varphi = 15^\circ$, the {short, long} spacing measurements can detect fractures larger than $A \sim \{10, 100\}\ \mathrm{m}^2$ but not distinguish them from bigger fractures; when $\varphi = 60^\circ$, they can detect fractures larger than $A \sim \{1, 100\}\ \mathrm{m}^2$ and distinguish them until $A \sim \{10, 1000\}\ \mathrm{m}^2$. By comparing the first row of Fig. 6.9 to the second row, it becomes clear that *xy*-oriented measurements are more sensitive to dip angle in the xoz plane compared to co-polarized measurements; this behavior is because the *x*-directed magnetic field is strongly correlated to the projected area of the fracture on the yoz plane and because the incident field does not include the cross component. Similarly, *zy*-oriented measurements can be used to detect the dip angle of the fractures in the yoz plane.

To summarize: Axially co-polarized measurements are rather insensitive to the dipping angle: They can be used to detect fractures with large dip angles but cannot distinguish the areas of dipping fractures. Cross-polarized measurements can detect the dip with respect to the borehole axis whether the fracture is small or large. The larger the dip angle, the more sensitive the cross-polarized measurements, e.g., {short, long} spacing measurements can detect 15° dipping fractures that are larger than $A \sim \{10, 100\}\ \mathrm{m}^2$ but cannot distinguish them, while the same measurements can detect and distinguish 60° dipping fractures in the range $A \sim \{1-10, 100-1000\}\ \mathrm{m}^2$. Therefore, cross-polarized measurements are more suitable to assess fracture dip.

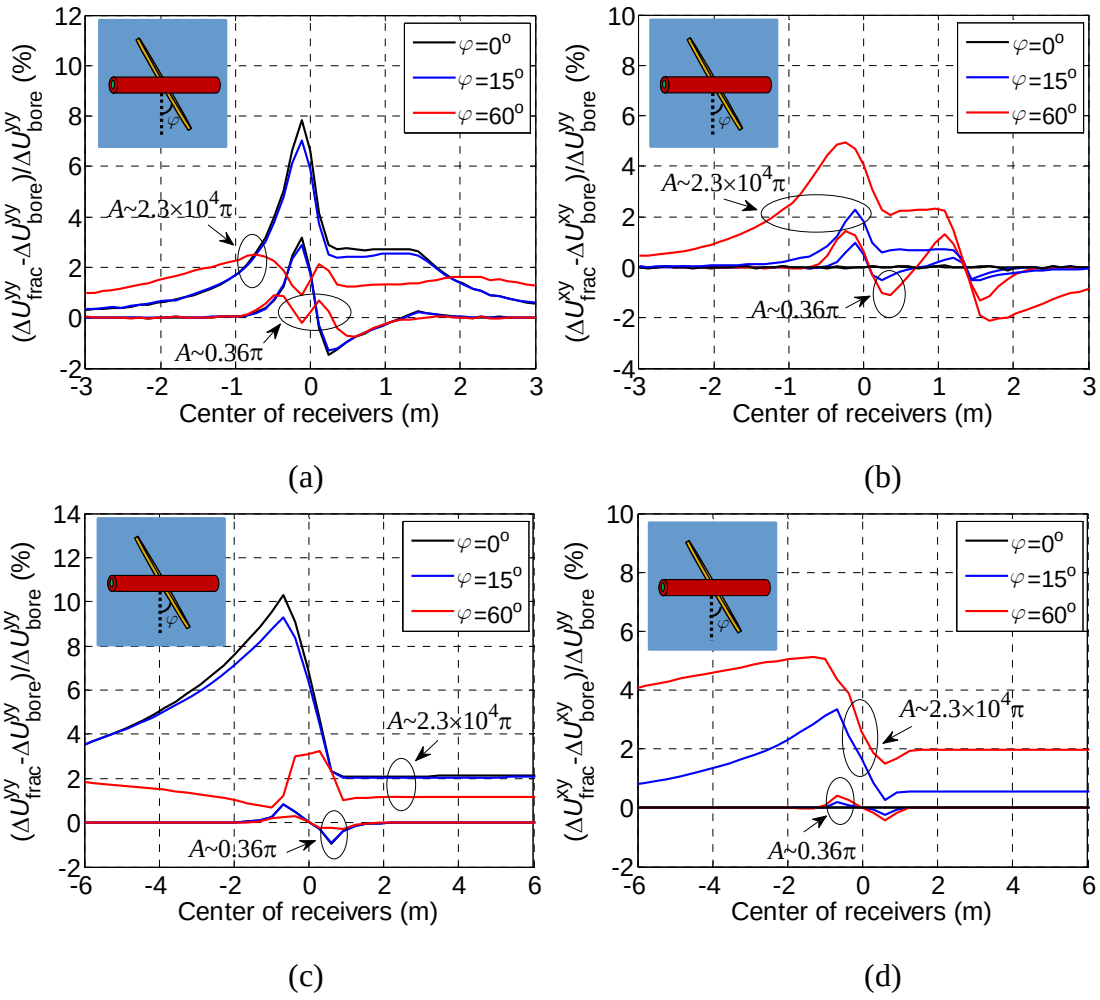

Figure 6.9: Sensitivity of co-polarized borehole resistivity measurements to the dip of circular fractures at 100 Hz. Left column: *yy*-oriented measurements. Right column: *xx*-oriented measurements. Top row: Short spacing measurements. Middle row: Long spacing measurements. Bottom row: Peak signal detected. The effective conductivities of the fractures are set to $\{10, 100\}$ S/m for {short, long} spacing measurements.

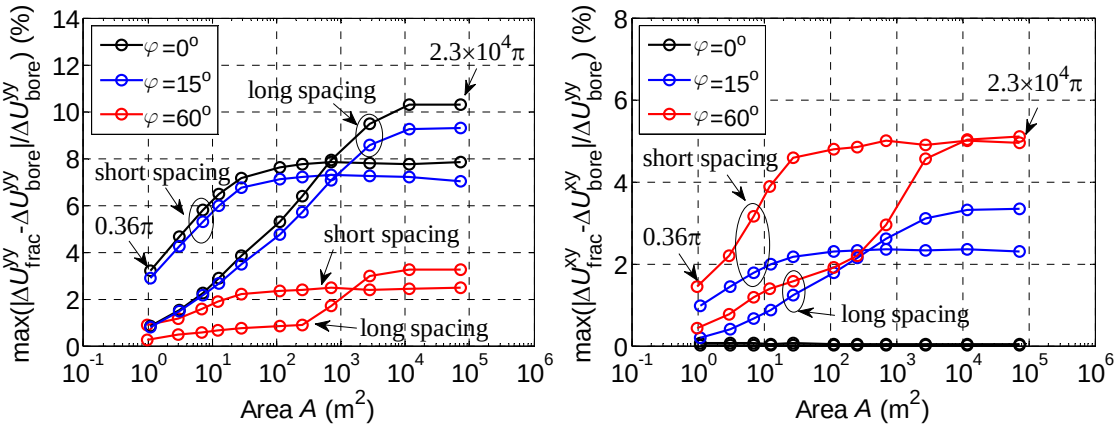

(e) (f)

Figure 6.9: Continued.

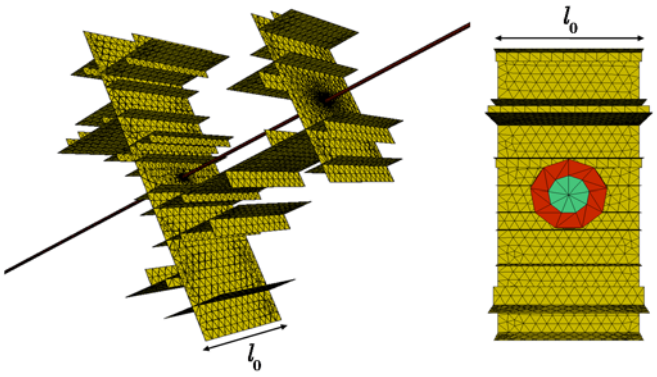

(a)

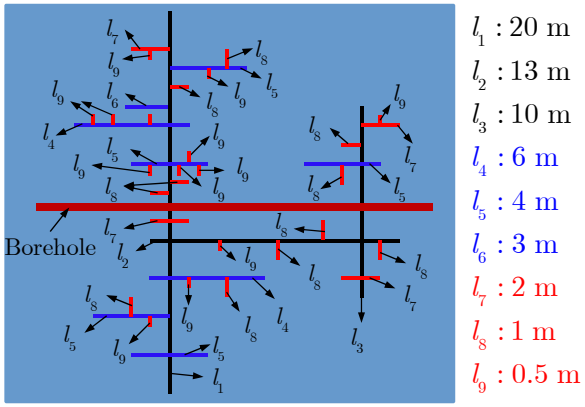

(b)

Figure 6.10: 3-D net-shaped hydro-fracture. (a) Different views of the tetrahedral mesh. (b) Side view of the geometry drawn to scale (major branches: black; intermediate branches: blue; minor branches: red).

6.1.3.4 Complex Hydro-Fracture Network

Finally, borehole resistivity measurements are used to appraise a complicated hydro-fracture network (Fig. 6.10). The branches in the network, which are all 5 mm thick, are separated into three groups based on their length: major branches are longer than or equal to 10 m, intermediate branches are shorter than 10 m but longer than 2 m, and minor

branches are shorter than or equal to 2 m (Fig. 6.10(b)). In the following, three cases are simulated: Only major branches of the fracture are modeled in case 1. Major and intermediate branches are modeled in case 2. All the branches are modeled in case 3. Unlike in Sections 6.1.3.1-6.1.3.3, the fracture area is increased by modifying not two but only one dimension, the depth of the fracture l; as a result, even the main branches are axially asymmetric and the area of the fractures in the side view in Fig. 6.10(b) are fixed to 0.215 m^2 (case 1), 0.39 m^2 (case 2), and 0.5175 m^2 (case 3) in all simulations.

Figs. 6.11(a)-(b) describe the simulation results for a {small, large} fracture depth of $l_0 = \{1.4, 122\}\ \mathrm{m}$. For these fractures, the auxiliary grid spacing was chosen as $\{0.2, 0.6\}\ \mathrm{m}$, which resulted in a total of $N \sim \{1.3\times10^4, 4.7\times10^5\}$ unknowns and $N^{3D} = \{189\times189\times105, 168\times168\times40\}$ for the fractures in case 3. Fractures in the remaining two cases have slightly smaller N but the same N^{3D}. The {small, large} fracture simulations required approximately $\{1.3\times10^5, 5.1\times10^5\}$ seconds for filling the matrices, {19, 105} GB of memory, and {51.6, 112.2} seconds per iteration for the fractures in case 3; these computational costs were similar for cases 1 and 2. Here, 101 tool positions were simulated to appraise the position and size of the fractures; on average, the iterative solver converged in {30, 55} for the short and {34, 75} iterations for the long spacing measurements in case 3. Average numbers of iteration were {25, 30} for the short and {25, 35} for the long spacing measurements in case 1 and {25, 28} for the short and {27, 36} for the long spacing measurements in case 2. Fig. 6.11(c) describes the maximum relative signal strength as a function of the network depth.

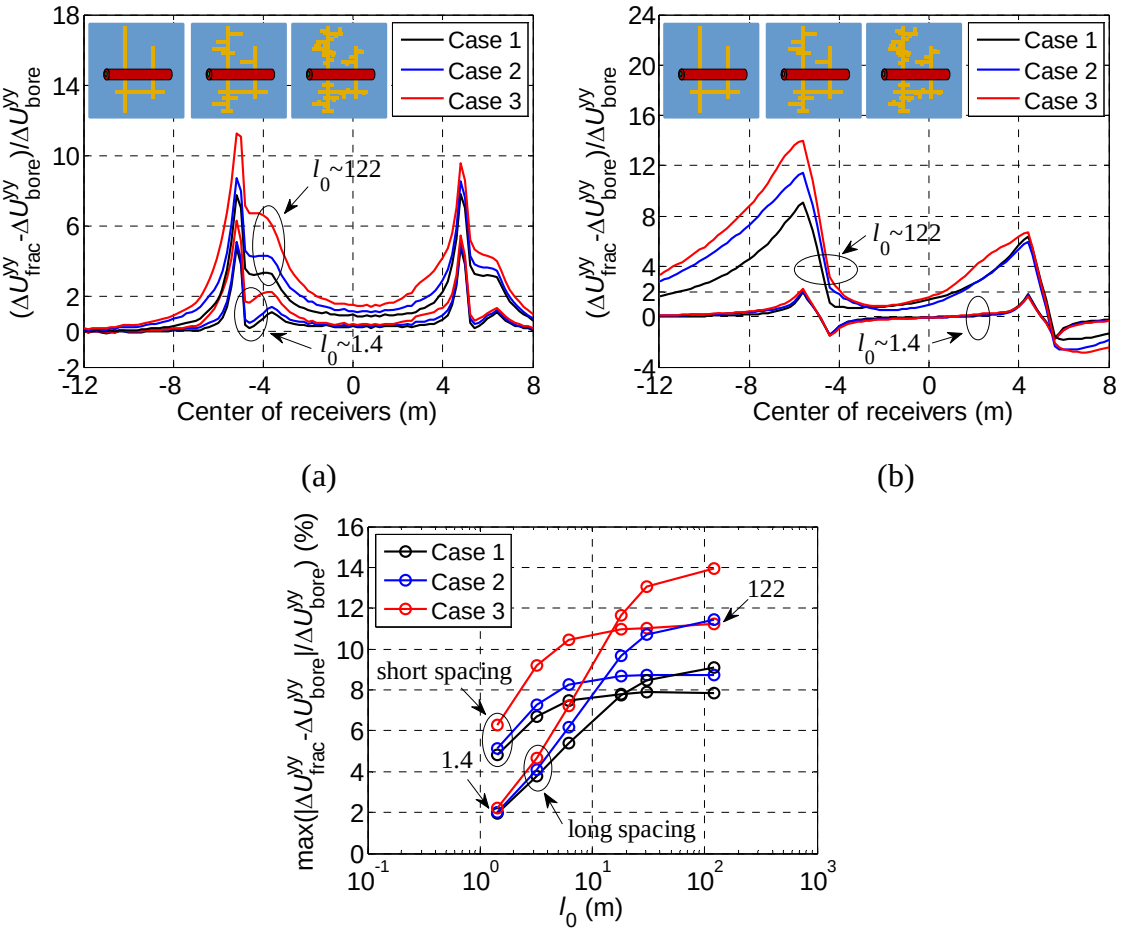

Figure 6.11: Sensitivity of borehole resistivity measurements to the different branches of a fracture network at 100 Hz. (a) Short spacing measurements. (b) Long spacing measurements. (c) Peak signal detected. The effective conductivities of the fractures are set to $\{10, 100\}$ S/m for {short, long} spacing measurements.

Fig. 6.11 indicates that borehole resistivity measurements can be used to detect and appraise complex fracture networks. Figs. 6.11(a)-(b) show that there are two spikes in the

measurements because of the two large branches perpendicular to the borehole and the shape of each spike is similar to those in Figs. 6.6-6.9. The width of the spike is narrower for the short spacing measurements ($\sim 1\ \mathrm{m}$) than that for the long spacing ones ($\sim 4\ \mathrm{m}$), i.e., short spacing measurements have a higher resolution; thus, they can differentiate fractures closer to each other compared to long spacing measurements. The different signals observed for the different cases indicate that the major, intermediate, and minor branches all contribute to the shape and magnitude of the signals; the contribution mainly depends on the area and position of the branch. Fig. 6.11(c) shows that the peak signal strength increases with fracture depth and converges to a constant for all three cases and both types of measurements. The {short, long} spacing measurements can detect the fracture network if it is deeper than $l_0 \sim \{1,1\}\ \mathrm{m}$ and can distinguish depths until $l_0 \sim \{3,10\}\ \mathrm{m}$.

Based on the above observations, the most effective approach for detecting and appraising 3-D hydraulic fractures with low-frequency borehole resistivity measurements is as follows: First, the short or long spacing cross-polarized component should be employed to quantify fracture dip with respect to the borehole axis, i.e., the orientation of fracture should be identified. Next, the number and the position of large fracture branches intersecting the borehole should be identified with shorter spacing measurements (either the axially co-polarized or cross-polarized component based on the fracture dip). Finally, longer spacing measurements should be used to assess the fracture area and shape. Higher effective conductivity is always preferred for enhancing the sensitivity of borehole resistivity measurements.

6.1.4 Summary

This section demonstrated the applicability of the AIM schemes for homogeneous and planar-layered medium backgrounds to type 1a, 1b, 2b, and 3a multi-scale problems in various geophysical applications including remote sensing, controlled-source electromagnetic (CSEM) surveys, and well logging.

6.2 MICROWAVE-ASSISTED THIN FILM GROWTH

In this section, the AIM for rectangular-cavity background is employed to model a microwave-assisted thin film growth experiment. In the experiment, an indium tin oxide (ITO) coated glass substrate is immersed in a liquid solution contained in a quartz vessel. The quartz vessel is placed on a rotor that is located in a microwave oven and heated. A computer model of the experiment is developed, the electromagnetic scattering analysis is performed using the AIM scheme to find the field distribution throughout the model, and the energy absorbed by the different parts in the model is extracted.

6.2.1 Electromagnetic Model

The electromagnetic model of the experimental setup is shown in Fig. 6.12. Here, the microwave oven is modeled as a rectangular cavity with PEC walls. The cavity and simulation frequency are the same as those in Section 3.6.2. The rotor (blue region in Fig. 6.12(a)), parts of which were observed to be made of metal (polytetrafluoroethylene-coated aluminum), is modeled as a PEC surface. The quartz vessel (green region in Fig. 6.12(a)) and the glass substrate (not shown in Fig. 6.12(a)) are modeled as lossless dielectric volumes with relative permittivity of 4 and 6, respectively. The liquid solution (orange region in Fig. 6.12(a)) is modeled as a lossy dielectric volume with relative permittivity of

12.5 and conductivity of $0.16\ \mathrm{S/m}$. The ITO layer (dark red square in Fig. 6.12(a)) is modeled as an infinitesimally thin dielectric sheet because its thickness is $150\ \mathrm{nm}$, relative permittivity is 4, and conductivity is $\sim 7.5 \times 10^5\ \mathrm{S/m}$ (the field penetration depth is $\sim 11.7\ \mu\mathrm{m}$ at 2.45 GHz). The geometrical description of the model is as follows: The rotor is centered in the middle of the cavity at $(22.5\ \mathrm{cm}, 21\ \mathrm{cm}, 16\ \mathrm{cm})$; it is 24.8 cm high; its top and bottom surfaces are formed of two concentric circles with 19.4 cm inner and 39.4 cm outer diameters; its 8 vertical metal rods are uniformly spaced identical cylinders of 0.9 cm diameter; and the distance from the center of a rod to the one diametrically on the opposite side is 29.2 cm. The 1-cm thick quartz vessel is formed of two concentric cylinders that have 2.54 cm inner diameter and 4.54 cm outer diameter; its outer cylinder is 18.5 cm high and is centered at $(22.5\ \mathrm{cm}, 6.4\ \mathrm{cm}, 14.15\ \mathrm{cm})$ while its inner cylinder is 17.5 cm high and is centered 0.5 cm higher. The liquid solution is a 7 cm high cylinder centered at $(22.5\ \mathrm{cm}, 6.4\ \mathrm{cm}, 9.4\ \mathrm{cm})$ and its diameter is 2.54 cm. The glass substrate is a parallelepiped of size $1.3\ \mathrm{cm} \times 1.1\ \mathrm{mm} \times 1.3\ \mathrm{cm}$ that is centered at $(22.5\ \mathrm{cm}, 6.4\ \mathrm{cm}, 8.55\ \mathrm{cm})$. The ITO layer is a rectangular surface of size $0.8\ \mathrm{cm} \times 0.8\ \mathrm{cm}$ that is centered at $(22.5\ \mathrm{cm}, 6.345\ \mathrm{cm}, 8.55\ \mathrm{cm})$. The positions described here are for one specific location of the vessel in the cavity (the one shown in Fig. 6.12(a)); because the structure rotates in the cavity over time, other orientations are also simulated in the following; the positions of the structures for the different orientations are found by rotating all parts of the model around the center of the cavity.

The current on ITO is expanded in terms of RWG functions and the impedance boundary condition is enforced [4]. Consequently, each SWG function that is defined over a pair of tetrahedra whose common face is on the ITO layer have to be modified to be two

SWG functions defined on a single tetrahedron; this is necessary to allow the discontinuity of normal component of the (conduction-current corrected) flux density across the interface due to the existence of infinitesimally thin ITO layer. The PEC junctions on the rotor (Fig. 6.12(b)) are treated in the same way as in [83],[84]. The average edge lengths of surface and volume elements are 5.3 mm (close to $\lambda_{\text{cav}} / 23$) and 2.8 mm (about $\lambda_{\text{cav}} / 44$), which result in $N^{\text{S}} = 21\,003$ RWG functions and $N^{\text{V}} = 77\,469$ SWG functions, respectively (Fig. 6.12(b)). In this scenario, the surface and volume meshes are not single-scale meshes as the mesh density varies significantly in the different parts of the model: The mesh close to/on the ITO layer is over-resolved to 0.19 mm (nearly $\lambda_{\text{cav}} / 650$) to capture the fast field variation, especially close to the edge of ITO layer arising from the edge condition [4],[85], while the rest of triangles and tetrahedral in the mesh have average edge lengths that are around one tenth of either the wavelength inside dielectric volume or λ_{cav}. The significant variation of mesh density leads to a type 2b multi-scale problem. The auxiliary grid spacing is 2.0 mm (around $\lambda_{\text{cav}} / 60$), $N^{\text{3D}} = 200 \times 200 \times 126$, and $\gamma = 3$.

The precise excitation of the microwave oven was unknown (only the frequency of operation and TE excitation mode were known) [4]; here, different excitations are investigated to identify which excitation best models the experimental setup. As shown in [86], the excitation of a cavity at a non-resonant frequency can be expanded as a summation of weighted cavity modes using modal decomposition. Because the weighting function decays fast (inversely proportional to the difference between the square of the resonant frequency and the square of the operating frequency [86]), the modes whose resonant frequencies are close to the operating frequency dominate the excitation. In the following, the incident field is chosen as a unit amplitude $\text{TE}_{\text{x}}(3,4,4)$, $\text{TE}_{\text{y}}(3,4,4)$, or

$\mathrm{TE}_{\mathrm{x}}(5,5,0)$ mode because the $\mathrm{TE}_{\mathrm{x}}(3,4,4)$ and $\mathrm{TE}_{\mathrm{y}}(3,4,4)$ modes have the closest resonant frequency ($\approx 2.445\ \mathrm{GHz}$) to the operating frequency of 2.45 GHz and $\mathrm{TE}_{\mathrm{x}}(5,5,0)$ has the next closest resonant frequency ($\approx 2.443\ \mathrm{GHz}$).

Once the electromagnetic scattering are solved for various positions of the rotor, the microwave energy absorbed at various positions in the cavity must be extracted, *i.e.*, the integral

$$e(\mathbf{r}) = \int_0^T [\omega\varepsilon''(\mathbf{r}_t) + \sigma(\mathbf{r}_t)]\,\mathrm{Re}[\mathbf{E}(\mathbf{r}_t)e^{j\omega t}]\cdot \mathrm{Re}[\mathbf{E}(\mathbf{r}_t)e^{j\omega t}]dt\ \ (\mathrm{Joule/m^3}) \qquad (6.2.1)$$

must be calculated, where $e(\mathbf{r})$ denotes the absorbed energy density per one rotation of the rotor, $\mathbf{r}$ is the position of interest on the ITO layer in time-invariant local coordinates (with respect to the substrate corner for example), and $\mathbf{r}_t$ is the position in time-varying global coordinates (with respect to the cavity corner for example) at time t. This integral must be carefully evaluated because the rotation period of the rotor is $T = 20\ \mathrm{s}$ while the period of the electric fields is $2\pi/\omega \sim 40.8\ \mathrm{ns}$. Here, it is calculated by dividing the integration interval into Q sub-intervals and approximating the energy absorbed in each sub-interval as the duration of the sub-interval multiplied by the average rate of energy (power) absorbed at the center of that sub-interval:

$$\begin{aligned} e(\mathbf{r}) &= \sum_{q=1}^{Q} \int_{t^{q-1}}^{t^q} [\omega\varepsilon''(\mathbf{r}_t) + \sigma(\mathbf{r}_t)]\,\mathrm{Re}[\mathbf{E}(\mathbf{r}_t)e^{j\omega t}]\cdot \mathrm{Re}[\mathbf{E}(\mathbf{r}_t)e^{j\omega t}]dt \\ &\approx \sum_{q=1}^{Q} (t^q - t^{q-1}) P^{\mathrm{avg}}(\mathbf{r}_{(t^q + t^{q-1})/2}) \end{aligned} \qquad (6.2.2)$$

Here

$$P^{\mathrm{avg}}(\mathbf{r}_t) = \frac{1}{2}[\omega\varepsilon''(\mathbf{r}_t) + \sigma(\mathbf{r}_t)]\left|\mathbf{E}(\mathbf{r}_t)\right|^2\ \ (\mathrm{Watt/m^3}) \qquad (6.2.3)$$

is the absorbed power density at position $\mathbf{r}_t$ averaged over one period of the fields. It is accurate to use the average power density to estimate the integral in (6.2.2) only under two conditions: (i) The time interval $t^q - t^{q-1}$ is large enough compared to the period of the fields $2\pi / \omega$ because the energy absorbed from the time-harmonic fields over a given interval is within $\pm\pi / \omega P^{\text{avg}}$ of the value $(t^q - t^{q-1})P^{\text{avg}}$ and (ii) The time interval $t^q - t^{q-1}$ is small enough that the rotor movement does not cause significant change in the field distribution and the energy absorption. The results in this section were obtained by setting $Q=8$ (2.5s intervals or 45° angles of the rotor) as shown in Fig. 6.12(c).

The normalized energy densities (dB scale) absorbed by the ITO layer per one rotation of the rotor due to different excitations are shown in Figs. 6.12(e)-(g) and compared to the experimental result in Fig. 6.12(d). The bright white area in Fig. 6.12(d) is the titanium dioxide (TiO_2) thin film grown on the transparent ITO substrate due to microwave heating. The thicker film close to the edges indicates more energy is absorbed by ITO near the edges. Figs. 6.12(e)-(g) show that the $\text{TE}_{\text{x}}(3,4,4)$ excitation leads to edge effects on all four edges with a smooth transition region; $\text{TE}_{\text{y}}(3,4,4)$ excitation also results in edge effects on all four edges, but the transition region is narrower, especially on the top edge; and the $\text{TE}_{\text{x}}(5,5,0)$ excitation only produces edge effects on the left and right edges. While the experimental result deviates from those obtained by using the last two excitations, it agrees well with that obtained by using the first excitation. As a result, the $\text{TE}_{\text{x}}(3,4,4)$ mode is employed as the excitation to predict the energy density absorbed by the different shapes and conductivities of ITO layer and the thin film growth in further experiments in this microwave oven. Here, the AIM simulation for each rotor

position typically required about 6.7×10^5 seconds for filling the matrices, 70 GB of memory, 2.1×10^2 seconds per iteration, and $13\,000$ iterations—the large number of iterations is caused by the dense surface mesh required to capture the fast field variation on the ITO substrate. This scenario could not be simulated with MOM because it required too much time and memory.

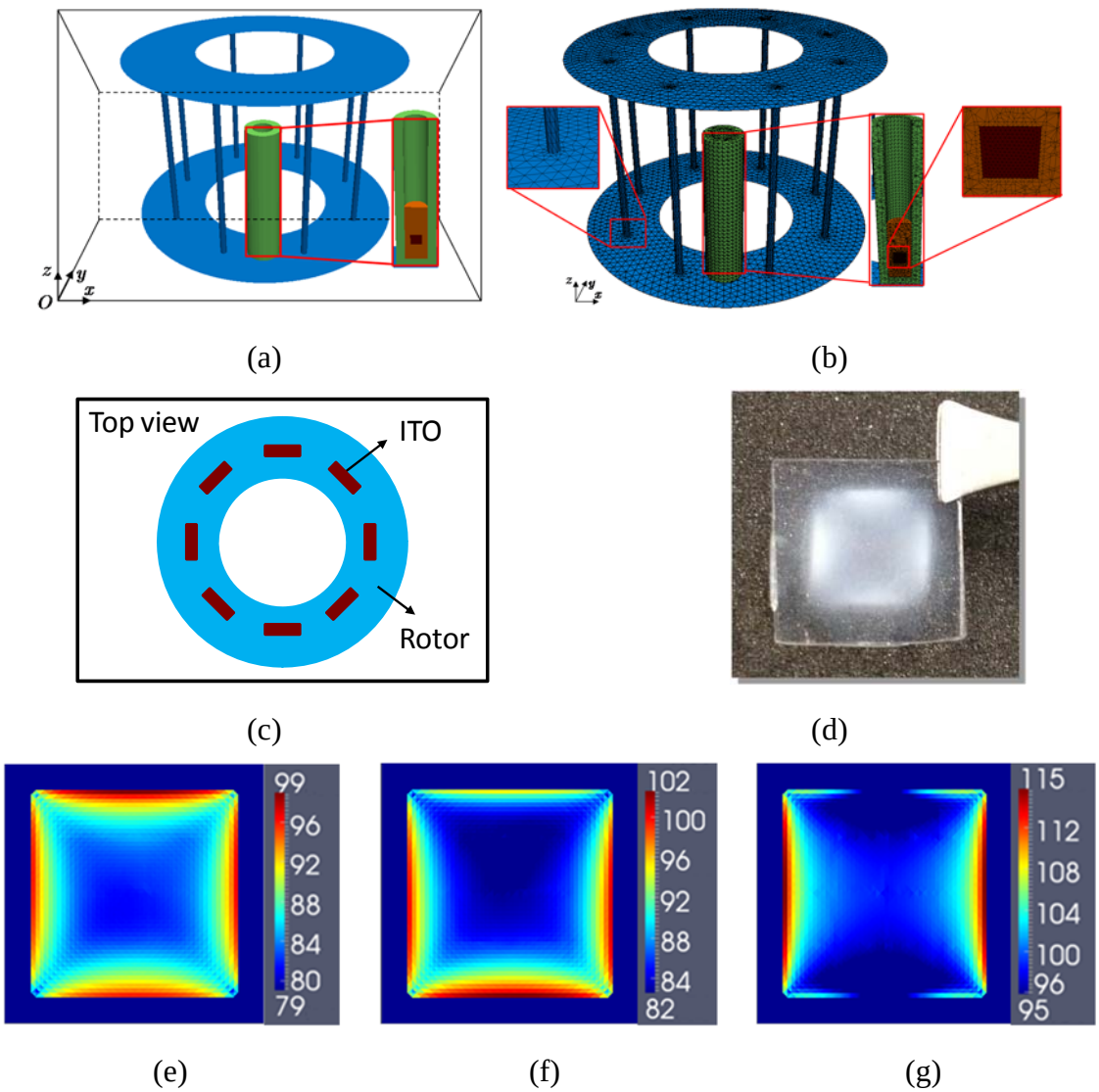

Figure 6.12: Microwave-assisted thin film growth. (a) Computational model of the experimental setup. (b) Surface and volume mesh. (c) Eight positions for calculating the absorbed energy density. (d) Experimental result showing thin film growth is focused at the edges. Computed absorbed energy density on the ITO layer per one rotation in the oven due to (e) $\mathrm{TE}_{x}(3,4,4)$ excitation, (f) $\mathrm{TE}_{y}(3,4,4)$ excitation, and (g) $\mathrm{TE}_{x}(5,5,0)$ excitation. The absorbed energy density is normalized by 1 J/m^3 and the color bars are in dB scale.

6.2.2 Thin Film Growth for Different Shapes of ITO Layer

Next, the electromagnetic simulations are further employed to predict the thin-films growth for four different shaped ITO layers (square, triangle, circle, and 2×2 square arrays). Fig. 6.13 shows the comparisons between the experimental data and simulated normalized energy densities (dB scale) for different shapes of the ITO layer. The simulated data (Figs. 6.13(i)-(l)) show that the electromagnetic energy absorption is concentrated at the edges of the ITO resulting in thicker TiO_2 films in these regions, irrespective of the ITO pattern shape. The experimentally observed edge patterns resulting from the concentration of the TiO_2 films at the ITO edges (Figs. 6.13(e)-(h)) show strong correlation to the simulations.

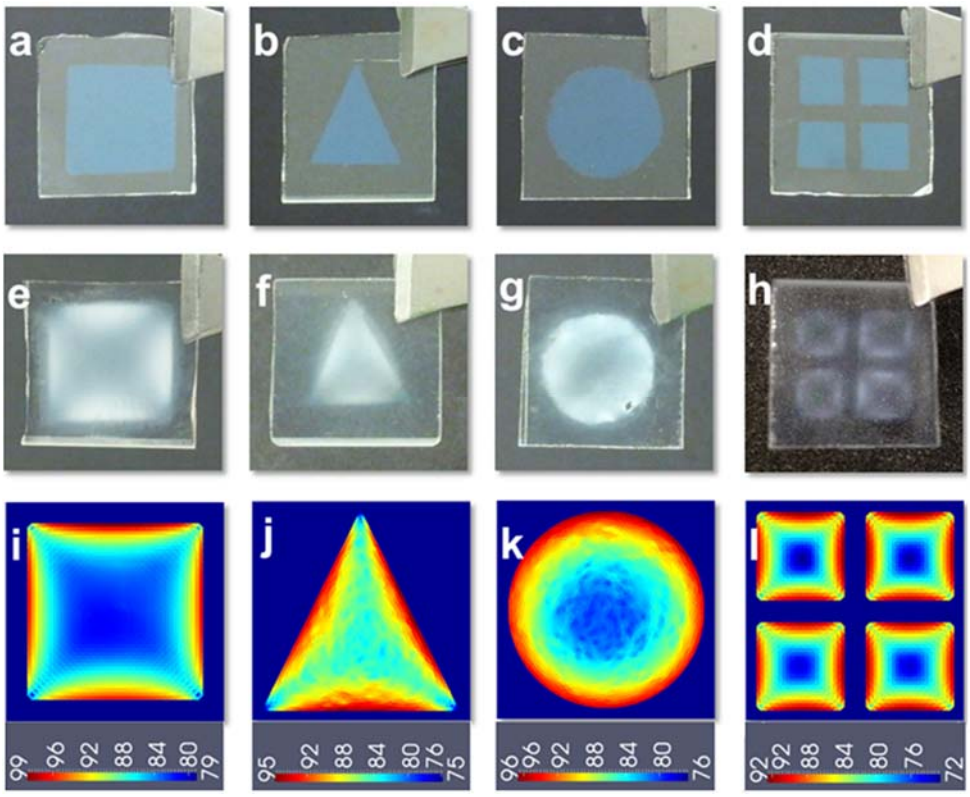

Figure 6.13: Microwave-assisted thin film growth for different shapes of ITO layer. (a)-(d) ITO layer before microwave heating. (e)-(h) ITO layer after microwave heating. (i)-(l) Computed absorbed energy density on the ITO layer per one rotation in the oven due to $\mathrm{TE}_{x}(3,4,4)$ excitation. The absorbed energy density is normalized by 1 J/m^3 and the color bars are in dB scale.

6.2.3 Uniformity Improvement of Thin Film

Finally, the electromagnetic simulations are employed to improve the uniformity of thin-film by varying the conductivity and size of the ITO layer (Fig. 6.14). As seen in Fig. 6.14(a), the total microwave energy absorbed by the ITO layer first increases as the conductivity increases, until a point is reached where the trend reverses. This is because, as σ increases, more energy is reflected rather than absorbed by the conducting layer, i.e., the electric field magnitude ($|\mathbf{E}|$) decreases in the ITO layer while σ increases and hence the absorbed energy density e, which is the time integral of $\sigma |\mathbf{E}|^2$, and the total absorbed energy by the conducting layer decreases. Thus, there exists a range of σ values where energy absorption is maximized and, therefore, would be ideal for film growth. The experiments show that while films did not grow on insulators like glass, they grow well on ITO, which has a reasonably high conductivity $(\sigma \sim 10^5\ \mathrm{S/m})$. Conversely, if conductivity is too high such as for an aluminum substrate $(\sigma \sim 10^7\ \mathrm{S/m})$, the microwave-grown films are more weakly adhered. The electromagnetic simulations further indicate that at lower conductivity, the films tend to be more uniform compared to those at higher conductivity (insets in Fig. 6.14(a)). Based on the computational predictions that lower ITO conductivity can improve film uniformity, TiO_2 films were also grown on lower conductivity $(\sigma \sim 10^3\ \mathrm{S/m})$ ITO, and the film uniformity was found to be greatly improved (Fig. 6.14(c)) in agreement with the simulations. In addition, electromagnetic simulations indicate that decreasing the size of ITO layer can also improve film uniformity (Fig. 6.14(d)-(f)).

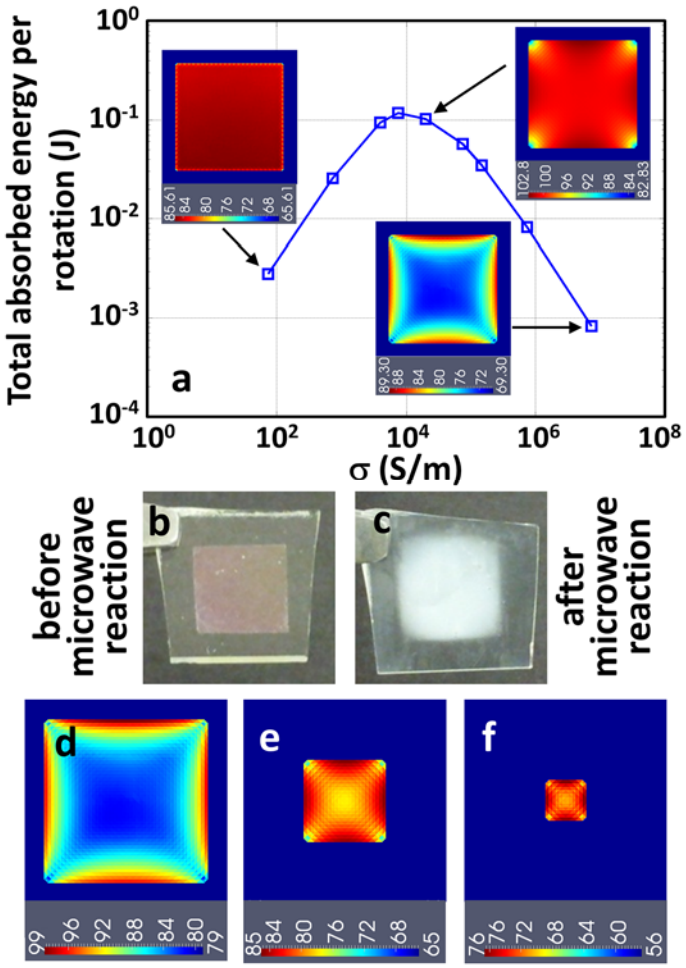

Figure 6.14: Effects of ITO layer conductivity and size on the total absorbed microwave energy and on absorption patterns. (a) Total microwave energy absorbed by the ITO layer per rotor rotation as the layer conductivity is changed with local absorption patterns (insets). Lower conductivity $(\sigma \sim 10^3\ \mathrm{S/m})$ ITO-coated glass substrate (b) before microwave reaction and (c) after microwave reaction. Films grown on lower conductivity ITO layers do not exhibit edge patterns and are more uniform than those shown in Fig. 6.13. Absorbed energy density per rotor rotation for ITO layer pattern sizes of (d) $0.8 \times 0.8\ \mathrm{cm}^2$, (e) $0.4 \times 0.4\ \mathrm{cm}^2$, and (f) $0.2 \times 0.2\ \mathrm{cm}^2$. The energy densities are normalized by 1 J/m3 and the color bars are in dB scale.

6.2.4 Summary

This section demonstrated the applicability of the AIM scheme for rectangular-cavity background to type 2b multi-scale problems in the prediction of microwave-assisted thin film growth. The AIM scheme is able to tackle multi-scale structure but becomes less efficient as the structure involves more length scales. The hybridization of the FFT-MLIM and rectangular-cavity Green functions can potentially be a more efficient alternative for analyzing microwave-assisted thin film growth.

6.3 MICROSTRIP CIRCUITS

Lastly, scattering from a 8×4 corporate-fed microstrip array [107], whose geometry is described in Fig. 6.15(a), is analyzed (a type 3b multi-scale problem). The substrate thickness is 1.59 mm and the relative permittivity is $\tilde{\varepsilon}_1^{\mathrm{t}} = 2.2$. The microstrip array is excited by a 2.5 GHz plane wave incident from $\theta^{\mathrm{inc}} = 60^\circ$ and $\phi^{\mathrm{inc}} = 0^\circ$. The surface of the microstrip array is discretized using triangles with $\sim \lambda_1 / 60.5$ average edge length and the auxiliary grid spacing is $\sim \lambda_1 / 20$ in all three directions; hence, $N = 9241$ and $N^{\mathrm{3D}} = 96 \times 96 \times 2$. The RCS pattern calculated with the AIM is compared to those calculated with MOM and a reference fast multipole algorithm (FMA) accelerated MOM [107] in Fig. 6.15(b). All results agree well. The AIM (MOM) simulation required $\sim 2.5 \times 10^3$ ($\sim 5.7 \times 10^4$) seconds to fill the matrices, ~155 MB (~1638 MB) to store the matrices, and $\sim 1.1 \times 10^{-1}$ (~ 1.3) seconds per iteration to solve the matrix equation, and the iterative solver converged in 482 (482) iterations. The number of unknown is moderate, but the reduction in computational costs is evident for the microstrip array.

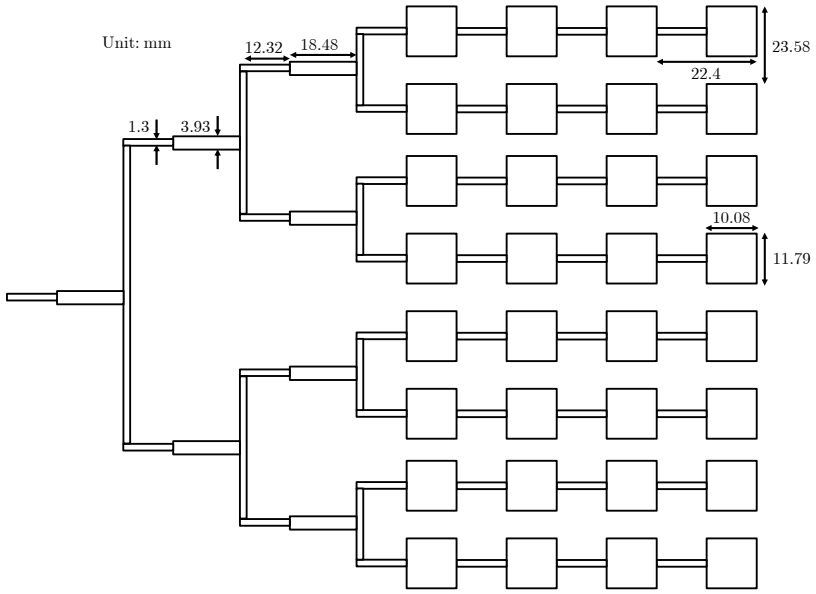

(a)

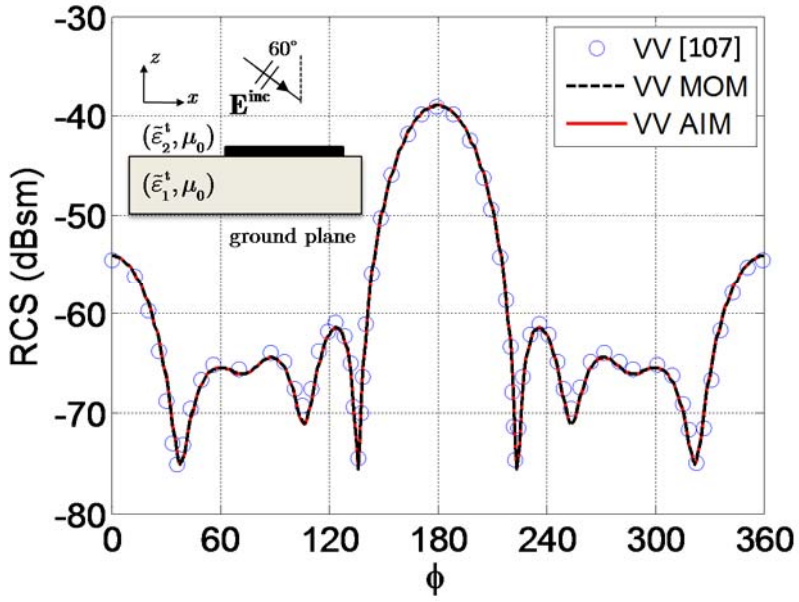

(b)

Figure 6.15: Scattering from the corporate-fed microstrip array. (a) Top view of the geometry. (b) VV-polarized bistatic RCS in the $\theta = 60^\circ$ cut at 2.5 GHz.

Chapter VII Conclusion and Future Work

This dissertation presented novel FFT and multigrid accelerated frequency-domain integral equation solvers for multi-scale electromagnetic analysis in complex backgrounds and demonstrated the benefits of the proposed methods for various applications (Table 7.1).

Table 7.1: Proposed methods for solving multi-scale problems and their applications

Problem Type	Simulation Regime	Proposed Solution Method	Sample Applications
Type 1 (Two-scale)	a. High frequency	AIM	Scattering from dielectric slab (Section 4.2.2) and underground PEC bunker (Section 6.1.1)
	b. Low frequency	AIM	Borehole resistivity measurements (Section 2.3.2)
Type 2 (Multi-scale structure)	b. Low frequency	AIM or MLIM	Borehole resistivity measurements of 3-D hydro-fractures (Section 6.1.3)
	c. Mixed frequency	AIM or FFT-MLIM	Scattering from plate array (Section 4.2.1) Microwave-assisted thin film growth (Section 6.2)
Type 3 (Multi-scale background)	a. High frequency	AIM	CSEM measurements (Section 6.1.2)
	b. Low frequency	AIM	Scattering from microstrip array (Section 6.3)
Type 4 (Multi-scale squared)	b. Low frequency	AIM or MLIM	Future work
	c. Mixed frequency	AIM or FFT-MLIM	Future work

Extended AIM schemes were proposed to solve type 1 and 3 multi-scale problems that involve single-scale structures in complex backgrounds. The AIM scheme was presented first for electrically large anisotropic dielectric structures in a homogeneous background (Chapter II). Then, it was extended to more complex scenarios where the structures reside in rectangular cavities and planar-layered media. As demonstrated in Chapters III and V, the computation time and memory requirement of the proposed extensions for these complex backgrounds are comparable to the requirements of AIM for the same structures in homogeneous backgrounds. A variety of complex applications—including remote sensing, CSEM surveys, detection of hydro-fractures with borehole resistivity measurements, microwave-assisted thin film growth, and microstrop circuits—were presented to validate the accuracy and efficiency of the proposed schemes and to demonstrate their generality, practicality, and usefulness for complex electromagnetic engineering problems. The AIM scheme and its extensions are most effective for single-scale structures. Though the methods can also be applied to multi-scale structures, in general, their efficiency should be expected to decrease as the number of length-scales in the analysis increases and the methods should eventually cease to be useful for type 2 and 4 multi-scale problems. This thesis showed, however, that the efficiency of AIM for multi-scale structures can be greatly improved by tuning its grid spacing and that AIM and its extensions remain effective schemes for many practical type 2 and 4 multi-scale problems. For those rare problems where extreme multi-scale structures exist, FFT-MLIM, an FFT-accelerated oct-tree based algorithm, was proposed as an alternative to solve type 2 and 4 multi-scale problems. It was shown that FFT-MLIM is less sensitive to the shape of the scattering structure.

This dissertation opens various potential research avenues that include the following: (i) The FFT-MLIM in Chapter IV and the AIM extension for structures residing in multiple layers of planar-layered media in Section 5.2 can be parallelized to enhance their capabilities to solve larger and more complex multi-scale problems. The efficient parallelization of FFT-MLIM is not trivial because of the oct-tree structure of this algorithm [108]. Special parallelization schemes similar to those in [109] should be devised to enhance the parallel efficiency of the algorithm by minimizing the communications and balancing the workload among the processors. Efficient parallelization of the FFT-based algorithm in Section 5.2 is complicated by the presence of multiple 2-D and 3-D auxiliary grids with varying sizes. (ii) As discussed in Chapter I, the surface electric field integral-equation suffers from the low-frequency breakdown when RWG edge length is four or five orders of magnitude smaller than the wavelength in the background medium. In order to enable the fast simulation of surface integral-equation based type 1b and 4b multi-scale problems often encountered in analyzing high-density integrated circuits, alternative basis/testing functions [25]-[31] should be incorporated into the proposed FFT and multigrid accelerated integral equation solvers. (iii) More complex type 4 multi-scale problems can be solved by extending FFT-MLIM to rectangular-cavity and layered-medium backgrounds.

References

[1] D. Pardo, M. J. Nam, C. T. Verdin, M. G. Hoversten, and I. Garay, "Simulation of marine controlled source electromagnetic measurements using a parallel fourier hp-finite element method," *Compu. Geosci.*, vol. 15, no. 1, pp. 53-67, July 2010.

[2] T. Ueda and M. S. Zhdanov, "Fast numerical methods for marine controlled-source electromagnetic (EM) survey data based on multigrid quasi-linear approximation and iterative EM migration," *Exploration Geophysics*, vol. 39, no. 1, pp. 30-37, Mar. 2008.

[3] F. Gutierrez, K. Parrish, and T. S. Rappaport, "On-Chip Integrated Antenna Structures in CMOS for 60 GHz WPAN Systems," *IEEE J. Select. Areas Commun.*, vol. 27, no. 8, pp. 1367-1378, Oct. 2009.

[4] B. Reeja-Jayan, K. L. Harrison, K. Yang, C.-L. Wang, A. E. Yılmaz, and A. Manthiram, "Microwave-assisted low-temperature growth of thin films in solution," *Sci. Rep.*, vol. 2, 1003, 2012.

[5] J. T. Oden, T. Belytschko, J. Fish, T. Hughes, C. Johnson, D. Keyes, A. Laub, L. Petzold, D. Srolovitz, S. Yip and J. Bass, "Simulation-based engineering science: Revolutionizing engineering science through simulation," Blue Ribbon Panel on Simulation-Based Engineering Science, Report of the National Science Foundation, May 2006.

[6] N. Geng, A. Sullivan, and L. Carin, "Multilevel fast-multipole algorithm for scattering from conducting targets above or embedded in a lossy half space," *IEEE Trans. Geosci. Remote Sens.*, vol. 38, no. 4, pp. 1561-2608, July 2000.

[7] H. Bagcı, F. P. Andriulli, F. Vipiana, G. Vecchi, and E. Michielssen, "A well-conditioned integral-equation formulation for efficient transient analysis of electrically small microelectronic devices," *IEEE Trans. Adv. Pack.*, vol. 33, no. 2, pp. 468–480, May 2010.

[8] F. P. Andriulli, F. Vipiana, and G. Vecchi, "Hierarchical bases for nonhierarchic 3-D triangular meshes," *IEEE Trans. Antennas Propagat.*, vol. 56, no. 8, pp. 2288–2297, Aug. 2008.

[9] F. Vipiana, M. A. Francavilla, and G. Vecchi, "EFIE modeling of high-definition multi-scale structures," *IEEE Trans. Antennas Propagat.*, vol. 58, no. 7, pp. 2362–2374, July 2010.

[10] J. S. Zhao, W. C. Chew, C. C. Lu, E. Michielssen, and J. M. Song, "Thin-stratified medium fast-multipole algorithm for solving microstrip structures," *IEEE Trans. Microw. Theory Tech.*, vol. 46, no. 4, pp. 395–403, Apr. 1998.

[11] M. S. Zhadanov, S. K. Lee, and K. Yoshioka, "Integral equation method for 3D modeling of electromagnetic fields in complex structures with inhomogeneous background conductivity," *Geophysics*, vol. 71, no. 6, pp. 333–345, Nov.-Dec. 2006.

[12] C. J. Ong, and L. Tsang, “Full-wave analysis of large-scale interconnects using the multilevel UV method with the sparse matrix iterative approach (SMIA),” *IEEE Trans. Adv. Pack.*, vol. 31, no. 4, pp.818-828, Nov. 2008.

[13] E. Jorgensen, O. S. Kim, P. Meincke, and O. Breinbjerg, “Higher order hierarchical discretization scheme for surface integral equations for layered media,” *IEEE Trans. Geosci. Remote Sens.*, vol. 42, no. 4, pp. 764-772, Apr. 2004.

[14] M. Gruber and T. F. Eibert, “Simulation of reverberation chambers using method of moments with cavity Green’s function and spectral domain factorization,” in *Proc. IEEE Electromagn. Comp. Soc. Int. Symp.*, 2013, pp. 808-812.

[15] A. J. Poggio and E. K. Miller, Integral Equation Solution of Three Dimensional Scattering Problems. Elmsford, NY: Permagon, 1973.

[16] Y. Chang and R. F. Harrington, “A surface formulation for characteristic modes of material bodies,” *IEEE Trans. Antennas Propagat.*, vol. 25, no. 6, pp. 789-795, Nov. 1977.

[17] T. K. Wu and L. L. Tsai, “Scattering from arbitrarily-shaped lossy dielectric bodies of revolution,” *Radio Sci.*, vol. 12, pp. 709-718, Sep.-Oct. 1977.

[18] M. F. Wu, G. Kaur, and A. E. Yılmaz, “A multiple-grid adaptive integral method for multi-region problems,” *IEEE Trans. Antennas Propagat.*, vol. 58, no. 5, pp. 1601–1613, May 2010.

[19] E. K. Miller, “A selective survey of computational electromagnetics,” *IEEE Trans. Antennas Propagat.*, vol. 36, no. 9, pp. 1281-1305, Sep. 1988.

[20] X. M. Xu and Q. H. Liu, “The BCGS-FFT method for electromagnetic scattering from inhomogeneous objects in a planarly layered medium," *IEEE Trans. Antennas wireless Propagat. Lett.*, vol. 1, no. 1, pp. 77-80, 2002.

[21] K. Yang and A. E. Yılmaz, “FFT-accelerated analysis of scattering in rectangular cavities loaded with lossy dielectrics,” in *Proc. IEEE Antennas Propagat. Soc. Int. Symp.*, 2013.

[22] S. M. Rao, D. R. Wilton, and A. W. Glisson, “Electromagnetic scattering by surfaces of arbitrary shapes,” *IEEE Trans. Antennas Propagat.*, vol. 30, no. 3, pp. 409-418, May 1982.

[23] D. H. Schaubert, D. R. Wilton, and A. W. Glisson, “A tetrahedral modeling method for electromagnetic scattering by arbitrarily shaped inhomogeneous dielectric bodies,” *IEEE Trans. Antennas Propagat.*, vol. 32, no. 1, pp. 77-85, Jan. 1984.

[24] G. Kaur and A. E. Yılmaz, “A practical implementation and comparative assessment of the radial-angular-transform singularity cancellation method,” *IEEE Trans. Antennas Propagat.*, vol. 59, no. 12, pp. 4634-4642, Dec. 2011.

[25] D. R. Wilton and A. W. Glisson, “On improving the electric field integral equation at low frequencies,” in *Proc. USNC/CNC/URSI Meet.*, Jun. 1981, pp. 24.

[26] J. Mautz and R. F. Hanington, "An E-field solution for a conducting surface small or comparable to the wavelength," *IEEE Trans. Antennas Propagat.*, vol. 32, no. 4, pp. 330-339, Apr. 1984.

[27] J. S. Zhao and W. C. Chew, "Integral equation solution of Maxwell's equations from zero frequency to microwave frequencies," *IEEE Trans. Antennas Propagat.*, vol. 48, no. 10, pp. 1635-339, Oct. 2000.

[28] F. P. Andriulli, K. Cools, H. Bagci, F. Olyslager, A. Buffa, S. Christiansen, and E. Michielssen, "A multiplicative Calderon preconditioner for the electric field integral equation," *IEEE Trans. Antennas Propagat.*, vol. 56, no. 8, pp. 2398-2412, Aug. 2008.

[29] H. Bagci, F. P. Andriulli, K. Cools, F. Olyslager, and E. Michielssen, "A Calderón multiplicative preconditioner for coupled surface-volume electric field integral equations," *IEEE Trans. Antennas Propagat.*, vol. 58, no. 8, pp. 2680-2690, Aug. 2010.

[30] F. Vipiana, P. Pirinoli, and G. Vecchi, "A multi-resolution method of moments for triangular meshes," *IEEE Trans. Antennas Propagat.*, vol. 53, pp. 2247-2258, July 2005.

[31] F. Vipiana, G. Vecchi, and P. Pirinoli, "A multi-resolution system of Rao-Wilton-Glisson functions," *IEEE Trans. Antennas Propagat.*, vol. 55, no. 3, pp. 924-930, Mar. 2007.

[32] M. Taskinen and P. Ylä-Oijala, "Current and charge integral equation formulation," *IEEE Trans. Antennas Propagat.*, vol. 54, pp. 58-67, Jan. 2006.

[33] Z. G. Qian and W. C. Chew, "An augmented EFIE for high speed interconnect analysis," *Microw. Opt. Tech. Lett.*, vol. 50, no. 10, pp. 2658-2662, Oct. 2008.

[34] Y. P. Chen, L. J. Jiang, Z. G. Qian, and W. C. Chew, "An augmented electric field integral equation for layered medium Green's function," *IEEE Trans. Antennas Propagat.*, vol. 59, no. 3, pp. 960–968, Mar. 2011.

[35] I. T. Chiang and W. C. Chew, "New formulation and iterative solution for low-frequency volume integral equation," *J. of Electromagn. Waves and Appl.*, vol. 19, no. 3, pp. 289-306, 2005.

[36] C. Lu and B. Shanker, "Generalized finite element method for vector electromagnetic problems," *IEEE Trans. Antennas Propagat.*, vol. 55, no. 5, pp. 1369-1381, May 2007.

[37] J. M. Song and W. C. Chew, "Multilevel fast multipole algorithm for solving combined field integral equations of electromagnetic scattering," *Microw. Opt. Technol. Lett.*, vol. 10, no. 1, pp. 14-19, Sep. 1995.

[38] D. Gope and V. Jandhyala, "Efficient solution of EFIE via low rank compression of multilevel predetermined interactions," *IEEE Trans. Antennas Propagat.*, vol. 53, no. 10, pp. 3324-3333, Oct. 2005.

[39] E. Bleszynski, M. Bleszynski, and T. Jaroszewicz, "AIM: Adaptive integral method for solving large-scale electromagnetic scattering and radiation problems," *Radio Sci.*, vol. 31, pp. 1225-1251, Sep.-Oct. 1996.

[40] J. R. Phillips and J. K. White, "A precorrected-FFT method for electrostatic analysis of complicated 3-D structures," *IEEE Trans. Computer-Aided Design*, vol. 16, no. 10, pp. 1059–1072, Oct. 1997.

[41] A. Brandt, "Multilevel computations of integral transforms and particle interactions with oscillatory kernels," *Comp. Phys. Comm.*, vol. 65, no. 1-3, pp. 24–38, Apr. 1991.

[42] H. G. Wang, C. H. Chan, and L. Tsang, "A new multilevel Green's function interpolation method for large-scale low-frequency EM simulations," *IEEE Trans. Computer-Aided Design*, vol. 24, no. 9, pp. 1443 – 1427, Sep. 2005.

[43] D. Schobert and T. F. Eibert, "A multilevel interpolating fast integral solver with fast Fourier transform acceleration," in *Proc. URSI EMTS*, 2010, pp. 539–542.

[44] A. Boag and E. Michielssen, "Nonuniform polar grid algorithm for fast field evaluation," *IEEE Trans. Antennas wireless Propagat. Lett.*, vol. 1, no. 1, pp. 142-145, 2002.

[45] M. Vikram and B. Shanker, "Fast evaluation of time domain fields in sub-wavelength source/observer distributions using accelerated Cartesian expansions (ACE)," *J. Comp. Phys.*, vol. 227, pp. 1007–1023, 2007.

[46] M. Vikram, H. Huang, B. Shanker, and T. Van, "A novel wideband FMM for fast integral equation solution of multi-scale problems in electromagnetics," *IEEE Trans. Antennas Propagat.*, vol. 57, no. 7, pp. 2094-2104, July 2009.

[47] N. Geng, A. Sullivan, and L. Carin, "Fast multipole method for scattering from an arbitrary PEC target above or buried in a lossy half space," *IEEE Trans. Antennas Propagat.*, vol. 49, no. 5, pp. 740–748, May 2001.

[48] A. E. Yılmaz, "A two-scale AIM for fast solution of volume integral equations," in *Proc. 13th Annu. Rev. Progress Appl. Comput. Electromagn.*, Mar. 2009, pp. 511–516.

[49] F. Ling, C. F. Wang, and J. M. Jin, "An efficient algorithm for analyzing large-scale microstrip structures using adaptive integral method combined with discrete complex-image method," *IEEE Trans. Microw. Theory Tech.*, vol. 48, no. 5, pp. 832–839, May 2000.

[50] F. Ling, V. I. Okhmatovski, W. Harris, S. McCracken, and A. Dengi, "Large-scale broad-band parasitic extraction for fast layout verification of 3-D RF and mixed-signal on-chip structures," *IEEE Trans. Microw. Theory Tech.*, vol. 53, no. 1, pp. 264–273, Jan. 2005.

[51] V. Okhmatovski, M. T, Yuan, I. Jeffrey, and R. Phelps, "A three-dimensional precorrected FFT algorithm for fast method of moments solutions of the mixed-

potential integral equation in layered media," *IEEE Trans. Microw. Theory Tech.*, vol. 57, no. 12, pp. 3505-3517, Dec. 2009.

[52] T. J. Cui and W. C. Chew, "Fast algorithm for electromagnetic scattering by buried 3-D dielectric objects of large size," *IEEE Trans. Geosci. Remote Sens.*, vol. 37, no. 5, pp. 2597-2608, Sep. 1999.

[53] X. M. Millard and Q. H. Liu, "A fast volume integral equation solver for electromagnetic scattering from large inhomogeneous objects in planarly layered media," *IEEE Trans. Antennas Propagat.*, vol. 51, no. 9, pp. 2393–2401, Sep. 2003.

[54] K. Yang and A. E. Yılmaz, "A three dimensional adaptive integral method for layered media," *IEEE Trans. Geosci. Remote Sens.*, vol. 50, no. 4, pp. 1130-1139 Apr. 2012.

[55] K. Yang and A. E. Yılmaz, "FFT accelerated analysis of scattering from complex dielectrics embedded in uniaxial layered media," *IEEE Geosci. Remote Sensing Lett.*, vol. 10, no. 4, pp. 662-666, July 2013.

[56] K. Yang and A. E. Yılmaz, "An FFT-accelerated integral equation solver for analyzing scattering in rectangular cavities," *IEEE Trans. Microw. Theory Tech.*, vol. 62, no. 9, pp. 1930-1942, Sep. 2014.

[57] B. Shanker, K. Aygun, and E. Michielssen, "Fast analysis of transient scattering from lossy inhomogeneous dielectric bodies," *Radio Sci.*, vol. 39, no. RS2007, 2004.

[58] K. Yang and A. E. Yılmaz, "Integral equation solution of 3-D anisotropic lossy dielectrics in uniaxial layered media," in *Proc. IEEE Antennas Propagat. Soc. Int. Symp.*, 2012.

[59] K. Yang, F. Wei, and A. E. Yılmaz, "Truncate multigrid versus pre-corrected FFT/AIM for Bioelectromagnetics: When is O(N) better than O(NlogN)?," in *Proc. Computational Electromagnetics Int. Workshop*, pp. 153-158, Aug. 2011.

[60] M. F. Wu, K. Yang, and A. E. Yılmaz, "Efficient incorporation of PEC/PMC plane in the multiple-grid adaptive integral method," *IEEE Trans. Antennas Propagat.*, vol. 59, no. 1, pp. 314-319, Jan. 2011.

[61] J. R. Phillips and J. K. White, "Efficient capacitance extraction of 3D structures using generalized pre-corrected FFT methods," in *Proc. IEEE 3rd Topical Meeting on Electrical Performance of Electronic Packaging*, Nov. 1994.

[62] J. R. Phillips, Rapid solution of potential integral equations in complicated 3-dimensional geometries. Ph.D. Dissertation, Massachusetts Institute of Technology. Cambridge, MA, 1997.

[63] D. B. Avdeev, A. V. Kuvshinov, O. V. Pankratov and G. A. Newman, "Three-dimensional induction logging problems, Part I: An integral equation solution and model comparisons," *Geophysics*, vol. 67, no. 2, pp. 413-426, Mar.-Apr. 2002.

[64] F. Z. Wei and A. E. Yılmaz, "A hybrid message passing/shared memory parallelization of the adaptive integral method for multi-core clusters," *Parallel Comp.*, vol. 37, pp. 279-301, Jun.-July 2011.

[65] F. Z. Wei and A. E. Yılmaz, "A hybrid parallelization of AIM for multi-core clusters: implementation details and benchmark results on Ranger," arXiv: 1010.1456 [cs.CE], 8 Oct. 2010.

[66] S. Gabriel, R. W. Lau, and C. Gabriel, "The dielectric properties of biological tissues: I. Literature survey," *Phys. Med. Biol.*, vol. 41, no. 11, pp. 2231-2249, Nov. 1996.

[67] C. Gabriel and S. Gabriel, "Dielectric properties of body tissues," [Online]. Available: http://niremf.ifac.cnr.it/tissprop/.

[68] F. Wei, J. W. Massey, C. S. Geyik, and A. E. Yılmaz, "Error measures for comparing bioelectromagnetic simulators," in *Proc. IEEE Antennas Propagat. Soc. Int. Symp.*, 2012.

[69] K. Karlsson, J. Carlsson, and P. S. Kildal, "Reverberation chamber for antenna measurements: modeling using method of moments, spectral domain techniques, and asymptote extraction," *IEEE Trans. Antennas Propagat.*, vol. 54, no. 11, pp. 3106-3113, Nov. 2006.

[70] A. Borji, "Fast electromagnetic analysis and design of multiple coupled cavity structures," Ph.D. dissertation, University of Waterloo, Waterloo, Ontario, Canada, 2004.

[71] F. Gronwald, J. Nitch, and S. Tkachenko, "Hybrid representation methods for the efficient analysis of antenna coupling within cavities," in *Proc. 16th Int. Wroclaw Symp. Electromagn. Comp.*, 2002, pp. 109-114.

[72] U. Carlberg, P. S. Kildal, and J. Carlsson, "Study of antennas in reverberation chamber using method of moments with cavity Green's function calculated by Ewald summation," *IEEE Trans. Electromagn. Compat.*, vol. 47, pp. 805-814, Nov. 2005.

[73] S. Lopez-Pena, M. Mattes, and J. R. Mosig, "The impact of metallic scatters on the performance of a class of shielded structures," in *Proc. Antennas and Propagat. EuCap 2007*, 2007, pp. 1-7.

[74] M. Gruber and T. F. Eibert, "Simulation of reverberation chambers using method of moments with cavity Green's function and spectral domain factorization," in *Proc. IEEE Electromagn. Comp. Soc. Int. Symp.*, 2013, pp. 808-812.

[75] P. P. Ewald, "Die berechnung optischer und electrostatischer gitterpotentiale," *Ann. Phys.*, vol. 64, pp. 253–287, 1921.

[76] M. J. Park, J. Park, and S. Nam, "Efficient calculation of the Green's function for the rectangular cavity," *IEEE Microw. Guided Wave Lett.*, vol. 8, no. 3, pp. 124-126, Mar. 1998.

[77] M. J. Park, "Accelerated summation of the Green's function for the rectangular cavity," *IEEE Microw. Wireless Comp. Lett.*, vol. 19, no. 5, pp. 260-262, May 2009.

[78] A. Kustepeli and A. Q. Martin, "On the splitting parameter in the Ewald method," *IEEE Microw. Guided Wave Lett.*, vol. 10, no. 5, pp. 168-170, May 2000.

[79] F. T. Celepcikay, D. R. Wilton, D. R. Jackson, and F. Capolino, “Choosing splitting parameters and summation limits in the numerical evaluation of 1-D and 2-D periodic Green’s functions with the Ewald method,” *Radio Sci.*, vol. 43, no. 6, pp. RS6S01, Dec. 2008.

[80] K. Yang and A. E. Yılmaz, “On the accurate and efficient evaluation of Green functions for rectangular cavities with the Ewald method,” in preparation.

[81] H. P. Zhao and Z. X. Shen, “Efficient modeling of three-dimensional reverberation chambers using hybrid discrete singular convolution- method of moments,” *IEEE Trans. Antennas Propagat.*, vol. 59, no. 8, pp. 2943-2953, Aug. 2011.

[82] S. N. Makarov, Antenna and EM Modeling with Matlab. New York: Wiley, 2002.

[83] J. M. Putnam and L. N. Medgyesi-Mitschang, “Combined field integral equation for inhomogeneous two- and three-dimensional bodies: The junction problem,” *IEEE Trans. Antennas Propagat.*, vol. 39, no. 5, pp. 667-672, May 1991.

[84] M. Carr, E. Topsakal, and J. L. Volakis, “A procedure for modeling material junctions in 3-D surface integral equation approaches,” *IEEE Trans. Antennas Propagat.*, vol. 52, no. 5, pp. 1374-1379, May 2004.

[85] J. Meixner, “The behavior of electromagnetic fields at edges,” *IEEE Trans. Antennas Propagat.*, vol. 20, no. 4, pp. 442-446, Apr. 1972.

[86] R. F. Harrington, Time-Harmonic Electromagnetic Fields. New York: Wiley-IEEE Press, 1961.

[87] A. E. Yılmaz, D. S. Weile, J. M. Jin, and E. Michielssen, “A hierarchical FFT algorithm for the fast analysis of transient electromagnetic scattering phenomena,” *IEEE Trans. Antennas Propagat.*, vol. 50, no. 7, pp. 971–982, July 2002.

[88] H. G. Wang and C. H. Chan, “The implementation of multilevel Green's function interpolation method for full-wave electromagnetic problems,” *IEEE Trans. Antennas Propagat.*, vol. 55, no. 5, pp. 1348–1358, May 2007.

[89] K. Yang and A. E. Yılmaz, “An FFT-truncated multilevel interpolation method for multi-scale integral equation analysis,” in *Proc. USNC/URSI Rad. Sci. Meet.*, July 2011.

[90] X. C. Nie, L. W. Li, N. Yuan, T. S. Yeo, and Y. B. Gan, “Precorrected-FFT solution of the volume integral equation for 3-D inhomogeneous dielectric objects,” *IEEE Trans. Antennas Propagat.*, vol. 53, no. 1, pp. 313–319, Jan. 2005.

[91] K. A. Michalski and J. R. Mosig, “Multilayered media Green functions in integral equation formulations,” *IEEE Trans. Antennas Propagat.*, vol. 45, no. 3, pp. 508–519, Mar. 1997.

[92] E. Simsek and Q. H. Liu, “Singularity subtraction for evaluation of Green functions for multilayer media,” *IEEE Trans. Microw. Theory Tech.*, vol. 54, no. 1, pp. 216–225, Sep. 2006.

[93] D. G. Fang, J. J. Yang, and G. Y. Delisle, “Discrete image theory for horizontal electric dipoles in a multilayered medium above a conducting ground plane,” *IEE Proc. H*, vol. 135, pp. 297-303, Oct. 1988.

[94] K. A. Michalski, “Extrapolation methods for Sommerfeld integral tails,” *IEEE Trans. Antennas Propagat.*, vol. 46, no. 10, pp. 1405–1418, Oct. 1998.

[95] A. E. Yılmaz, J. M. Jin, and E. Michielssen, “Time domain adaptive integral method for surface integral equations,” *IEEE Trans. Antennas Propagat.*, vol. 52, no. 10, pp. 2692–2708, Oct. 2004.

[96] K. Yang and A. E. Yılmaz, “Comparison of pre-corrected FFT/adaptive integral method matching schemes,” *Microw. Opt. Technol. Lett.*, vol. 53, no. 6, pp. 1368-1372, Jun. 2011.

[97] X. C. Nie, L. W. Li, and N. Yuan, “Precorrected-FFT algorithm for solving combined field integral equations in electromagnetic scattering,” in *Proc. IEEE Antennas Propagat. Soc. Int. Symp.*, 2002, pp. 574–577.

[98] H. Bagcı, A. E. Yılmaz, V. Lomakin, and E. Michielssen, “Fast solution of mixed-potential time-domain integral equations for half-space environments,” *IEEE Trans. Geosci. Remote Sens.*, vol. 43, no. 2, pp. 269–279, Feb. 2005.

[99] B. Hu, “Fast inhomogeneous plane wave algorithm for electromagnetic scattering problems,” Ph.D. Dissertation, Dept. Elect. Comput. Eng., University of Illinois at Urbana-Champaign. Champaign, IL, 2001.

[100] Y. G. Li and S. K. Dai, “Finite element modeling of marine controlled-source electromagnetic responses in two-dimensional dipping anisotropic conductivity structures,” *Geophys. J. Int.*, vol. 185, no. 2, pp. 622-636, May 2011.

[101] T. J. Cui, W. C. Chew, A. A. Aydiner, and Y. H. Zhang, “Fast-Forward Solvers for the Low-Frequency Detection of Buried Dielectric Objects,” *IEEE Trans. Geosci. Remote Sens.*, vol. 41, no. 9, pp. 2026-2036, Sep. 2003.

[102] K. Yang and A. E. Yılmaz, “Comparison of pre-corrected FFT/AIM and FFT-truncated multilevel interpolation methods for multi-scale analysis,” in *Proc. Appl. Comp. Electromagnetics Symp.*, Mar. 2012.

[103] D. Pardo and C. Torres-Verdín, “Sensitivity analysis for the appraisal of hydrofractures in horizontal wells with borehole resistivity measurements,” *Geophysics*, vol. 78, no. 4, pp. D209-D222, July-Aug. 2013.

[104] K. Yang, E. Celik, C. Torres-Verdín, and A. E. Yılmaz, “Detection and quantification of 3D hydraulic fractures with multi-component low-frequency borehole resistivity measurements,” in *Proc. SEG Expanded Abstracts*, pp. 545-550, Sep. 2013.

[105] G. Gao, C. Torres-Verdín, and S. Fang, “Fast 3D modeling of borehole induction data in dipping and anisotropic formations using a novel approximation technique,” *Petrophysics*, vol. 45, no. 4, pp. 335-349, July-Aug. 2004.

[106] S. Fang, G. Gao, and C. Torres-Verdín, “Efficient 3D electromagnetic modeling in the presence of anisotropic conductive media, using integral equations,” *Exploration Geophysics*, vol. 37, no. 3, pp. 239-244, 2006.

[107] Y. P. Chen, J. L. Xiong, and W. C. Chew, “A mixed-form thin-stratified medium fast-multipole algorithm for both low and mid-frequency problems,” *IEEE Trans. Antennas Propagat.*, vol. 59, no. 6, pp. 2341-2349, Jun. 2011.

[108] S. Velamparambil and W. C. Chew, “Analysis and performance of a distributed memory multilevel fast multipole algorithm,” *IEEE Trans. Antennas Propagat.*, vol. 53, no. 8, pp. 2719-2727, Aug. 2005.

[109] Ö. Ergül and L. Gürel, "Efficient parallelization of the multilevel fast multipole algorithm for the solution of large-scale scattering problems," *IEEE Trans. Antennas Propagat.*, vol. 56, no. 8, pp. 2335-2345, Aug. 2008.

Vita

Kai Yang was born in Shanghai, China, in 1982. He received received the B. Eng. and M. Eng. degrees in electronic engineering from Shanghai Jiao Tong University, Shanghai, China, in June 2005 and March 2008, respectively.

Permanent Email address: white_yk@hotmail.com

This dissertation was typed by Yang, Kai.